Low-dose IL-2 reduces IL-21$^+$ T cells and induces a long-lived anti-inflammatory gene expression signature inversely modulated in COVID-19 patients

Jia-Yuan Zhang[1], Fiona Hamey[1], Dominik Trzupek[1], Marius Mickunas[2], Mercede Lee[1], Leila Godfrey[1], Jennie H.M. Yang[2], Marcin L Pekalski[1], Jane Kennet[3,4], Frank Waldron-Lynch[5], Mark L. Evans[3,4], Timothy I. M. Tree[2], Linda S. Wicker[1†], John A. Todd[1†] and Ricardo C. Ferreira[1†]

[1]JDRF/Wellcome Diabetes and Inflammation Laboratory, Wellcome Centre for Human Genetics, Nuffield Department of Medicine, NIHR Oxford Biomedical Research Centre, University of Oxford, Oxford, United Kingdom.

[2]Department of Immunobiology, King's College London, School of Immunology and Microbial Sciences, London, United Kingdom.

[3]Wellcome-MRC Institute of Metabolic Science, Metabolic Research Laboratories, University of Cambridge, Cambridge, United Kingdom.

[4]National Institute for Health Research Cambridge Biomedical Research Centre, Addenbrooke's Biomedical Campus, Cambridge, United Kingdom.

[5]Vertex Pharmaceuticals, Vertex Cell & Gene Therapies, Boston, Massachusetts, United States of America.

[†]Co-senior authors

Correspondence:

Prof. John A. Todd:

Email: john.todd@well.ox.ac.uk

Dr. Ricardo C. Ferreira:

Email: ricardo.ferreira@well.ox.ac.uk

Abstract

Despite early clinical successes, the mechanisms of action of low-dose interleukin-2 (LD-IL-2) immunotherapy remain only partly understood. Here, we examined the effects of interval administration of low-dose recombinant IL-2 (iLD-IL-2) using high-resolution, single-cell multiomics and flow cytometry. We confirmed that iLD-IL-2 selectively expands thymic-derived $FOXP3^{+}HELIOS^{+}$ Tregs and $CD56^{br}$ NK cells, and showed that treatment reduced the frequency of IL-21-producing $CD4^{+}$ T cells and of two subsets of innate-like $CD8^{+}$ T cells, mucosal-associated invariant T cells and $V_{\gamma 9}V_{\delta 2}$ T cells. The cellular changes induced by LD-IL-2 were associated with an anti-inflammatory gene expression signature, which remains detectable in all T and NK cell subsets analysed one month after treatment. The anti-inflammatory nature of this gene expression signature was supported by the observation that the same genes were also modulated in COVID-19 patients, but in the opposite direction. These findings warrant continued investigations of the potential clinical benefits of iLD-IL-2 in immunotherapy and further understanding of the development of long-term sequelae in convalescent COVID-19 patients.

Introduction

The use of much lower doses of interleukin-2 (IL-2) than employed in cancer therapy has shown clinical efficacy in a number of inflammatory and autoimmune conditions, by stimulating a subset of $CD4^+$ T cells expressing high levels of the high-affinity trimeric IL-2 receptor, designated as regulatory T cells (Tregs)[1–9]. In the autoimmune disease type 1 diabetes (T1D), the genetic association with the IL-2 pathway in mice[10] and in humans[11,12], combined with preclinical studies[13,14], have provided a strong rationale for the development of low-dose (LD)-IL-2 immunotherapy. Safety and dose determination studies in T1D have been informative and underpin future clinical trials in T1D[15–18]. We have previously conducted an adaptive single-dose observational study (DILT1D), which demonstrated the sensitivity and specificity of IL-2 signalling *in vivo* and determined a dosing range of $0.2\text{-}0.47\times10^6$ IU/m^2 of recombinant IL-2 (aldesleukin/proleukin) to achieve Treg increases in blood in the order of 20-50% from baseline[18]. We then performed a second study (DILfrequency)[19] to determine how often to give low-dose aldesleukin to reliably induce a steady-state Treg induction whilst maintaining the selective expansion of Tregs and not effector T cells.

Here, we explored in depth the effects and pharmacodynamics of interval LD-IL-2 dosing (iLD-IL-2) in DILfrequency peripheral blood mononuclear cell (PBMC) samples. We employed a recently developed targeted multiomics approach, which allowed us to simultaneously quantify 565 mRNA transcripts and 65 surface protein targets at the single-cell level[20]. We performed a detailed immunophenotypic characterization of both T and NK cell compartments, with a particular emphasis on the $CD4^+$ $CD127^{low}CD25^{hi}$ T cell and $CD56^{br}$ NK cell subsets, which have been previously shown to be highly sensitive to iLD-IL-2 treatment[18,19]. Aside from the expected expansions of thymic-derived $FOXP3^+HELIOS^+$ Tregs and $CD56^{br}$ NK cells in T1D patients, we show that iLD-IL-2 reduces the frequency of IL-21-producing cells, a subset that has been previously implicated in the pathogenesis of T1D[21–23]. The reduction of IL-21-producing cells by iLD-IL-2 may provide therapeutic benefit in T1D since a recent clinical trial combining anti-IL-21 with liraglutide (to improve beta cell function) slowed the decline of C-peptide[24]. Unexpectedly, we discovered that iLD-IL-2 also induces an anti-inflammatory gene expression signature in both

T and NK cell subsets that continues to at least one month after cessation of treatment. Altered expression of the same set of genes, but in the opposite direction, was found to be progressively induced and sustained in COVID-19 patients, highlighting the anti-inflammatory nature of the prolonged iLD-IL-2-induced gene changes. Taken together, our findings indicate that iLD-IL-2 can reduce IL-21 during treatment, and induce a suite of cellular alterations that promotes the establishment of a long-lived anti-inflammatory environment.

Results

Interval administration of low-dose IL-2 (iLD-IL-2) induces and maintains increased frequencies of CD4$^+$ CD127^{low}CD25^{hi} T cells and CD56^{br} NK cells

The DILfrequency[19] study established an optimal three-day aldesleukin dosing interval, with doses ranging from 0.20-0.47 × 10^6 IU/m^2 (**Fig. 1a**). To gain further insight into the mechanism of action of iLD-IL-2, we selected 18 DILfrequency participants (adults with long-standing T1D) treated with this dosing regimen (**Supplementary Table 1**) and characterised the cellular alterations in blood by polychromatic flow-cytometry (FACS). We observed a sustained increase in the frequency of CD4$^+$ CD127^{low}CD25^{hi} T cells (henceforth designated as the CD4$^+$ Treg gate) during the dosing phase, but no alterations in the frequency of the broader CD4$^+$ conventional T (Tconv) or CD8$^+$ T cell populations (**Fig. 1b,c**), including in a subset of CD45RA$^-$CD62L$^-$ effector memory CD4$^+$ T cells (T_{EM}), known to be enriched for recently activated effector T cells (**Supplementary Fig. 1a-c**).

Outside the T cell compartment, iLD-IL-2 also caused sustained increased frequencies of a subset of CD56^{br} NK cells (**Fig. 1c**). This effect was more pronounced than the increase in CD4$^+$ Tregs and is consistent with the relatively high affinity of the CD56^{br} NK subset for IL-2, especially when compared to the bulk NK population[25,26]. We observed no alteration in the frequency of the classical CD56^{dim} NK cells, which represent the majority of CD56$^+$ NK cells in circulation. The IL-2-induced increase in CD4$^+$ Tregs and CD56^{br} NK cells was recapitulated when assessing absolute numbers of cells in circulation, although their relative low abundance in blood resulted in no discernible alteration in the numbers of either CD4$^+$ and CD8$^+$ T cells or CD56$^+$ NK cells (**Fig. 1d,e**). An increase in both frequency and numbers of CD56^{br} (but not CD56^{dim}) NK cells in blood was observed in all IL-2 dose groups (**Supplementary Fig. 1d-f**).

Investigating IL-2-induced cellular alterations in blood using single-cell multiomics

We next profiled PBMCs from 13 selected participants treated with the three-day interval dosing regimen (**Supplementary Table 1**) using a targeted single-cell multiomics approach, which

enables the parallel quantification of specific mRNA and cell-surface proteins (AbSeq) in each cell[27]. To increase the power of this approach to identify small, yet potentially important, changes elicited by iLD-IL-2, we have adopted a cell enrichment strategy to greatly increase the numbers of $CD4^+$ Tregs and $CD56^{br}$ NK cells profiled in this study. In addition, we designed a custom mRNA panel of 565 oligonucleotide probes, assessed in parallel with the expression of 65 cell-surface protein targets (**Supplementary Table 2**)[20]. From each participant, we selected three longitudinal blood samples on Day 0 (baseline), Day 27 (immediately before the last IL-2 injection) and Day 55 (four weeks after the last IL-2 dose), respectively. We then isolated five immune populations from each sample following predefined proportions: 30% $CD4^+$ Tregs; 25% $CD4^+$ Tconv and $CD8^+$ T cells 12% $CD56^{br}$ and 8% $CD56^{dim}$ NK cells, which were analysed with or without *in vitro* stimulation (**Fig. 1f**). Unsupervised clustering of the 482,531 unstimulated cells passing quality control (QC) revealed a clear delineation of the sorted T and NK cell populations, identifying 15 distinct functional clusters (**Fig. 1g**). We observed good overlap among cells from each participant, with similar representation in the five sorted immune populations (**Supplementary Fig. 2a-c**). A similar result was observed for the clustering of the 323,839 stimulated cells passing QC (**Supplementary Fig. 2d-f**), indicating minimal batch effects that are usually prevalent in scRNA-seq data.

In the unstimulated cells, we also identified two clusters characterised by the distinct co-expression of a set of canonical cell cycle genes (see Methods), including *MKI67* (encoding for Ki-67), which corresponded to cycling T and NK cells (**Supplementary Fig. 3a**). Overall, we found no evidence that iLD-IL-2 was increasing the frequency of proliferating cells. Conversely, we found a reduction in the frequency of proliferating $CD56^{br}$ NK cells and $CD4^+$ Tregs at Day 27 (**Supplementary Fig. 3b**). Given the previously reported increased frequency of Ki-67^+ Tregs and $CD56^{br}$ NK cells following LD-IL-2 treatment, we next investigated the frequency of proliferating cells by assessing the intracellular expression of Ki-67 in patients treated with either single or multiple doses of LD-IL2. In agreement with previous observations[4,28,29], we found a marked increased frequency of Ki-67^+ cells in both $CD4^+$ Tregs and $CD56^{br}$ NK cells following the first dose of IL-2 (**Supplementary Fig. 3c,d**). In the multiple dosing cohort, we noted that this increased frequency of Ki-67^+ cells persisted up to Day 27 only in $CD56^{br}$ NK, but not in the $CD4^+$ Treg cells (**Supplementary Fig. 3d**). This discrepancy between the multiomics and FACS assessment of proliferating $CD56^{br}$ NK cells may reflect a difference in the use of protein or mRNA markers to

assess cell cycle progression. Both *MKI67* (mRNA) and Ki-67 protein are synthesised and accumulate during the S and G2/M phases of the cell cycle and show very good correlation in synchronised cells[30]. However, in contrast to *MKI67*, Ki-67 protein is more long-lived, and can still be detected in G1 after cell division[31]. The levels of Ki-67 protein in G1 depend on the rate of protein accumulation during the S and G2/M phases, leading to the much higher rate of detection of Ki-67$^+$ cells compared to the frequency of cells in the S-G/M phase (eg. 37% vs 1% in Fraction II Tregs)[32]. Consistently, we found that 20% of total CD4$^+$ Tregs are Ki-67$^+$ at baseline, but only ~1% were identified as proliferating by multiomics analysis. These data indicate that in contrast to Ki-67$^+$ protein levels, mRNA quantification allows a more specific identification of actively dividing cells (in the S-G/M phases). Therefore, an explanation for the discrepancy between the FACS and multiomics assessment of proliferating CD56^{br} NK cells at Day 27, is that the increased levels of Ki-67$^+$ cells reflect protein accumulation in recently divided G1 cells. In contrast, the decrease in proliferating cells from the multiomics analysis reflects a reduction of actively dividing cells in blood, possibly due to an increased likelihood for cells to enter the cell cycle in tissues as IL-2 accumulates on the extracellular matrix during dosing[33–36].

Interval administration of low-dose IL-2 selectively expands FOXP3$^+$HELIOS$^+$ Tregs

Next, we sought to investigate whether our iLD-IL-2 regimen altered the relative composition of the cells sorted from the CD127^{low}CD25^{hi} Treg gate (**Supplementary Fig. 4**). Analysis of the expression of the canonical Treg transcription factors *FOXP3* and *IKZF2* (encoding HELIOS) allowed the stratification of CD127^{low}CD25^{hi} Treg clusters into three functional groups according to their origin (**Supplementary Fig. 5** and **Methods**). Differential abundance analysis revealed an enrichment in the frequency of naïve FOXP3$^+$HELIOS$^+$ Tregs and a concomitant reduction of CD25$^+$ FOXP3$^-$HELIOS$^-$ Teffs on Day 27, after the conclusion of the four-week IL-2 dosing phase, immediately before the last of the ten aldesleukin injections (**Fig. 2a,b**), which was replicated in stimulated cells (**Fig. 2c,d**). Given the observed increase in CD127^{low}CD25^{hi} T cells by FACS following LD-IL-2, we next investigated whether these changes were also reflected in the absolute numbers in circulation, which were inferred from the relative frequencies identified by single-cell analysis, scaled by the whole-blood CD127^{low}CD25^{hi} Treg counts. We found that the IL-2 induced expansion on Day 27 was restricted to the thymic-derived FOXP3$^+$HELIOS$^+$ Treg subsets (**Fig. 2e**). We observed very good concordance between unstimulated and stimulated

conditions, with naïve Tregs showing >2-fold increase and memory FOXP3^{+}HELIOS^{+} Tregs displaying approximately a 70% increase in cell numbers compared to baseline pre-treatment levels (**Fig. 2e**). In contrast, despite the expansion of CD127^{low}CD25^{hi} T cells, we obtained no evidence of alterations in the number of activated CD25^{+} FOXP3^{-}HELIOS^{-} Teffs contained in this population, even though they express the high affinity trimeric IL-2 receptor (**Fig. 2e**). Furthermore, we observed no changes in the *in vitro* suppressive capacity of CD4^{+} CD127^{low}CD25^{hi} T cells after IL-2 treatment on a per cell basis compared to the pre-treatment cells (**Fig. 2f**). The alterations in the relative composition of CD127^{low}CD25^{hi} T cells were found to be transient and reverted to baseline one month after the last dose of IL-2 (Day 55; **Supplementary Fig. 6a-d**). In contrast, we observed no notable changes in the relative abundance of CD4^{+}CD25$^{-/low}$ Tconv subsets during or after IL-2 treatment (**Supplementary Fig. 7**).

Using pseudo-time analysis, we identified a single trajectory of FOXP3^{+} Treg differentiation among CD4^{+} T cells, stemming from the conventional naïve Tregs towards the classical HLA-II^{+} effector Treg subset (**Supplementary Fig. 8a-c**). In agreement with our compositional analysis, we found a significantly increased ratio of naïve to HLA-II^{+} Tregs at Day 27 (**Supplementary Fig. 8d**). Notably, there was no alteration in the differentiation status of Tregs in response to iLD-IL-2, as illustrated by the overlapping pseudo-time distribution within the Treg differentiation trajectory between Days 0, 27 and 55 (**Supplementary Fig. 8d**). These data indicate that iLD-IL-2 treatment is affecting only the output and/or survival of thymic-derived naïve Tregs but not their differentiation towards HLA-II^{+} effector Tregs. Furthermore, we also replicated the transient IL-2-induced increase in the frequency of naïve Tregs by measuring the naïve:memory Treg ratio at Day 27 by FACS in all 18 DILfrequency participants treated with the 3-day interval dosing schedule (**Supplementary Fig. 9a-c**). We found good concordance between FACS and single-cell data on the frequency of naïve and memory Tregs as well as their ratios (**Supplementary Fig. 9d,e**). To confirm the characterisation of Treg subsets obtained through the single-cell multiomics analysis, we next assessed the protein expression of FOXP3 and HELIOS by FACS in our single and multiple dosing replication cohorts. In agreement with the multiomics analysis, we found a selective decrease in the relative proportion of CD45RA^{-} FOXP3^{-}HELIOS^{-} cells within CD127^{low}CD25^{hi} T cells in both cohorts in response to iLD-IL-2 (**Supplementary Fig. 10a-c**). These results translated into a consistent increase in the frequency of both CD4^{+}CD25^{hi} FOXP3^{+}

Treg subsets and a concomitant reduction in $CD4^{+}CD25^{hi}$ $FOXP3^{-}HELIOS^{-}$ Teffs (**Supplementary Fig. 10d,e**).

In addition to the conventional $CD25^{hi}$ $FOXP3^{+}$ Treg subsets, we have recently shown that a subset of $CD25^{-/low}$ $FOXP3^{+}$ T cells are increased in patients with autoimmune diseases[37]. We found no substantial change in the frequency of $CD25^{-/low}$ $FOXP3^{+}$ T cells (defined as cells with >=1 copy of FOXP3 within the $CD4^{+}CD25^{-/low}$ Tconv gate; **Supplementary Fig. 11a,b**). We replicated these results using a FACS approach to vastly increase the number of characterised $CD25^{-/low}$ $FOXP3^{+}$ T cells. In agreement with the multiomics analysis we found no change in the frequency of this rare subset in either the single or multiple dosing cohorts (**Supplementary Fig.11c-g**). However, we noted a small reduction in the frequency of $CD25^{-/low}$ $FOXP3^{+}$ T cells at Day 27 by both methods, suggesting that iLD-IL-2 may restore the CD25 expression in these cells.

IL-21-producing T cells are reduced by iLD-IL-2 treatment

Among the identified $CD25^{+}$ $FOXP3^{-}HELIOS^{-}$ Teff clusters within the sorted $CD127^{low}CD25^{hi}$ Treg cells, we noted an IL-2-induced reduction of a subset with a marked T follicular helper (T_{FH}) cell profile, including the expression of canonical T_{FH} receptors CXCR5, PD-1 and ICOS, and the transcription factor *MAF* ($CD25^{hi}$ T_{FH}, cluster 8; **Supplementary Figs. 4a** and **6a)**. Although differentiated T_{FH} cells are rare in blood, within cells sorted from the $CD25^{-/low}$ Tconv gate, we were able to characterise an analogous heterogeneous cluster of central memory (T_{CM}) $CXCR5^{+}$ cells (cluster 1; **Supplementary Fig. 7a-c**), which is known to be enriched with circulating precursors of T_{FH} cells. Upon *in vitro* stimulation, which elicited the expression of the classical T_{FH} cytokine IL-21, we obtained a better discrimination of the T_{FH} clusters. This led to improved differentiation of a cluster of $CXCR5^{+}$ T_{CM} cells (cluster 2) and a cluster of $CXCR5^{low}$ $IL\text{-}21^{+}$ T cells (cluster 6) that was reduced with IL-2 dosing (**Supplementary Fig. 7d-f**). In addition, within the $CD127^{low}CD25^{hi}$ Treg gate, *in vitro* stimulation allowed the stratification of the activated $CD25^{+}$ T_{FH} cells into two separate clusters (cluster 10 and 11) based on their expression of IL-21 that were both reduced by iLD-IL-2 treatment (**Supplementary Fig. 6b**). We note that a related cluster of $FOXP3^{+}$ T follicular regulatory cells (T_{FR}, cluster 11 in unstimulated cells) which, in addition to the T_{FH} signature, also featured a distinct Treg transcriptional profile as well as the

upregulation of *POU2AF1* and *CCR9*, was not altered by iLD-IL-2 treatment (**Supplementary Fig. 6a**).

Next, we compared the transcriptional profile of the four identified T_{FH}-like clusters marked by the specific upregulation of IL-21 expression. We identified a continuum of T_{FH} cell differentiation among these clusters, with the $CD25^{+}IL\text{-}21^{+}$ T_{FH} subset representing the terminal stage of maturation in blood, as illustrated by their classical T_{FH} profile and increased IL-21 production (**Fig. 3a**). Analysis of the co-expression of CXCR5 and IL-21 revealed that IL-21 was preferentially expressed within the $CXCR5^{+}$ cells (**Fig. 3b**). The exception was in the $CXCR5^{low}$ $IL\text{-}21^{+}$ cluster, where approximately 50% of the $IL\text{-}21^{+}$ cells were also $CXCR5^{low}$. These data suggest that our single-cell multiomics approach allows us to specifically identify the more differentiated IL-21-producing T cells in this cluster, with a phenotype resembling the $CXCR5^{low}$ $PD\text{-}1^{hi}$ circulating T peripheral helper (T_{PH}) cells that have been previously shown to be increased in T1D patients[23]. Furthermore, we found similar profiles between the $CXCR5^{+}$ T_{CM} and the $CD25^{+}$ T_{FH} clusters sorted from the $CD25^{-/low}$ Tconv and $CD25^{+}$ Treg gates, respectively, with the latter likely representing an earlier stage of T_{FH}-cell differentiation. In agreement with this shared identity and developmental stage, the $CXCR5^{+}$ T_{CM} and $CD25^{+}$ T_{FH} subsets displayed largely overlapping embeddings among all stimulated $CD4^{+}$ T cells (**Fig. 3c,d**). In contrast to these three conventional T_{FH}-like subsets, which seem to share a similar differentiation pathway, the $CXCR5^{low}IL\text{-}21^{+}$ $CD25^{-/low}$ Teff cluster represented a much more heterogeneous cluster with a scattered clustering profile and increased IL-21 production (**Fig. 3c,d**).

To better discriminate the effect of IL-2 on the differentiation of IL-21-producing cells, we then stratified the cells in these four T clusters according to their expression of IL-21 to define activated T_{FH} profiles (**Fig. 3e**). Consistent with the results from the differential abundance analysis (**Supplementary Figs. 6b** and **7e**), we found evidence for a reduction in the relative proportion of $IL\text{-}21^{+}$ cells at Day 27 in the two subsets with higher frequencies of $IL\text{-}21^{+}$ cells (**Fig. 3f**). Furthermore, pseudo-time analysis in total stimulated $CD4^{+}$ T cells revealed a similar trajectory of T_{FH} cell differentiation characterised by the acquisition of an activated T_{FH} phenotype and production of IL-21 (**Supplementary Fig. 8e-g**). In contrast with the $FOXP3^{+}$ Treg trajectory, iLD-IL-2 was found to impair this differentiation trajectory, as illustrated by the reduced pseudo-time distribution at Day 27 among cells from the more differentiated $CD25^{+}IL\text{-}21^{+}$ T_{FH} subset

(**Supplementary Fig. 8h**). These results further support a broader, previously uncharacterized, effect of iLD-IL-2 immunotherapy in potentially inhibiting the differentiation of IL-21-producing cells. In addition to the reduction of IL-21-producing cells, we also obtained some evidence (FDR-adjusted $P = 0.096$) for the reduction of another subset marked by the expression of many pro-inflammatory cytokines, including GM-CSF, IL-21 and IL-2, as well as the classical type-2 inflammatory cytokines IL-4 and IL-13 ($CD25^+$ T_{H2} T_{EM}, cluster 6; **Supplementary Figs. 4b** and **6b**).

Effects of iLD-IL-2 on $CD8^+$ T and $CD56^+$ NK cells

In the $CD8^+$ T cell compartment, differential abundance analysis revealed no discernible differences in the relative composition of the conventional αβ $CD8^+$ T cell subsets after IL-2 treatment. However, we identified a previously uncharacterised reduction of two subsets of innate-like $CD8^+$ T cells, including mucosal-associated invariant T cells (MAIT; cluster 4) and $V_{\gamma 9}V_{\delta 2}$ T cells (cluster 9; **Fig. 4a,b** and **Supplementary Fig. 12**). In contrast to the IL-2 induced alterations in the $CD4^+$ T cell compartment, the reduction of circulating MAIT and $V_{\gamma 9}V_{\delta 2}$ T cells was more long-lived and there was still evidence of a reduced frequency in blood one month after the last dose of IL-2 (**Fig. 4c**).

Finally, in the $CD56^+$ NK cell compartment, despite the lower level of functional heterogeneity and differentiation (**Fig. 4d,e**), we found that the increased frequency of $CD56^{br}$ NK cells after IL-2 treatment, was driven particularly by an increased relative proportion of an activated HLA-II^+ subset (**Fig. 4f**). By contrast we found no alterations in the relative composition of $CD56^{dim}$ subsets (**Fig. 4g** and **Supplementary Fig. 13**). Consistent with activation phenotype and increased expression of CD56 on $CD56^{br}$ NK cells after treatment, we observed a reduced frequency of contaminating $CD56^{dim}$ and $CD56^{br}$ NK cells sorted from the $CD56^{br}$ and $CD56^{dim}$ NK cell gates, respectively at Day 27 (**Fig. 4f,g**). The alterations in the $CD56^{br}$ NK cells were also transient and were not maintained one month after treatment (**Supplementary Fig. 13b,c**).

Interval low-dose IL-2 immunotherapy induces a systemic and long-lasting anti-inflammatory gene expression signature

We next investigated whether, in addition to cellular composition alterations, we could detect IL-2-induced gene expression changes. On Day 27, we identified 40 genes that are differentially expressed in one or more subsets of unstimulated and stimulated cells (**Fig. 5a-c**). Consistent with previous flow cytometry analyses[19], CD25 was strongly upregulated on Tregs on Day 27. The differential expressed genes were mostly restricted to the more IL-2-sensitive CD127^{low}CD25^{hi} Treg and CD56^{br} NK cell subsets and could be broadly categorised into CD4^{+} Treg and CD56^{br} NK cell signature genes, reflecting the relative increased proportion of both subsets after iLD-IL-2 treatment, as well as the identified reduction in actively dividing CD56^{br} NK cells (**Supplementary Fig. 3b**). Cycling cells were not present in the stimulated cell populations, potentially due to the preferential sensitivity of cycling cells to apoptosis following activation.

Contrary to the differential expression on Day 27, which was observed exclusively in the IL-2-sensitive Treg and CD56^{br} subsets, differential expression on Day 55, one month after the last IL-2 injection, was widespread and displayed a consistent pattern in all five assessed immune subsets (**Fig. 6a** and **Supplementary Fig. 14a,b**). These findings indicate that our iLD-IL-2 dosing regimen induces a shared Day 55 gene expression signature in different cell types, which featured most prominently the upregulation of Cytokine Inducible SH2 Containing Protein (*CISH*), a gene encoding a well-characterised negative regulator of cytokine signalling, and the downregulation of Amphiregulin (*AREG*), a secreted TNF-inducible protein with pleiotropic roles in inflammation[38]. We also noted an enrichment of genes associated with cytokine signalling, most notably in the tumour necrosis factor (TNF) signalling pathway, which in addition to *CISH* and *AREG*, also included *TNFSF14*, *TNFSF10*, *STAT1*, *SGK1*, *NFKBIZ*, *NFKBIA*, *DUSP2*, *DUSP4*, *DUSP5*, *RGS1* and *TNFAIP3* (**Fig. 6a**). Furthermore, we observed a downregulation of several TNF-induced genes that play a central role in curtailing TNF signalling, including the inhibitors of NFκB, *NFKBIZ* and *NFKBIA*, *RGS1*, *TNFAIP3* and *AREG*. Consistent with this observation, Oncostatin M (*OSM*), a pro-inflammatory cytokine shown to be increased in inflammatory bowel disease patients with poor response to anti-TNF therapy[39], was also downregulated by iLD-IL-2. Increased expression of *TNFSF14*, which encodes LIGHT, is notable since decreased expression is associated with higher susceptibility to multiple sclerosis[40] and in a mouse model of multiple

sclerosis, LIGHT expression in the brain limits disease severity[41]. The widespread detection of this signature in all five T and NK cell populations assessed in this study suggests that this effect is not driven by IL-2 signalling directly but is likely the result of the sustained cellular changes induced by iLD-IL-2 immunotherapy.

Although this Day 55 expression signature was detected in 11 of the 12 participants with Day 55 data, we observed heterogeneity among participants for the expression levels of the same genes on Day 27 (**Fig. 6b**). Some participants exhibited concordant expression changes on Day 27 and Day 5, compared to Day 0, while others showed discordant expression profiles, with *CISH* being downregulated and *AREG* upregulated on Day 27. Moreover, by principal component analysis (PCA), we found that this concordant-discordant axis, captured by the first principal component (PC1), was able to largely explain the inter-individual heterogeneity of Day 55 signature genes on Day 27 and appeared to be associated with IL-2 dose (**Supplementary Fig. 14c**). Considering this, we derived a linear score to quantify the changes in the Day 55 signature for each participant, referred to as the Day 55 signature score, with higher scores reflecting higher expression of signature genes upregulated on Day 55 (e.g. *CISH*), and lower expression of signature genes downregulated on Day 55 (e.g. *AREG*). As expected, the Day 55 signature score showed considerable inter-individual variation (**Fig. 6c**) that was consistent across different cell types (**Supplementary Fig. 14d**). This enabled us to correlate changes in signature score, which indicated the direction and amplitude of the modulation of Day 55 genes, with IL-2 dose level. We confirmed that participants receiving higher doses of IL-2 were more likely to have increased signature scores on Day 27 and Day 55 compared the baseline, indicating concordant expression changes, whilst participants receiving lower doses tended to show discordant changes (**Fig. 6d,e**). The dose-dependence of the Day 55 signature reached statistical significance only when comparing to the participant-specific baseline, but not when inspecting the cross-sectional data at each time point (**Supplementary Fig. 14e**). This underscores the importance of our longitudinal study design that enhanced our statistical power to identify differential expression patterns.

Long-lived iLD-IL-2 gene expression alteration is inversely modulated in COVID-19 patients and is progressively induced after the onset of symptoms

To extend the support for the existence of the Day 55 gene expression signature, we sought independent evidence of a similar transcriptional response with another immune challenge. Recently, the Oxford COVID-19 Multi-omics Blood Atlas (COMBAT) study[42] has generated a large single-cell dataset illustrating the changes in blood induced by COVID-19 infection. We found a reverse regulation in all immune populations of the 41 identified IL-2 regulated Day 55 signature genes, including a marked downregulation of *CISH* and upregulation of *AREG* in COVID-19 patients (**Fig. 7A**). This finding was replicated in an independent cohort of convalescent COVID-19 patients (INCOV)[43]. In both cohorts, we observed a progressive reduction of the Day 55 gene expression signature, which was particularly pronounced for the first 2-3 weeks after the onset of symptoms (**Fig. 7b,c**). In the INCOV cohort, follow-up samples taken several months after initial symptoms revealed signs of a slow recovery towards the pre-COVID-19 baseline. (**Fig. 7c**). This progressive induction of the Day 55 signature genes was observed in all COVID-19 disease severity groups and was consistent in all immune populations (**Supplementary Fig. 15**).

In the COMBAT study[36], a multiparametric COVID-19-induced gene expression signature, designated as Component 187, featured the differential expression of several Day 55 iLD-IL-2 signature genes, including *CISH* and *AREG*. Of the 1,419 genes contributing to the COVID-19 Component 187, 77 were present in our transcriptional panel. We found that virtually all signature genes upregulated on Day 55 had negative loading scores in the COVID-19 Component 187, and vice versa (**Fig. 7d**), indicating a strong inverse correlation between the differential gene expression induced by IL-2 treatment and COVID-19. In the COMBAT study, Component 187 belonged to Cluster 3, a cluster of similar gene expression signatures associated with all severity groups of COVID-19 patients. We found that Cluster 3 showed the strongest enrichment of the Day 55 Signature genes, compared to all other reported clusters (**Fig. 7e**). Furthermore, the dynamics of Component 187 over time were similar to that of the Day 55 Signature, though in the opposite direction (**Fig. 7f**), implying that the set point of a homeostatic cellular network is altered in opposing directions by LD-IL-2 immunotherapy and COVID-19.

Discussion

Our findings not only extend previous studies[15–17,28] but also provide new insight into the mechanism of action of LD-IL-2 that has practical implications for its clinical use: firstly, we show that LD-IL-2 administered every three days for a period of one month is able to selectively increase the frequency and number of thymic-derived FOXP3$^+$HELIOS$^+$ Tregs in all 18 study participants analysed, while showing no detectable impact on the expansion or activation of conventional effector T or CD56^{dim} NK cells. We observed a particularly pronounced increase in the frequency of naïve FOXP3$^+$HELIOS$^+$ Tregs after iLD-IL-2 therapy, indicating that the Treg increases are caused by an increased representation of thymic-derived Tregs, and not the proliferation of peripherally-induced Tregs. These findings are consistent with the increased clonal diversity in T cells following an escalating LD-IL-2 regimen in graft-versus-host disease patients[44,45]. Secondly, we also noted that our iLD-IL-2 schedule did not induce a detectable cytotoxic gene expression signature in any T cell subset, indicating that among T cells iLD-IL-2 has a Treg-specific effect and does not lead to the activation of a pro-inflammatory response. In addition to Tregs, the CD56^{br} NK cell population is also probably contributing to the overall anti-inflammatory effects of iLD-IL-2, in an immunoregulatory role, as previously described[46,47]. Thirdly, iLD-IL-2 was able to reduce IL-21-producing T cells, possibly by antagonizing their differentiation. IL-2 signalling has been shown to inhibit the differentiation of T_{FH} cells *in vivo* in mice[48], and in an *in vitro* model in humans[49]. Consistent with these findings, LD-IL-2 has been shown to decrease the frequency of T_{FH} cells, as defined by cell surface markers[50], as well as the frequency of marginal zone B cells[29] in SLE patients, supporting a role in the regulation of germinal centre reactions. Our results extend these findings to T1D and demonstrate a specific effect of iLD-IL-2 treatment in reducing pathogenic IL-21-producing CXCR5$^+$ T_{FH} cells as well as IL-21-producing CXCR5^{low} T cells. Previously, we have shown that a two-fold increase in IL-2, but not IL-21, was responsible for the protective effect conferred by the *Idd3* locus (containing *IL2* and *IL21*) in the nonobese diabetic (NOD) mouse model of T1D[13], and independently that a reduction in IL-21 correlated with increased IL-2[51]. In humans, IL-21 has been implicated in the pathogenesis of several autoimmune diseases[52,53], particularly T1D[21–23]. Together, these observations lend further support for the use of iLD-IL-2 in T1D as well as in other diseases associated with increased IL-21 production, such as systemic lupus erythematosus, rheumatoid arthritis, and psoriasis. In support of this therapeutic

399 strategy, an anti-IL-21 monoclonal antibody in combination with liraglutide showed promising
400 results in preserving beta-cell function[24]. Of note, we observed no evidence for the alteration of
401 the frequency of FOXP3$^+$ T_{FR} cells, which has been previously shown to play a role in the
402 regulation of T_{FH} cells and the germinal centre reaction[54,55].

403 We also observed a decrease in circulating innate-like CD8$^+$ MAIT and $V_{\gamma 9}V_{\delta 2}$ T cell subsets
404 during treatment and one month after. Since these cells function in anti-viral and anti-bacterial
405 defence[56], our findings suggest a role of IL-2 immunotherapy in the recruitment of MAIT and
406 $V_{\gamma 9}V_{\delta 2}$ T cells to tissues following treatment, thereby increasing defence against viral and bacterial
407 infections[57]. This could provide a mechanism for the observed decreased incidence of viral
408 infections in SLE patients undergoing LD-IL-2 immunotherapy[58].

409 The cellular alterations induced by iLD-IL-2 treatment led to the establishment of a long-lived
410 gene expression signature in all assessed immune populations, which suggest a novel
411 immunoregulatory mechanism of iLD-IL-2. Although the effects of this signature are not yet
412 understood, it is marked by the distinct upregulation of *CISH*, a well-characterised negative
413 regulator of cytokine signalling whose expression is known to be induced by IL-2, as well as other
414 cytokines, signalling through the activation of STAT5[59]. In contrast, among the downregulated
415 genes, we observed several negative regulators of an inflammatory response at Day 55, including
416 key TNF-induced genes such as *TNFAIP3*, *RGS1* and *AREG*, suggesting that iLD-IL-2 can
417 decrease the homeostatic levels of TNF for at least one month after the cessation of dosing. Support
418 for the existence of the iLD-IL2-induced long-lived gene expression signature was obtained from
419 analysis of the Oxford COMBAT dataset[42], where we detected the modulation of the same genes,
420 but showing consistent opposite direction of expression following the onset of COVID-19
421 symptoms. We replicated this signature in a large longitudinal cohort of convalescent COVID-19
422 patients[43], which demonstrated a progressive induction of these genes that was particularly
423 pronounced in the first two weeks after onset of symptoms. This altered expression profile was
424 consistently sustained for up to 5 months, evidencing the longevity of this immune dysregulation
425 in COVID-19 patients. One possible explanation for the longevity of the signature is that TNF and
426 IL-2 are among the cytokines known to bind to the extracellular matrix[33–36] and that the retention
427 of the cytokines within tissues extends far beyond their initial increases[60]. The establishment of
428 the Day 55 IL-2 signature is dose-dependent at Day 27, likely reflecting a dose-dependent

accumulation of injected IL-2 on the extracellular matrix within the interstitial space following subcutaneous dosing. A long-lasting immune alteration that also possibly reflects a continuing inflammatory stimulus or long-lived pro-inflammatory cytokines on the extracellular matrix has been reported in mild COVID-19 patients, with infection inducing a pro-inflammatory response in monocyte-derived macrophages that continues to be detected 3-5 months following SARS-CoV-2 infection[61]. In a separate study, pro-inflammatory markers such as IL-8 and sTIM-3 were still elevated four months after the cessation of COVID-19 symptoms in patients having had mild or moderate disease, but the increases resolved eight months post-infection except in patients with long COVID[62].

We hypothesise that the balance between pro- and anti-inflammatory cytokines bound to the extracellular matrix provides a regulatory mechanism to control immune responses. Circulating immune cells can constantly integrate this information through a combination of cell-type specific receptors. Under homeostatic conditions this provides a dynamic buffer system preventing excessive (or potentially chronic) immune activation. A perturbation of this balance via either sustained regulatory (e.g. iLD-IL-2 immunotherapy) or inflammatory (e.g. SARS-CoV-2 infection) environment can alter the composition of the soluble mediators contained in the extracellular matrix, and consequently affect the interaction between the immune system and the local environment, leading to the remodelling of their transcriptional profile and an alteration of their threshold for further stimulation. Such a complex system is likely critical not only to prolong the biological activity of key immune mediators such as TNF and IL-2, but also to control site specificity to prevent improper signalling in the wrong physiological context. These findings are also consistent with our observation that pro-inflammatory gene expression is progressively induced after infection, and that it could contribute to the long-lasting systemic alterations associated with the persistence of clinical manifestations in long COVID patients.

A limitation of this study is that we were not able to elucidate the exact mechanism underpinning the induction of the identified long-lived gene expression signature and how this is regulated by iLD-IL-2 or COVID-19. Although we show that iLD-IL-2 can induce this signature, it is certainly not the only responsible factor, as a reversed expression can also be induced in a completely different pathophysiological context such as COVID-19. Furthermore, markers of disease activity and progression are limited in T1D and were not collected for the DILfrequency patients, which

459 precludes the analysis of how they are associated with these gene expression alterations. A more
460 comprehensive investigation of these questions will need to be performed in an appropriate follow
461 up cohort such as the recently completed Interleukin-2 Therapy of Autoimmunity in Diabetes
462 (ITAD) trial[63]. The findings from this study will inform the design of suitable follow up
463 experiments in this and other studies of iLD-IL-2 in multiple diseases and will be critical to better
464 understand both the longevity of the signature and how it is associated with clinical outcomes.
465 Another limitation is that the interpretation of the results may be dependent on our specific iLD-
466 IL-2 dosing regimen. Although it is likely that most regimens will induce very similar results, it
467 will be important to validate these findings in different dosing schedules. Given the diverse range
468 of conditions where LD-IL-2 immunotherapy is being trialled, it is critical to better understand
469 how dosing regimen affects the drug's mechanism of action, and to tailor it to the disease-specific
470 applications, including when best to administer IL-2 during the course of standard care or as a way
471 of maintaining the clinical benefits of ongoing treatments[64], for example, in the use of anti-CD3
472 (teplizumab) to treat and prevent T1D[65].

473 Taken together, our findings provide a better understanding of the mechanism of action of LD-IL-
474 2 immunotherapy. In the past there have been concerns over the very short half-life of recombinant
475 IL-2 *in vivo* and that NK cell expansion might be detrimental, which have led to the development
476 of genetically-modified IL-2 muteins with increased half-life and preferential binding to the high-
477 affinity trimeric IL-2 receptor in order to reduce $CD56^{br}$ NK cell stimulation. Our results
478 demonstrating a long-lived gene expression signature associated with potential anti-inflammatory
479 effects, detectable one month after the end of aldesleukin treatment, alleviate some of these
480 concerns and support the therapeutic potential of IL-2 that is not engineered for longer *in vivo* half-
481 life or preferential binding to the high affinity IL-2 receptor, given intermittently and at low doses.
482 Our study adds to the good track record of using low-dose recombinant IL-2 and confirms its very
483 strong safety profile, which is critical for the potential long-term use of LD-IL-2 immunotherapy
484 for diseases such as T1D in which the target patient population will consist mainly of children,
485 including the possible future use of iLD-IL-2 treatment in the prevention of T1D diagnosis, as
486 demonstrated in recent teplizumab trials[65] and for T1D treatment with other monoclonal antibodies
487 such as golimumab (anti-TNF)[66,67]. Additionally, iLD-IL-2 treatment could be trialled in
488 recovering COVID-19 patients, after acute inflammation has been resolved, to determine if such

489 treatment hastens the restoration of normal immune homeostasis and perhaps reduce the
490 occurrence of long COVID complications.

Methods

The study was performed in accordance with the guidelines for good clinical practice and the Declaration of Helsinki. Study participants included T1D patients enrolled in two single centre mechanistic studies of low-dose recombinant IL-2 (aldesleukin) immunotherapy: (i) the Adaptive study of IL-2 dose on regulatory T cells in type 1 diabetes (DILT1D), a non-randomised single IL-2 dosing study20; and (ii) the Adaptive study of IL-2 dose frequency on regulatory T cells in type 1 diabetes (DILfrequency), a response-adaptive trial of repeated doses of IL-2 administered using an interval dosing approach21. Approval was obtained from the Health Research Authority, National Research Ethics Service (13/EE/0020 and 14/EE/1057, for the DILT1D and DILfrequency studies, respectively), London, United Kingdom. The trials were registered at the International Standard Randomised Controlled Trial Number Register (ISRCTN27852285 and ISRCTN40319192) and ClinicalTrials.gov (NCT01827735 and NCT02265809). The study protocols were published in advance of the completion and final analysis of the trials[68,69]. All participants provided written informed consent prior to their participation in the studies.

Study design and participants

Study participants comprised 18 T1D patients enrolled in the DILfrequency study[19]. All 18 study participants, who were all adult patients diagnosed with T1D over 60 months before recruitment into the study, were selected from the 3-day interval group and were treated with IL-2 with doses ranging from 0.2 to 0.47 × 10^6 IU/m^2.

FACS-based replication of the single-cell multiomics findings was performed in two follow-up cohorts: (i) a single-dosing cohort, comprising 6 DILT1D patients[18] treated with a single dose of IL-2 ranging from 0.6 to 1.5 x 10^6 IU/m^2; and (ii) a multiple dosing cohort, comprising 5 DILfrequency patients from the three-day dosing regimen, treated with IL-2 doses ranging from 0.2 to 0.32 × 10^6 IU/m^2. Study participants' characteristics and immune profiling at baseline are summarised in **Supplementary Table 1**.

Flow cytometry

Flow cytometric characterisation of fresh whole-blood samples from the DILfrequency study participants was performed at each visit within 4 h of phlebotomy, as previously described[20]. Briefly, 150 µl whole blood were incubated for 45 min at room temperature with fluorochrome-conjugated antibodies (**Supplementary Table 2, 2nd panel**). Red blood cells were then lysed (BD FACS Lysing solution). The absolute number of the main lymphocyte populations, including $CD4^+$ T, $CD8^+$ T and $CD56^+$ NK cells, was assessed using a whole-blood BD Multitest 6-Color TBNK assay using BD Trucount Tubes according to the manufacturers' instructions (BD Biosciences) at each visit. Absolute numbers of $CD4^+$ Tregs and Tconvs, and $CD56^{br}$ and $CD56^{dim}$ NK cells were derived by multiplying the absolute number of $CD4^+$T cells and $CD56^+$ NK cells by the appropriate percentages derived from the panel described above.

For the intracellular immunostainings, cryopreserved PBMCs were thawed at 37°C and resuspended drop-by-drop in X-VIVO 15 (Lonza) with 1% heat-inactivated, filtered human AB serum (Sigma). PBMC samples were selected from 10 visits (Days 0, 1, 2, 3, 4, 5, 6, 9, 14 and 28) from each patient from the single-dosing and 4 visits (Days 0, 3, 27 and 55) for the multiple dosing cohort. PBMCs were then washed in PBS, incubated with Fixable Viability Dye eFluor 780 (eBioscience) for 15 min at 4°C and stained with fluorochrome-conjugated antibodies against surface-expressed markers (**Supplementary Table 2)** for 45 min at 4ºC. Fixation and permeabilisation was performed using the FOXP3 Fix/Perm Buffer Set (eBioscience) according to the manufacturer's instructions, and cells were then stained with fluorochrome-conjugated antibodies against intracellular markers (**Supplementary Table 2)** for 1 h at room temperature.

Immunostained samples were acquired on a BD Fortessa (BD Biosciences) flow cytometer with FACSDiva software (BD Biosciences) and analysed using FlowJo (Tree Star, Inc.). Information for all fluorochrome-conjugated antibody panels used in this study is provided in Supplementary Table 2.

In vitro Treg suppression assay

A total of 12 DILfrequency participants were selected for this analysis, including nine participants that were also included in the single-cell analyses. For each participant, cells sampled from three time points were used: Day 0, Day 24 and Day 55. Cryopreserved PBMCs were thawed as

described above and stained with a cocktail of monoclonal antibodies (**Supplementary Table 2**) for cell sorting. Suppression assays were established in V-bottom 96-well plates by sorting 500 $CD4^+CD25^{-/lo}CD127^+$ effector T cells (Teffs) in the presence or absence of $CD4^+CD25^{high}CD127^{low}$ Tregs at various ratios (Treg:Teff 0:1, 1:4, 1:2 and 1:1) with 1×10^3 $CD19^+$ B cells, using the BD FACSAria III flow cytometer automated cell deposition unit (BD Biosciences). Cells were sorted into in 150 µl X-VIVO 15 supplemented with Penicillin-Streptomycin-Fungizone (Gibco) and 10% heat-inactivated, filtered human AB sera, stimulated with PHA (4 µg/ml; Alere) and incubated at 37°C, 5% CO_2, for 5 days. Proliferation was assessed by the addition of 0.5 µCi/well [3H] thymidine (PerkinElmer) for the final 20 h of co-culture. Conditions were run in 5 replicates, and proliferation readings (counts per minute [CPM]) averaged. Two samples with averaged proliferation less than 1,000 CPM from the Teff wells alone were excluded from the analysis. The percentage suppression in each culture was calculated using the following formula: percent suppression = 100 − [(CPM in the presence of Tregs ÷ CPM in the absence of Tregs) × 100]. All time points from a participant were analysed concurrently.

Single-cell multiomics: cell preparation and capture

Single-cell multiomics profiling was performed using the BD Rhapsody system on PBMC aliquots from 13 of the DILfrequency participants treated with the 3-day interval dosing schedule (**Supplementary Table 1**) collected at the baseline visit (Day 0), 3 days after the last dose of IL-2, immediately prior to the last IL-2 infusion of the dosing phase (Day 27) and one month after the last dose of IL-2 (Day 55). Cryopreserved PBMCs were thawed at 37°C and resuspended drop-by-drop in X-VIVO 15 with 1% heat-inactivated, filtered human AB serum. After washing in PBS, cells were incubated with Fixable Viability Dye eFluor 780 (eBioscience) for 10 min at room temperature, washed with cold PBS + 2% FBS and incubated for 30 min at 4ºC with fluorochrome-conjugated antibodies for sorting (**Supplementary Table 2**). Cells were then washed two times and resuspended in cold PBS + 1% FBS for cell sorting at 4ºC in a BD FACSAria Fusion sorter (BD Biosciences). The following T and NK cell subsets were sorted from each participant at each visit: (i) $CD3^-CD56^{hi}$ ($CD56^{br}$ NK; (ii) $CD3^-CD56^+$ ($CD56^{dim}$ NK; (iii) $CD3^+CD8^+$ ($CD8^+$ T); (iv) $CD3^+CD4^+$ $CD25^{-/low}$ ($CD4^+$ Tconv); and (v) $CD3^+CD4^+$ $CD127^{low}CD25^{hi}$ ($CD4^+$ Treg). We

aimed to sort a total of 130,000 cells for the Day 0 and Day 55 visits and 160,000 for the Day 27 visit, with the following proportion of each of the sorted cell populations: 30% $CD4^+$ Treg; 25% $CD4^+$ Tconv and $CD8^+$ T; 12% $CD56^{br}$ NK and 8% $CD56^{dim}$ NK cells.

Following cell sorting, each sorted subset was labelled with the respective sample barcoding antibody (sample multiplexing kit; BD Biosciences) for 20 min at 4ºC to allow for the identification of the sorting gate and visit of each captured single cell. To minimise day-to-day variation, we processed the three PBMC samples corresponding to the three visits from each participant on the same day. As the number of barcoded oligo-conjugated antibodies available in the kit was less than the total number of sorted subsets, we combined the $CD4^+$ Treg and $CD56^{dim}$ NK cells as well as the $CD4^+$ Tconv and $CD56^{br}$ NK cells from each visit and labelled the pooled cells with the same barcode. These combined subsets were chosen for their highly differentiated transcriptional and proteomics profile, which allowed robust separation of the respective original subsets at the analysis stage. Cells were then washed three times with BD Sample Buffer (BD Biosciences) at 4ºC to remove any residual unbound barcoding antibody and then pooled together for downstream processing.

To profile unstimulated cells, half of the pooled cells volume (corresponding to ~210,000 cells) were initially incubated at 4ºC for 5 min with human Fc block (BD Biosciences) and then for a further 45 min with a master mix of 65 oligo-conjugated AbSeq antibodies (BD Bioscience; **Supplementary Table 2**). Cells were then washed three times with BD Sample Buffer at 4ºC to remove residual unbound oligo-conjugated AbSeq antibodies, resuspended in 500 ul cold BD Sample buffer and filtered through a sterile 50 µm Filcon cup-type filter (BD Biosciences) for cell counting. Samples were then resuspended in 620 µl of cold BD sample buffer at a concentration of 40 cells/µl - for an estimated capture rate of ~20,000 single-cells / cartridge - and immediately loaded on two BD Rhapsody cartridges (BD Biosciences) for single-cell capture.

For *in vitro* stimulation, the remaining volume from the pooled cells was washed at 4ºC and resuspended in X-VIVO 15 + 10% heat-inactivated, filtered human AB serum at a final concentration of 2×10^6 cells/ml. A volume of 100 µl (~200,000 cells) was then incubated in one well of a round-bottom 96-well plate at 37ºC for 90 minutes with a PMA and ionomycin cell stimulation cocktail (eBioscience), in the absence of protein transport inhibitors. Cells were

harvested into a FACS tube, washed with PBS + 2% FBS and processed for cell capture, as detailed above for the unstimulated cells.

Single-cell multiomics: cDNA library preparation and sequencing

Single-cell capture, and cDNA library preparation was performed using the BD Rhapsody Express single-cell analysis system (BD Biosciences), according to the manufacturer's instructions. cDNA was initially amplified for 11 cycles (PCR1) using the pre-designed Human T-cell Expression primer panel (BD Biosciences) containing 259 primer pairs, together with a custom designed primer panel containing 306 primer pairs (BD Biosciences), described previously[20]. A total of 565 primer pairs targeting 534 different genes were targeted for amplification with this targeted panel (**Supplementary Table 2**).

The resulting PCR1 products were purified using AMPure XP magnetic beads (Beckman Coulter) and the respective mRNA and AbSeq/sample tag products were separated based on size selection, using different bead ratios (0.7× and 1.2×, respectively). The purified mRNA and sample tag PCR1 products were further amplified (10 cycles) using a nested PCR approach and the resulting PCR2 products purified by size selection (0.8× and 1.2× for the mRNA and sample tag libraries, respectively). The concentration, size and integrity of the resulting PCR products was assessed using both Qubit (High Sensitivity dsDNA kit; Thermo Fisher) and the Agilent 4200 Tapestation system (Agilent). The final products were normalised to 2.5 ng/µl (mRNA), 1.1 ng/µl (sample tag) and 0.35 ng/µl (AbSeq) and underwent a final round of amplification (six cycles for mRNA and sample tag and 7 cycles for AbSeq) using indexes for Illumina sequencing to prepare the final libraries. Final libraries were quantified using Qubit and Agilent Tapestation and pooled (~29/67/4% mRNA/AbSeq/sample tag ratio) to achieve a final concentration of 5 nM. Final pooled libraries were spiked with 15% PhiX control DNA to increase sequence complexity and sequenced (150 bp paired-end) on a NovaSeq 6000 sequencer (Illumina).

630 **Pre-processing of single-cell sequencing data**

631 The single-cell sequencing reads were processed following instructions from BD Biosciences
632 described earlier[27], with slight modifications. First, low-quality read pairs were removed based on
633 read length, mean base quality score and highest single-nucleotide frequency. High-quality R1
634 reads were analysed to extract cell labels and unique molecular identifier (UMI) sequences. High-
635 quality R2 reads were aligned to the reference panel sequences using Bowtie2[70]. Reads having the
636 identical cell labels and UMI sequences and aligned to the same gene were collapsed into a single
637 molecule. To correct sequencing and PCR errors, the obtained counts were adjusted by a recursive
638 substitution error correction (RSEC) algorithm developed by BD Biosciences. The sampling time
639 point and sorting gate of origin of each cell were labelled using information from barcoded oligo-
640 conjugated antibodies. Cells without barcoding information were labelled as "tag N/A", and cells
641 with two or more barcodes were labelled as "multiplet". We note that sample barcoding and AbSeq
642 staining efficiency was compromised in $CD56^{br}$ NK cells. As the quality of the main mRNA library
643 was not affected by this technical issue, $CD56^{br}$ NK cells without barcoding information were
644 included in the quality control and clustering step, but excluded from subsequent analyses
645 dependent on sampling time point (see below). This led to a significant reduction in the number of
646 $CD56^{br}$ NK cells analysed and a concomitant reduction in statistical power to identify IL-2-induced
647 alterations. Nevertheless, we also note that our cell-enrichment strategy compensated for this cell
648 loss due to technical reasons and provided sufficient resolution to dissect the heterogeneity of the
649 rare population of $CD56^{+}$ NK cells.

650

651 **Doublet scoring**

652 Doublet scoring was performed on each sample separately using Scrublet[71]. Briefly, this method
653 simulates synthetic doublets by sampling pairs of cells and then scores each cell by its similarity
654 to the simulated doublets. For each sample, count matrices for RNA and AbSeq data were
655 concatenated and used as the input. The method was modified to exclude known multiplet-tagged
656 cells from the doublet simulation while retaining them for scoring. The doublet score was used to
657 help identify clusters of doublets in subsequent quality control stages.

658

659 **Normalisation, integration, dimensionality reduction and clustering**

660 Data normalisation was performed using Seurat[72]. The RNA count matrices were normalised by
661 log normalisation. Specifically, the RNA counts for each cell were (i) divided by the total counts
662 for that cell, (ii) multiplied by a scale factor of 10,000, and (iii) natural-log transformed after
663 adding one pseudo count. The AbSeq counts for each cell were considered compositional and
664 normalised by a centred log ratio transformation[73]. Normalised RNA and AbSeq expression
665 matrices were then centred and scaled. Specifically, each feature was linearly regressed against
666 selected latent variables including the number of RNA and AbSeq features, and the donor of origin,
667 where appliable. The resulting residuals were mean-centred and divided by their standard
668 deviations.

669 Integration of the scaled AbSeq expression matrices from different participants were performed
670 using a combination of canonical correlation analysis (CCA) and identification of mutual nearest
671 neighbours (MNNs), implemented in Seurat[72]. After integration was performed, the updated
672 AbSeq expression matrices produced by the integration algorithm were used in subsequent
673 dimensionality reduction and clustering.

674 Dimensionality reduction and clustering were performed using Seurat[72]. Specifically, principal
675 components (PCs) were calculated separately for each assay using the top variable features of the
676 scaled or integrated expression matrices, and a weighted nearest neighbour (WNN) graph as well
677 as a weighted shared nearest neighbour (WSNN) graph were generated on the ten top PCs from
678 each assay, unless otherwise specified. We used $k = 30$ nearest neighbours for each cell. Uniform
679 Manifold Approximation and Projection (UMAP)[74] embeddings were then calculated based on the
680 WNN graph. The Louvain algorithm[75] was applied to identify clusters of cells based on a WSNN
681 graph, at the selected resolution level. Clusters with fewer than ten cells were removed. The
682 resulting clusters were manually annotated based on marker genes and sorting gate information to
683 elucidate cell types and label suspicious clusters.

684

685 **Data quality control**

686 The BD Rhapsody single-cell sequencing data generated in this study was processed through a
687 pipeline consisting of multiple quality control steps as described below. Methodological details of
688 each step are specified in previous sections. The single-cell sequencing data of each sample (i.e.
689 the collection of stimulated and unstimulated cells for a single participant) were pre-processed to
690 obtain two annotated count matrices (RNA and AbSeq). We performed data normalisation,
691 dimensionality reduction and clustering for each sample. Specifically, 30 RNA principal
692 components (PCs) and 30 AbSeq PCs were used to generate the WNN and WSNN graphs, and
693 clustering was performed at resolution 0.5.

694 Within each sample, cells meeting one of the following criteria were removed: (1) cells that are
695 labelled as "multiplet" or in clusters with high doublet scores; (2) cells labelled as "tag N/A",
696 except those in clusters annotated as $CD56^{br}$; (3) cells in clusters with very low RNA counts and
697 very low or very high AbSeq counts; (4) cells in clusters annotated as monocyte or B cell
698 contamination; (5) cells labelled as DN T cells.

699 The filtered cells from each participant were merged according to the stimulation status into two
700 datasets (unstimulated cells and *in vitro* stimulated cells). Both stimulated and unstimulated cells
701 were then processed in the same way unless otherwise specified. We performed data normalisation,
702 dimensionality reduction and clustering for each merged dataset. Specifically, clustering was
703 performed at resolution 0.7 (unstimulated cells) or 1.5 (stimulated cells). Doublet clusters were
704 manually annotated and removed. Data normalisation, dimensionality reduction and clustering
705 were performed again. Specifically, clustering was performed at resolution 0.5.

706 Cells in each filtered dataset were subsequently partitioned into four major groups ($CD4^+$ Treg,
707 $CD4^+$ Tconv, CD8+ T and $CD56^+$ NK cells) based on cluster annotations and sorting gates of
708 origin. In addition, unstimulated cells in clusters marked by genes related to cell cycle were
709 grouped as cycling cells. We chose to partition cycling cells into one separate group based on the
710 following considerations: (i) cycling cells were relatively rare in numbers (0.72% of total
711 unstimulated cells); (ii) cycling cells clusters had well-defined mRNA markers; (iii) The
712 phenotypical differences between cycling cells and their non-cycling counterparts were potentially
713 larger than the heterogeneity within each major cell populations.

After partitioning, doublet clusters were manually annotated and removed. Data normalisation, dimensionality reduction, integration and clustering were performed in each group of partitioned cells. Specifically, clustering was performed at resolution 0.5. Finally, data normalisation, dimensionality reduction, and clustering were performed again.

Owing to the aforementioned technical limitations with AbSeq staining in CD56^{br} NK cells, AbSeq data was not used in dimensionality reduction and clustering of NK cells. The following resolutions were used for the final clustering: unstimulated Tregs, 0.6; unstimulated Tconvs, 0.5; unstimulated CD8, 0.5; unstimulated NK, 0.3; unstimulated cycling cells, 0.5; stimulated Tregs, 0.5; stimulated Tconvs, 0.4; stimulated CD8: 0.5; stimulated NK: 0.5. The resulting partitioned datasets were used for subsequent analyses. We note that one PBMC aliquot (corresponding to the Day 55 visit of Participant 8) yielded very low cell numbers (N = 603 unstimulated and N = 67 stimulated cells) and displayed a compromised FACS staining profile. These cells were included in quality control and clustering procedures but excluded from downstream analyses. All other 38 samples corresponding to 38 visits yielded the expected cell frequencies and numbers.

Single-cell proliferation scores

Single-cell proliferation scores were calculated using a previously described approach[76], which is based on the average normalised expression levels of a pre-selected set of 11 mRNA features related to cell cycle (*AURKB*, *HMGB2*, *HMMR*, *MCM4*, *MKI67*, *PCLAF*, *PCNA*, *TK1*, *TOP2A*, *TYMS*, and *UBE2C*), subtracted by the aggregated expression of a control set of 50 randomly selected mRNA features. The proliferation scores were used to identify two cycling clusters from the 15 functional T and NK cell subsets identified in blood from the initial clustering (**Supplementary Fig. 3a**). We noted that the distinct co-expression of these cell-cycle genes present in our targeted transcriptional panel superseded more subtle functional differences and aggregated all cycling T and NK cells into two respective clusters, regardless of their original sorting gate. Given this lack of functional differentiation and to avoid the potential overwhelming effect of these cell-cycle genes on the resulting clustering visualisation, we opted to separate these cycling T and NK cells from the rest of the cells included in subsequent clustering steps to assess IL-2-induced changes in their relative frequency in blood.

Cluster annotation

Functional annotation of the resulting clusters was performed manually based on the cluster-specific differential expression of the mRNA and protein markers (summarised in **Supplementary Data 1**). Sample tagging information, corresponding to sorting gate information, was used to sub-cluster the five main immune populations ($CD4^+$ $CD127^{low}CD25^{hi}$ Treg; $CD4^+$ $CD25^{-/low}$ Tconv; $CD8^+$ T; $CD56^{br}$ NK and $CD56^{dim}$ NK cells). The use of a bespoke targeted single-cell approach combined with a cell-subset enrichment strategy provided a high-resolution map of the heterogeneity of these cell populations – and particularly of the rare circulating $CD4^+$ Treg and $CD56^{br}$ NK cell subsets.

We note that a consequence of the cell-subset enrichment strategy used in this study is that the frequency of the T and NK cell subsets described in this dataset do not directly represent their frequency in whole blood. The aim of this study was not to identify changes in the global composition of PBMCs, but to specifically focus on the T and NK cell subsets. The pre-purification of the Treg and $CD56^{br}$ NK subsets was central to the resolution of this approach and provided greater power to dissect their functional heterogeneity and investigate how their relative composition was modified by LD-IL-2 immunotherapy

Functional annotation of $CD4^+$ $CD127^{low}CD25^{hi}$ T cell clusters

Owing to our cell-subset enrichment strategy, we obtained a high-resolution map depicting the heterogeneity of $CD127^{low}CD25^{hi}$ T cells in blood, with 13 distinct clusters identified in unstimulated cells (**Supplementary Fig. 4a**) and 12 in *in vitro* stimulated cells (**Supplementary Fig. 4b**). Overall, we found consistency in the functional annotation of the identified subsets in stimulated and unstimulated cells, with a clear demarcation of the naïve and memory subsets.

Expression of the canonical Treg transcription factors *FOXP3* and *IKZF2* (encoding HELIOS) was used to identify three distinct groups of clusters, corresponding to different populations of $CD127^{low}CD25^{hi}$ T cells: (i) $CD45RA^+$ $FOXP3^+HELIOS^+$ clusters (depicted in green)

corresponding to thymic-derived naïve Tregs; (ii) CD45RA$^-$ FOXP3$^+$HELIOS$^+$ clusters (depicted in blue) corresponding to memory Tregs with suppressive function; and (iii) CD45RA$^-$ CD25$^+$ FOXP3$^-$HELIOS$^-$ clusters (depicted in red) corresponding to a small subset of Teffs expressing CD25 likely due to recent activation (**Supplementary Fig. 5**). Additional clusters showing variable expression of FOXP3 but lack of HELIOS expression (FOXP3$^+$HELIOS$^-$ clusters) were depicted in black, and represent a more heterogeneous group of Treg subsets, containing a mix of thymic-derived and induced Treg subsets.

As expected, most of the cells within the CD127^{low}CD25^{hi} Treg gate showed concomitant expression of FOXP3 and HELIOS, which is consistent with their largely demethylated *FOXP3* Treg-specific demethylated region (TSDR)[37], the hallmark of *bona fide* thymic Tregs. Furthermore, we were able to identify a trajectory of thymic Treg differentiation, originating from the naïve FOXP3$^+$HELIOS$^+$ Tregs (cluster 0). Memory FOXP3$^+$HELIOS$^+$ Tregs displayed more heterogeneity and included four distinct subsets in unstimulated cells, including a cluster of CD80$^+$ Tregs characterised by elevated expression of tissue-homing receptors (cluster 7) and a cluster of effector Tregs (cluster 1) typically marked by the expression of HLA class II and other effector Treg markers such as CD39 and GITR (**Supplementary Fig. 4a**). We have also identified a subset of CD45RA$^+$ naïve cells (cluster 2) showing much lower expression of FOXP3 and HELIOS compared to the classical naïve Treg cluster. This likely corresponds to a subset of homeostatically-expanded CD45RA$^+$ T cells upregulating CD25 that we have previously characterised[77]. Consistent with this non-Treg profile, these CD25$^+$ naïve T cells upregulated the expression of IL-2 upon *in vitro* stimulation (**Supplementary Fig. 5f**). The expression of IL-2 in stimulated cells was also a hallmark of the CD25$^+$ FOXP3$^-$HELIOS$^-$ Teff clusters and allowed us to further refine their functional heterogeneity. Moreover, the relative frequency of CD45RA$^-$ FOXP3$^-$HELIOS$^-$ cells identified in this single-cell dataset is consistent with the frequency of cells identified by FACS as cytokine-producing FOXP3$^-$HELIOS$^-$ cells in the CD127^{low}CD25^{hi} Treg gate that we have previously shown to contain a methylated TSDR[37], further indicating that they correspond to a small proportion of activated CD25$^+$ FOXP3$^-$HELIOS$^-$ Teffs captured in the CD127^{low}CD25^{hi} Treg gate.

Functional annotation of CD56^{+} NK cell clusters

In contrast to T cells, we found much lower heterogeneity in NK cells (**Fig. 4d** and **Supplementary Fig. 13**). In addition, the technical issue affecting the efficiency of the AbSeq staining on CD56^{br} NK cells, precluded the use of protein data for the clustering and annotation of the CD56^{+} NK cells, which also contributed to a lower resolution of the clusters. Nevertheless, our cell-enrichment strategy allowed us to generate a comprehensive single-cell map of NK cell heterogeneity, most notably of the rare, IL-2-sensitive CD56^{br} NK population. We observed differentiation of CD56^{br} NK cells from a rare progenitor subset marked by the expression of genes associated with haematopoiesis such as SOX4 and KIT, and characterization of two functional subsets associated with a trajectory of CD56^{br} NK cell maturation, which was marked by HLA class II gene expression in the more differentiated cells. In contrast, CD56^{dim} NK cells showed a distinct transcriptional profile of two distinct subsets, reflecting a gradient of NK cell activation associated with the acquisition of a cytotoxic profile (**Fig. 4d** and **Supplementary Fig. 13**). These findings support a distinct functional differentiation between the CD56^{dim} and CD56^{br} subsets, which allowed clear identification a fraction of CD56^{dim} NK cells sorted in the CD56^{br} gate, as well as a fraction of CD56^{br} NK cells sorted within the CD56^{dim} gate (**Fig. 4e**).

Differential abundance analysis

To identify specific cell frequency changes across different sampling time points, we calculated the frequency of each cell type annotated. A cell type was defined as a group of cells from the same cluster or several similar clusters, after removing cells not sorted from the corresponding gate. The frequency of each cell type for each participant and each time point was calculated as the proportion of that cell type within all cells from the same participant, time point and sorting gate of origin. For each cell type, a two-sided Wilcoxon signed-rank test was performed to compare the frequencies at Day 0 with the frequencies at Day 27 or Day 55 in the 13 participants selected for single-cell analysis. Benjamini-Hochberg FDR correction was applied after pooling all resulting *P* values. For each cell type and each participant, the $\log_2$ fold change values between corresponding frequency values were calculated and visualised. We note that cells were compared

827 only if they were from the same sorting gate, as cells from different sorting gates were pooled in
828 designated proportions that are not biologically relevant.

829

830 **Generation and normalisation of pseudo-bulk expression data**

831 For the DILfreq dataset, unstimulated and stimulated cells were separately partitioned into five
832 groups (Treg, Tconv, CD8, CD56^{br} and CD56^{dim}), after removing cells not sorted from the
833 corresponding gate. In each group, cells from the same participant, time point and stimulation
834 status were aggregated into one pseudo-bulk sample by summarising raw counts of each mRNA
835 or AbSeq feature. For the COMBAT and INCOV datasets, the pseudo-bulk expression data for
836 each participant and each cell type were obtained from the authors, and samples with less than
837 2,000 total RNA counts were removed. For the INCOV dataset, samples from non-COVID-19,
838 immunocompromised or immunosuppressed participants were additionally removed.

839

840 **Differential expression analysis**

841 Differential expression analysis was performed separately for RNA and AbSeq data from raw
842 pseudo-bulk counts using DESeq2[78]. Specifically, the likelihood ratio test was used, with a full
843 model including time points and the participants as independent variables, and a reduced model
844 including only participants as the independent variable. The apeglm method[79] was applied to
845 shrink the resulting fold change values, and the Benjamini-Hochberg FDR correction was applied
846 after pooling all resulting *P* values (**Supplementary Data 2**). Genes with either (i) absolute log2
847 fold change values equal to or greater than 0.4 and FDR-adjusted *P* values less than 0.01, or (ii)
848 FDR-adjusted *P* values less than 1×10^{-10}, were selected as significantly differentially expressed
849 genes, unless otherwise noted. Participant-specific $\log_2$ fold change values were calculated directly
850 from the normalised pseudo-bulk expression data.

851

852 **Day 55 signature scores**

Forty-one genes that were significantly upregulated or downregulated in at least one unstimulated cell population comparing Day 55 with Day 0 were defined as Day 55 signature genes, from which the Day 55 signature scores were calculated. Within each dataset, the Day 55 signature score was defined for each pseudo-bulk sample as the sum of z-scores of normalised expression levels of upregulated signature genes, subtracted by that of downregulated signature genes. For each participant and cell type in the DILfrequency dataset, the Δ signature scores were defined as the signature score differences between Day 27 or Day 55 and Day 0, as indicated.

Pseudo-time trajectory analysis

Pseudo-time trajectory analysis was performed using Slingshot[80] and tradeSeq[81]. First, 10-dimensional UMAP embeddings were generated for stimulated $CD4^+$ T cells based on RNA and AbSeq data, as described above. Second, the Slingshot algorithm was applied to UMAP data and the manually annotated cluster labels, with naïve cells selected as the starting point, and other parameters set to default. Finally, the resulting pseudo-time data were used as the input for the tradeSeq algorithm to model the expression levels of each gene along each trajectory.

Data availability

The single-cell sequencing data generated in this study have been deposited in Gene Expression Omnibus (GEO) under accession code GSE201197 (https://www.ncbi.nlm.nih.gov/geo/query/acc.cgi?acc=GSE201197).

Code availability

The custom code used in the study for data analyses and visualisation has been deposited in Zenodo (https://doi.org/10.5281/zenodo.7116340).

Acknowledgements

We thank all participants in DILT1D and DILfrequency for their generous contribution to this study. The authors also acknowledge the support of the NIHR Cambridge Biomedical Research Centre and the Cambridge Clinical Trial Unit for trial coordination; the NIHR/Wellcome Trust Clinical Research Facility and Addenbrooke's Centre for Clinical Investigation for clinical facilities; the Department of Clinical Immunology, Addenbrooke's Hospital; the JDRF/Wellcome Diabetes and Inflammation laboratory sample processing team (led by Helen Stevens) and information technology and administration team (led by Judy Brown) and data teams at the Cambridge Institute for Medical Research. We thank Shannah Donhou, Sarune Kacinskaite and Heather McMurray, University of Oxford for sample collection and preparation, and members of the Diabetes and Inflammation Laboratory for critical discussion. We thank Justin Whalley, Georgina Kerr, Brian Marsden and Julian Knight, University of Oxford, for providing access to clinical data collected from the COMBAT cohort. We also thank Yapeng Su, and Dan Yuan from Institute for Systems Biology, and Jason D. Goldman from Swedish Medical Center, for providing access to the annotated single-cell data collected from the INCOV cohort.

Funding

This work was supported by the Sir Jules Thorn Trust (13/JTA (OCT2013/DR/1044)), the JDRF (1-SRA-2019-657-A-N), and the NIHR Cambridge Biomedical Research Centre. The Diabetes and Inflammation Laboratory was supported by a strategic award from the Wellcome (107212/A/15/Z) and the JDRF (4-SRA-2017-473-A-A). JYZ was supported by the China Scholarship Council-University of Oxford Scholarship. The research was supported by the Wellcome Trust Core Award Grant Number 203141/Z/16/Z with additional support from the NIHR Oxford BRC. The University of Cambridge has received salary support for M.L.E. through the National Health Service in the East of England through the Clinical Academic Reserve. The views expressed are those of the author(s) and not necessarily those of the NHS, the NIHR or the Department of Health.

Author contributions

L.S.W., J.A.T. and R.C.F. conceptualised this work and designed the experiments. M.L., L.G. and R.C.F. performed the scRNA-seq experiments. J-Y.Z. led the analysis of the scRNA-seq data with help from F.H. and D.T. M.M. and J.H.M.Y. performed the in vitro suppression experiments and analysed the data under the supervision of T.I.M.T. M.L.P. and R.C.F. performed FACS experiments and analysed the data. J.K., F.W-L. and M.L.E. supervised the DILfrequency study. T.I.M.T. provided conceptual advice on the experiments. J-Y.Z., L.S.W, J.A.T. and R.C.F. wrote the manuscript with input from all authors.

Competing interests

F.W-L. is employed by Vertex Pharmaceuticals; J.A.T. is a member of the GSK Human Genetics Advisory Board. The remaining authors declare no competing interests.

References

1. Koreth, J. *et al.* Interleukin-2 and Regulatory T Cells in Graft-versus-Host Disease. *New Engl J Med* **365**, 2055–2066 (2011).
2. Saadoun, D. *et al.* Regulatory T-Cell Responses to Low-Dose Interleukin-2 in HCV-Induced Vasculitis. *New Engl J Med* **365**, 2067–2077 (2011).
3. Castela, E. *et al.* Effects of Low-Dose Recombinant Interleukin 2 to Promote T-Regulatory Cells in Alopecia Areata. *JAMA Dermatol* **150**, 748–751 (2014).
4. von Spee-Mayer, C. *et al.* Low-dose interleukin-2 selectively corrects regulatory T cell defects in patients with systemic lupus erythematosus. *Ann Rheum Dis* **75**, 1407–1415 (2016).
5. Zhao, T. X. *et al.* Low-dose interleukin-2 in patients with stable ischaemic heart disease and acute coronary syndromes (LILACS): protocol and study rationale for a randomised, double-blind, placebo-controlled, phase I/II clinical trial. *BMJ Open* **8**, e022452 (2018).
6. He, J. *et al.* Efficacy and safety of low-dose IL-2 in the treatment of systemic lupus erythematosus: a randomised, double-blind, placebo-controlled trial. *Ann Rheum Dis* **79**, 141–149 (2020).
7. Klatzmann, D. & Abbas, A. K. The promise of low-dose interleukin-2 therapy for autoimmune and inflammatory diseases. *Nat Rev Immunol* **15**, 283–294 (2015).
8. Graßhoff, H. *et al. Low-Dose IL-2 Therapy in Autoimmune and Rheumatic Diseases*. *Front Immunol* **12**, e648408 (2021).
9. Kolios, A. G. A., Tsokos, G. C. & Klatzmann, D. Interleukin-2 and regulatory T cells in rheumatic diseases. *Nat Rev Rheumatol* **17**, 749–766 (2021).
10. Ghosh, S. *et al.* Polygenic control of autoimmune diabetes in nonobese diabetic mice. *Nat Genet* **4**, 404–409 (1993).
11. Todd, J. A. Etiology of Type 1 Diabetes. *Immunity* **32**, 457–467 (2010).
12. Hulme, M. A., Wasserfall, C. H., Atkinson, M. A. & Brusko, T. M. Central Role for Interleukin-2 in Type 1 Diabetes. *Diabetes* **61**, 14–22 (2011).
13. Yamanouchi, J. *et al.* Interleukin-2 gene variation impairs regulatory T cell function and causes autoimmunity. *Nat Genet* **39**, 329–337 (2007).
14. Tang, Q. *et al.* Central Role of Defective Interleukin-2 Production in the Triggering of Islet Autoimmune Destruction. *Immunity* **28**, 687–697 (2008).
15. Hartemann, A. *et al.* Low-dose interleukin 2 in patients with type 1 diabetes: a phase 1/2 randomised, double-blind, placebo-controlled trial. *Lancet Diabetes Endocrinol* **1**, 295–305 (2013).
16. Rosenzwajg, M. *et al.* Low-dose interleukin-2 fosters a dose-dependent regulatory T cell tuned milieu in T1D patients. *J Autoimmun* **58**, 48–58 (2015).
17. Rosenzwajg, M. *et al.* Low-dose IL-2 in children with recently diagnosed type 1 diabetes: a Phase I/II randomised, double-blind, placebo-controlled, dose-finding study. *Diabetologia* **63**, 1808–1821 (2020).
18. Todd, J. A. J. *et al.* Regulatory T cell responses in participants with type 1 diabetes after a single dose of interleukin-2: a non-randomised, open label, adaptive dose-finding trial. *PLoS Med* **13**, e1002139 (2016).

19. Seelig, E. *et al.* The DILfrequency study is an adaptive trial to identify optimal IL-2 dosing in patients with type 1 diabetes. *JCI Insight* **3**, (2018).
20. Trzupek, D. *et al.* Single-cell multi-omics analysis reveals IFN-driven alterations in T lymphocytes and natural killer cells in systemic lupus erythematosus. *Wellcome Open Res* **6**, (2021).
21. Kenefeck, R. *et al.* Follicular helper T cell signature in type 1 diabetes. *J Clin Invest* **125**, 292–303 (2015).
22. Ferreira, R. C. *et al.* IL-21 production by CD4+ effector T cells and frequency of circulating follicular helper T cells are increased in type 1 diabetes patients. *Diabetologia* **58**, 781–790 (2015).
23. Ekman, I. *et al.* Circulating CXCR5−PD-1hi peripheral T helper cells are associated with progression to type 1 diabetes. *Diabetologia* **62**, 1681–1688 (2019).
24. von Herrath, M. *et al.* Anti-interleukin-21 antibody and liraglutide for the preservation of β-cell function in adults with recent-onset type 1 diabetes: a randomised, double-blind, placebo-controlled, phase 2 trial. *Lancet Diabetes Endocrinol* **9**, 212–224 (2021).
25. Bell, C. J. M. *et al.* Sustained in vivo signaling by long-lived IL-2 induces prolonged increases of regulatory T cells. *J Autoimmun* **56**, 66–80 (2015).
26. Yu, A. *et al.* Selective IL-2 Responsiveness of Regulatory T Cells Through Multiple Intrinsic Mechanisms Supports the Use of Low-Dose IL-2 Therapy in Type 1 Diabetes. *Diabetes* **64**, 2172–2183 (2015).
27. Trzupek, D. *et al.* Discovery of CD80 and CD86 as recent activation markers on regulatory T cells by protein-RNA single-cell analysis. *Genome Med* **12**, 55 (2020).
28. Ito, S. *et al.* Ultra-low Dose Interleukin-2 Promotes Immune-modulating Function of Regulatory T Cells and Natural Killer Cells in Healthy Volunteers. *Mol Ther* **22**, 1388–1395 (2014).
29. Humrich, J. Y. *et al.* Low-dose interleukin-2 therapy in refractory systemic lupus erythematosus: an investigator-initiated, single-centre phase 1 and 2a clinical trial. *Lancet Rheumatol* **1**, e44–e54 (2019).
30. Uxa, S. *et al.* Ki-67 gene expression. *Cell Death Differ* **28**, 3357–3370 (2021).
31. di Rosa, F., Cossarizza, A. & Hayday, A. C. To Ki or Not to Ki: Re-Evaluating the Use and Potentials of Ki-67 for T Cell Analysis. *Front Immunol* **12**, (2021).
32. Muñoz-Ruiz, M. *et al.* Tracking immunodynamics by identification of S-G2/M-phase T cells in human peripheral blood. *J Autoimmun* **112**, 102466 (2020).
33. Ariel, A. *et al.* IL-2 Induces T Cell Adherence to Extracellular Matrix: Inhibition of Adherence and Migration by IL-2 Peptides Generated by Leukocyte Elastase. *J Immunol* **161**, 2465 (1998).
34. Franitza, S. *et al.* TNF-α Associated with Extracellular Matrix Fibronectin Provides a Stop Signal for Chemotactically Migrating T Cells. *The Journal of Immunology* **165**, 2738–2747 (2000).
35. Wrenshall, L. E., Platt, J. L., Stevens, E. T., Wight, T. N. & Miller, J. D. Propagation and Control of T Cell Responses by Heparan Sulfate-Bound IL-2. *J Immunol* **170**, 5470 (2003).
36. Miller, J. D., Clabaugh, S. E., Smith, D. R., Stevens, R. B. & Wrenshall, L. E. Interleukin-2 is present in human blood vessels and released in biologically active form by heparanase. *Immunol Cell Biol* **90**, 159–167 (2012).

37. Ferreira, R. C. *et al.* Cells with Treg-specific FOXP3 demethylation but low CD25 are prevalent in autoimmunity. *J Autoimmun* **84**, 75–86 (2017).
38. Singh, S. S. *et al.* Amphiregulin in cellular physiology, health, and disease: Potential use as a biomarker and therapeutic target. *J Cell Physiol* **237**, 1143–1156 (2022).
39. West, N. R. *et al.* Oncostatin M drives intestinal inflammation and predicts response to tumor necrosis factor–neutralizing therapy in patients with inflammatory bowel disease. *Nat Med* **23**, 579–589 (2017).
40. Richard, A. C. *et al.* Targeted genomic analysis reveals widespread autoimmune disease association with regulatory variants in the TNF superfamily cytokine signalling network. *Genome Med* **8**, 76 (2016).
41. Maña, P. *et al.* LIGHT (TNFSF14/CD258) Is a Decisive Factor for Recovery from Experimental Autoimmune Encephalomyelitis. *J Immunol* **191**, 154–163 (2013).
42. Ahern, D. J. *et al.* A blood atlas of COVID-19 defines hallmarks of disease severity and specificity. *Cell* **185**, 916-938 (2022).
43. Su, Y. *et al.* Multiple early factors anticipate post-acute COVID-19 sequelae. *Cell* **185**, 881-895.e20 (2022).
44. Whangbo, J. S. *et al.* Functional analysis of clinical response to low-dose IL-2 in patients with refractory chronic graft-versus-host disease. *Blood Adv* **3**, 984–994 (2019).
45. Whangbo, J. S. *et al.* Dose-escalated interleukin-2 therapy for refractory chronic graft-versus-host disease in adults and children. *Blood Adv* **3**, 2550–2561 (2019).
46. Bielekova, B. *et al.* Regulatory CD56bright natural killer cells mediate immunomodulatory effects of IL-2Rα-targeted therapy (daclizumab) in multiple sclerosis. *Proc Natl Acad Sci USA* **103**, 5941–5946 (2006).
47. Melsen, J. E., Lugthart, G., Lankester, A. C. & Schilham, M. W. Human Circulating and Tissue-Resident CD56bright Natural Killer Cell Populations. *Front Immunol* **7**, 262 (2016).
48. Ballesteros-Tato, A. *et al.* Interleukin-2 Inhibits Germinal Center Formation by Limiting T Follicular Helper Cell Differentiation. *Immunity* **36**, 847–856 (2012).
49. Locci, M. *et al.* Activin A programs the differentiation of human TFH cells. *Nat Immunol* **17**, 976–984 (2016).
50. He, J. *et al.* Low-dose interleukin-2 treatment selectively modulates CD4+ T cell subsets in patients with systemic lupus erythematosus. *Nat Med* **22**, 991–993 (2016).
51. Liu, S. M. *et al.* Differential IL-21 signaling in APCs leads to disparate Th17 differentiation in diabetes-susceptible NOD and diabetes-resistant NOD.Idd3 mice. *J Clin Invest* **121**, 4303–4310 (2011).
52. Crotty, S. T Follicular Helper Cell Biology: A Decade of Discovery and Diseases. *Immunity* **50**, 1132–1148 (2019).
53. Ren, H. M., Lukacher, A. E., Rahman, Z. S. M. & Olsen, N. J. New developments implicating IL-21 in autoimmune disease. *J Autoimmun* **122**, 102689 (2021).
54. Sage, P. T. & Sharpe, A. H. T follicular regulatory cells. *Immunol Rev* **271**, 246–259 (2016).
55. Jacobsen, J. *et al.* Expression of Foxp3 by T follicular helper cells in end-stage germinal centers. *Science* **373**, eabe5146 (2021).
56. Provine, N. M. & Klenerman, P. MAIT Cells in Health and Disease. *Annu Rev Immunol* **38**, 203–228 (2020).

57. Tao, H. *et al.* Differential controls of MAIT cell effector polarization by mTORC1/mTORC2 via integrating cytokine and costimulatory signals. *Nat Commun* **12**, 2029 (2021).
58. Zhou, P. *et al.* Low-dose IL-2 therapy invigorates CD8+ T cells for viral control in systemic lupus erythematosus. *PLoS Pathog* **17**, e1009858 (2021).
59. Matsumoto, A. *et al.* CIS, a Cytokine Inducible SH2 Protein, is a Target of the JAK-STAT5 Pathway and Modulates STAT5 Activation. *Blood* **89**, 3148–3154 (1997).
60. Gill, K. L., Gardner, I., Li, L. & Jamei, M. A Bottom-Up Whole-Body Physiologically Based Pharmacokinetic Model to Mechanistically Predict Tissue Distribution and the Rate of Subcutaneous Absorption of Therapeutic Proteins. *AAPS J* **18**, 156–170 (2016).
61. Bohnacker, S. *et al.* Mild COVID-19 imprints a long-term inflammatory eicosanoid- and chemokine memory in monocyte-derived macrophages. *Mucosal Immunol* (2022) doi:10.1038/s41385-021-00482-8.
62. Phetsouphanh, C. *et al.* Immunological dysfunction persists for 8 months following initial mild-to-moderate SARS-CoV-2 infection. *Nat Immunol* **23**, 210–216 (2022).
63. Marcovecchio, M. L. *et al.* Interleukin-2 Therapy of Autoimmunity in Diabetes (ITAD): a phase 2, multicentre, double-blind, randomized, placebo-controlled trial. *Wellcome Open Res* **5**, (2020).
64. Ferreira, R. C. *et al.* Chronic Immune Activation in Systemic Lupus Erythematosus and the Autoimmune PTPN22 Trp620 Risk Allele Drive the Expansion of FOXP3+ Regulatory T Cells and PD-1 Expression. *Front Immunol* **10,** 2606 (2019).
65. Sims, E. K. *et al.* Teplizumab improves and stabilizes beta cell function in antibody-positive high-risk individuals. *Sci Transl Med* **13**, eabc8980 (2021).
66. Quattrin, T. *et al.* Golimumab and Beta-Cell Function in Youth with New-Onset Type 1 Diabetes. *New Engl J Med* **383**, 2007–2017 (2020).
67. Dayan, C. M. *et al.* Preventing type 1 diabetes in childhood. *Science* **373**, 506–510 (2021).
68. Waldron-Lynch, F. *et al.* Rationale and study design of the Adaptive study of IL-2 dose on regulatory T cells in type 1 diabetes (DILT1D): a non-randomised, open label, adaptive dose finding trial. *BMJ Open* **4**, (2014).
69. Truman, L. A. *et al.* Protocol of the adaptive study of IL-2 dose frequency on regulatory T cells in type 1 diabetes (DILfrequency): a mechanistic, non-randomised, repeat dose, open-label, response-adaptive study. *BMJ Open* **5**, (2015).
70. Langmead, B. & Salzberg, S. L. Fast gapped-read alignment with Bowtie 2. *Nat Methods* **9**, 357–359 (2012).
71. Wolock, S. L., Lopez, R. & Klein, A. M. Scrublet: Computational Identification of Cell Doublets in Single-Cell Transcriptomic Data. *Cell Syst* **8**, 281-291.e9 (2019).
72. Hao, Y. *et al.* Integrated analysis of multimodal single-cell data. *Cell* **184**, 3573-3587.e29 (2021).
73. Aitchison, J. *The Statistical Analysis of Compositional Data*. (Chapman & Hall, Ltd., 1986).
74. McInnes, L., Healy, J. & Melville, J. UMAP: Uniform Manifold Approximation and Projection for Dimension Reduction. *ArXiv* **arXiv:1802**, (2018).
75. Blondel, V. D., Guillaume, J.-L., Lambiotte, R. & Lefebvre, E. Fast unfolding of communities in large networks. *Journal of statistical mechanics: theory and experiment* **2008**, P10008 (2008).

76. Itay, T. *et al.* Dissecting the multicellular ecosystem of metastatic melanoma by single-cell RNA-seq. *Science* **352**, 189–196 (2016).
77. Pekalski, M. L. *et al.* Postthymic expansion in human CD4 naive T cells defined by expression of functional high-affinity IL-2 receptors. *J Immunol* **190**, 2554–2566 (2013).
78. Love, M. I., Huber, W. & Anders, S. Moderated estimation of fold change and dispersion for RNA-seq data with DESeq2. *Genome Biol* **15**, 1–21 (2014).
79. Zhu, A., Ibrahim, J. G. & Love, M. I. Heavy-tailed prior distributions for sequence count data: removing the noise and preserving large differences. *Bioinformatics* **35**, 2084–2092 (2019).
80. Street, K. *et al.* Slingshot: cell lineage and pseudotime inference for single-cell transcriptomics. *BMC Genomics* **19**, 477 (2018).
81. van den Berge, K. *et al.* Trajectory-based differential expression analysis for single-cell sequencing data. *Nat Commun* **11**, 1201 (2020).

Figures

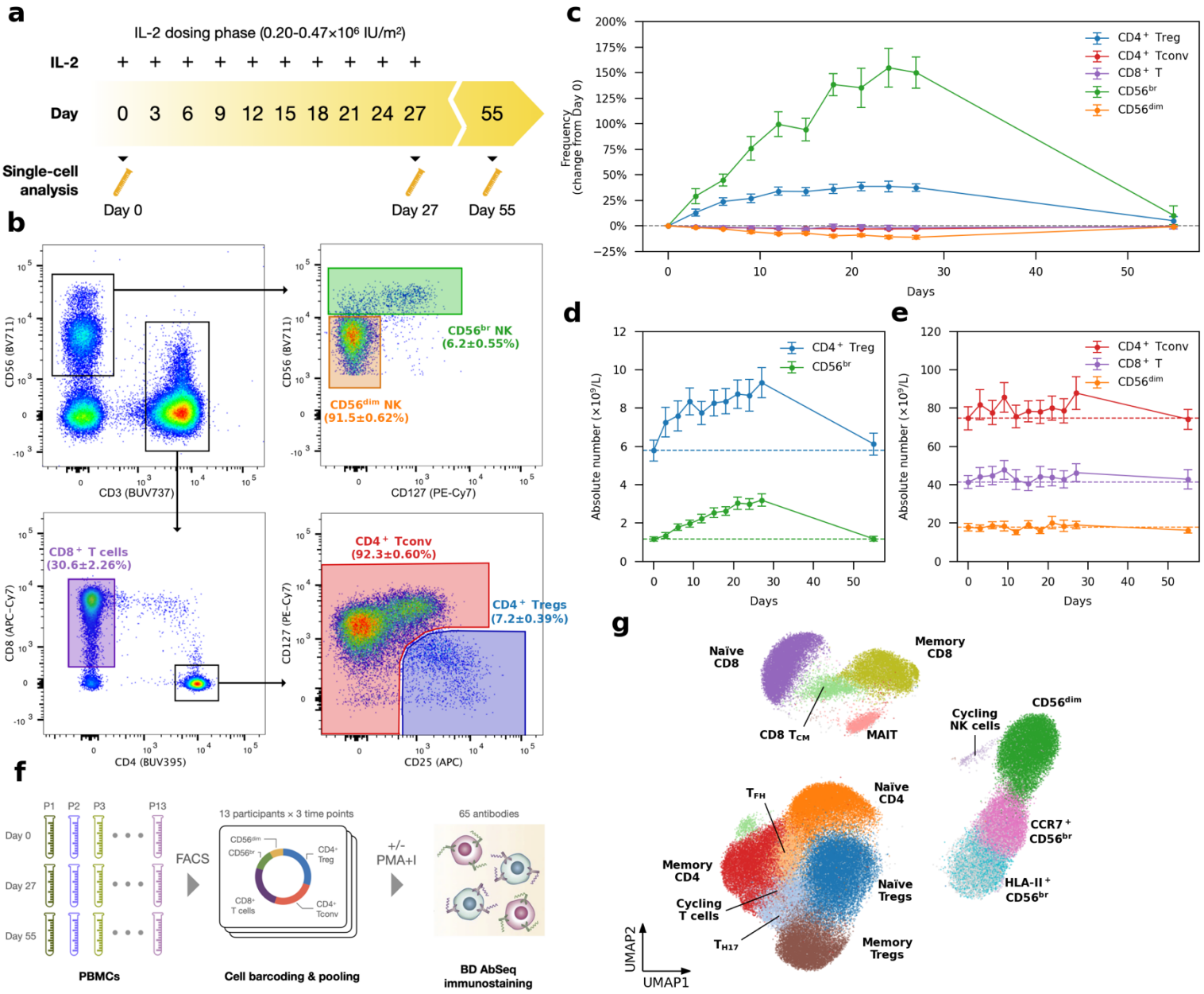

Figure 1. Interval low-dose IL-2 administered every three days sustained an increased frequency of CD4$^+$ regulatory T cells and CD56^{br} NK cells in blood.

a, Schematic representation of the interval low-dose IL-2 (iLD-IL-2) dosing regimen used in this study. **b**, Gating strategy for the delineation of the five T and NK cell populations assessed by flow cytometry. Values shown represent the average frequency of the respective immune cell population at baseline (Day 0; ± standard error of mean, SEM) of the 18 DILfrequency participants. **c**, Variation (depicted as the %

change from baseline pre-treatment levels) in the frequency of the five assessed immune subsets in blood (denominator is total T cells for T cell subsets, CD 4^+ T cells for the CD 4^+ Treg subset and total $CD56^+$ NK cells for NK subsets). Data shown depict the average (± SEM) variation at each visit in the 18 DILfrequency participants treated with the 3-day interval dosing schedule. **d-e**, Absolute numbers of the assessed $CD4^+$ $CD127^{low}CD25^{hi}$ (Tregs) and $CD56^{br}$ NK cell (**d**), as well as the broader $CD4^+$and $CD8^+$ T and $CD56^+$ NK cell (**e**) subsets in blood. Data shown depict the average (± SEM) numbers at each visit in the 18 selected participants - treated with either 0.2 ($N = 4$), 0.32 ($N = 12$) or 0.47 ($N = 2$) × 10^6 IU/m^2 IL-2. Dotted lines indicate the average baseline pre-treatment numbers of each immune subset. Plots depicting the changes of the immune populations shown in **c-e** in each of the individual study participants are shown in ref. [19]. **f**, Overview of the experimental design employed in this study. Simultaneous quantification of mRNA (N = 565 probes) and surface-expressed proteins (N = 65 AbSeq antibodies) was performed at the single-cell level using the BD Rhapsody system and employing a cell-enrichment strategy. Equal proportions of flow-sorted cells subsets (30% $CD4^+$ Tregs; 25% $CD4^+$ Tconv and $CD8^+$ T; 12% $CD56^{br}$ NK and 8% $CD56^{dim}$ NK cells) from 13 selected DILfrequency participants treated with the 3-day dosing interval were profiled at three distinct time points: (i) prior to IL-2 treatment (Day 0), (ii) three days after the penultimate dose of IL-2 (Day 27), and (iii) one month after the last dose of IL-2 (Day 55). **g**, Uniform Manifold Approximation and Projection (UMAP) plot depicting the 15 clusters identified from the clustering of the 482,531 unstimulated cells profiled in this study. Clusters were manually annotated based on the expression of key differentially expressed mRNA and protein markers. Light grey cells correspond to $CD56^{br}$ NK cells without sorting gate information.

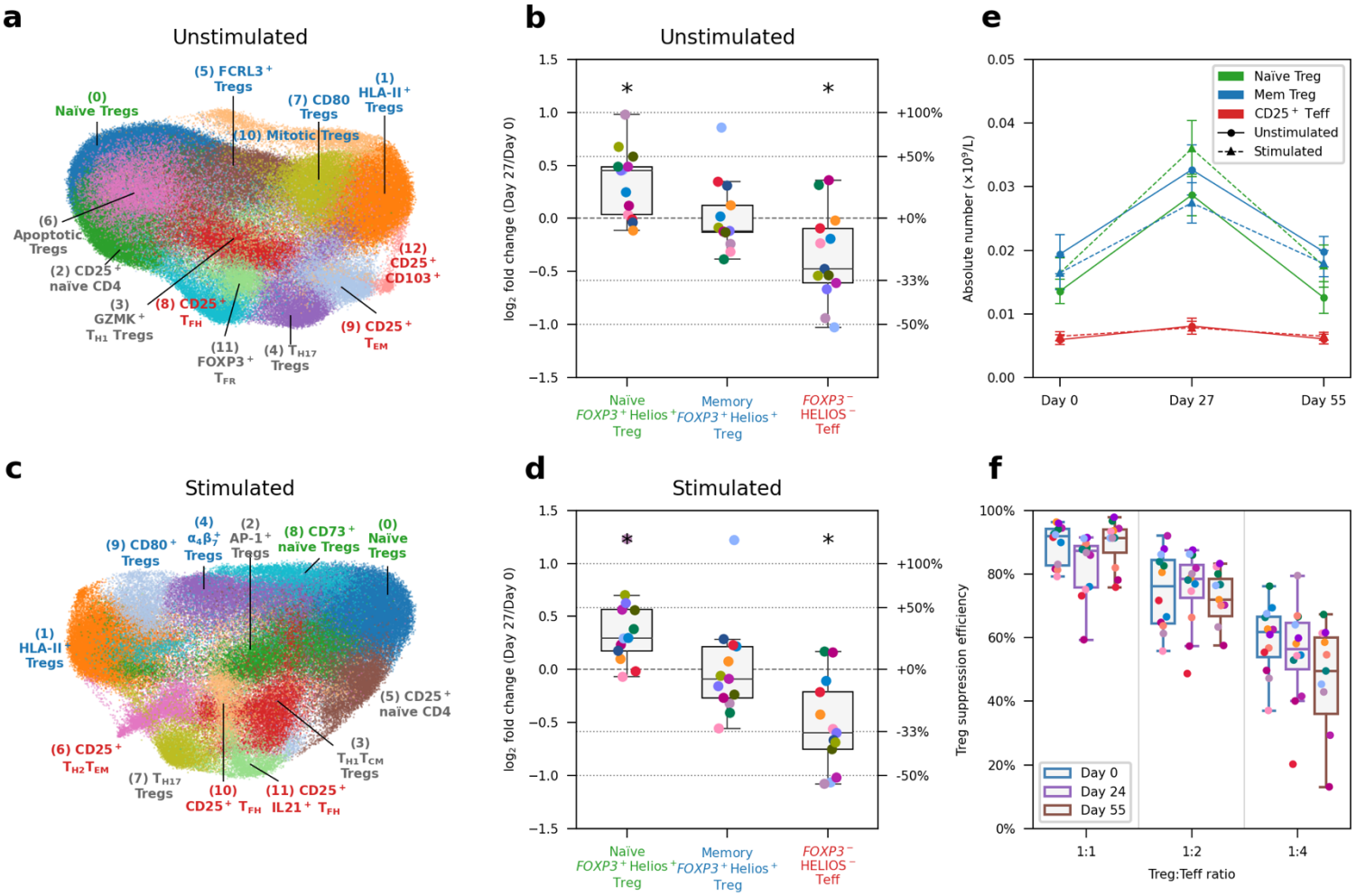

1137

1138 **Figure 2. Interval low-dose IL-2 immunotherapy selectively expands FOXP3$^+$HELIOS$^+$ Tregs.**

1139 **a**, UMAP plot depicting the 13 clusters identified from the clustering of the 149,202 unstimulated cells
1140 sorted from the CD127^{low}CD25^{hi} Treg gate profiled in this study. Clusters were manually annotated
1141 based on the expression of key differentially expressed mRNA and protein markers. Clusters
1142 corresponding to: (i) naïve Tregs (defined as CD45RA$^+$ FOXP3$^+$HELIOS$^+$); (ii) memory Tregs (defined
1143 as CD45RA$^-$ FOXP3$^+$HELIOS$^+$); or (iii) CD25$^+$ FOXP3$^-$HELIOS$^-$ Teffs (defined as CD45RA$^-$ FOXP3$^-$
1144 HELIOS$^-$) are annotated in green, blue and red, respectively. All other miscellaneous clusters not
1145 conforming to this definition are annotated in black. **b**, Relative frequency changes of naïve
1146 FOXP3$^+$HELIOS$^+$ Tregs, memory FOXP3$^+$HELIOS$^+$ Tregs, and CD25$^+$ FOXP3$^-$HELIOS$^-$ Teffs
1147 clusters on Day 27 compared to the baseline pre-treatment (Day 0) levels, for unstimulated cells. Relative
1148 frequency of a certain cluster was calculated as the number of cells in that cluster divided by the total

number of cells sorted from the Treg gate. **c**,**d** Corresponding UMAP plot (**c**) and relative frequency for the identified subsets (**d**) for the 115,153 *in vitro* stimulated $CD4^+$ T cells sorted from the $CD127^{low}CD25^{hi}$ Treg gate. **e**, Absolute cell numbers of naïve $FOXP3^+HELIOS^+$ Tregs, memory $FOXP3^+HELIOS^+$ Tregs, and $CD25^+$ $FOXP3^-HELIOS^-$ Teffs on Day 0, Day 27 and Day 35, for unstimulated (circles connected by solid lines) and stimulated (triangles connected by dashed lines) cells. Absolute cell numbers were calculated as the total absolute number of Tregs measured by FACS multiplied by the relative frequency of a certain cluster. **f**, Per-cell Treg suppression efficiency for each time point. Treg suppression efficiency was assessed *in vitro* by culturing $CD4^+CD25^{hi}CD127^{low}$ Tregs with autologous $CD4^+CD25^{-/low}CD127^+$ Teffs at various ratios (x axis) and represented as the decrease in Teff proliferation compared with the control condition (y axis). PBMCs from 12 participants sampled on Day 0, Day 24 and Day 55 were used for this assay. *FDR-adjusted $P < 0.05$; two-sided Wilcoxon signed-rank test comparing the relative frequency of the subsets between Day 27 and Day 0. In **b**, **d** and **f**, each dot represents cells from a single participant. Dots with the same colour represent the same participant.

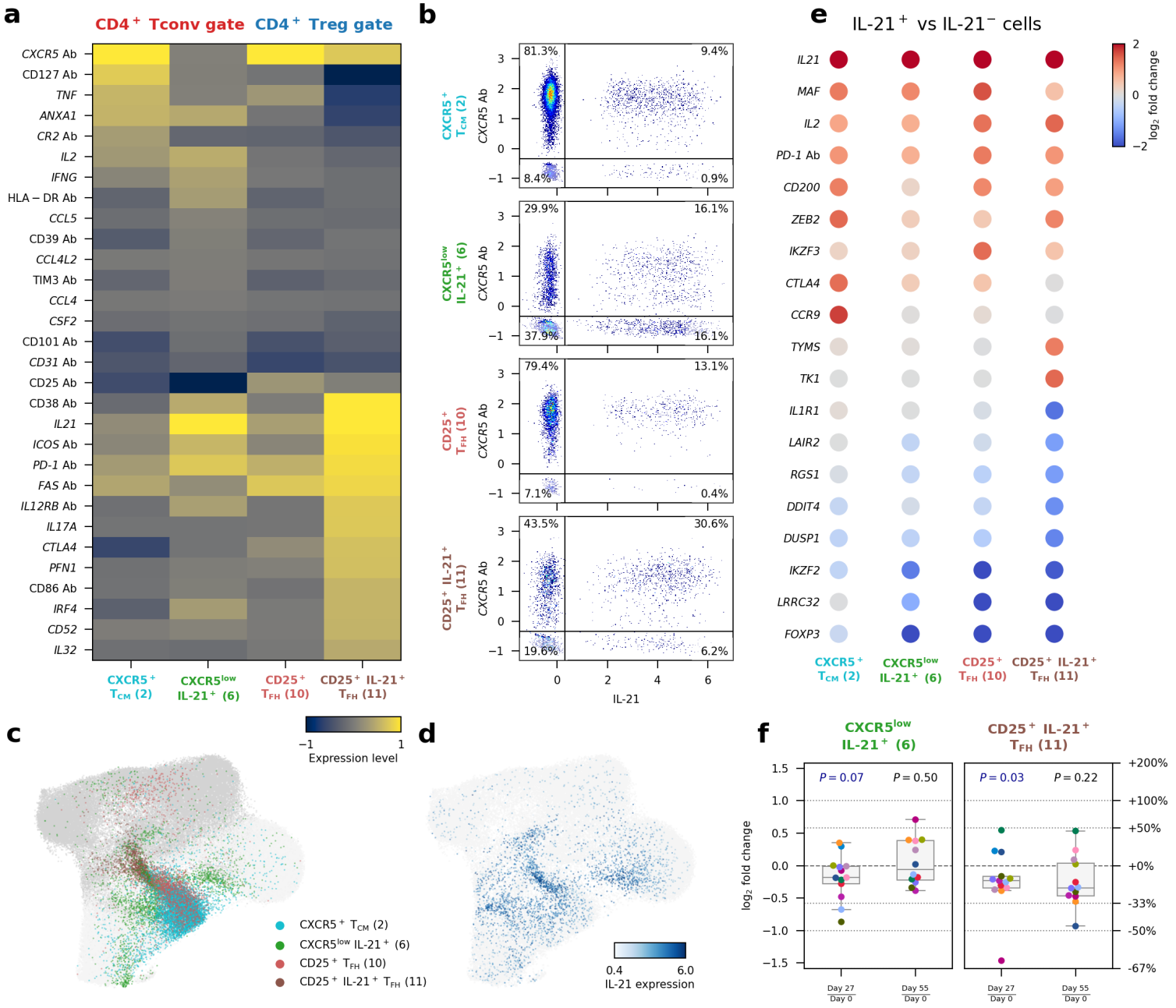

1165

1166 **Figure 3. Low-dose IL-2 treatment inhibits the differentiation of IL-21-producing CD4$^+$ T cells**

1167 **a,** Expression levels of 30 differentially expressed markers in the four assessed IL-21-producing CD4$^+$
1168 T cell subsets from *in vitro* stimulated CD4$^+$ T cells: CXCR5$^+$ T_{CM} and CXCR5^{low}IL-21$^+$ sorted from
1169 the CD25$^{-/low}$ Tconv gate; and CD25$^+$ T_{FH} and CD25$^+$IL-21$^+$ T_{FH} sorted from the CD127^{low}CD25^{hi} Treg
1170 gate. Expression levels are based on normalised and scaled single-cell expression data. Gene markers

were selected based on pairwise differential expression analysis among the four assessed clusters. **b**, Expression of CXCR5 (AbSeq) and *IL21* in the four assessed IL-21$^+$ CD4$^+$ T cell subsets from *in vitro* stimulated cells. **c**, UMAP plot depicting the clustering of *in vitro* stimulated CD4$^+$ T cells (N = 209,543 cells). Cells are coloured according to the respective IL-21$^+$ cluster assignment. Dark grey and light grey denote cells sorted from the CD127^{low}CD25^{hi} Treg gate and CD25$^{-/low}$ Tconv gate, respectively, that are not in IL-21$^+$ clusters (**c**); or by normalised and scaled IL-21 expression levels (**d**). **e**, Gene expression changes between IL-21$^+$ and IL-21$^-$ cells within each of the four assessed IL-21$^+$ CD4$^+$ T cell clusters. Fold change values were calculated from pseudo-bulk expression data. Genes with absolute $\log_2$ fold change values equal to or greater than 1.2 and FDR-adjusted *P* values less than 0.01 in at least one cluster were selected. **f**, Relative frequency changes of IL-21$^+$ cells within the two CD4$^+$ T cell subsets displaying higher expression levels of IL-21: the CXCR5^{low}IL-21$^+$ subset (left panel) and the CD25$^+$IL-21$^+$ T_{FH} subset (right panel), comparing Day 27 and Day 55 with Day 0, respectively. Each dot represents cells from a single participant. Dots with the same colour represent the same participant. *P* values were calculated by comparing the relative frequency values between the two time points using a two-sided Wilcoxon signed-rank test.

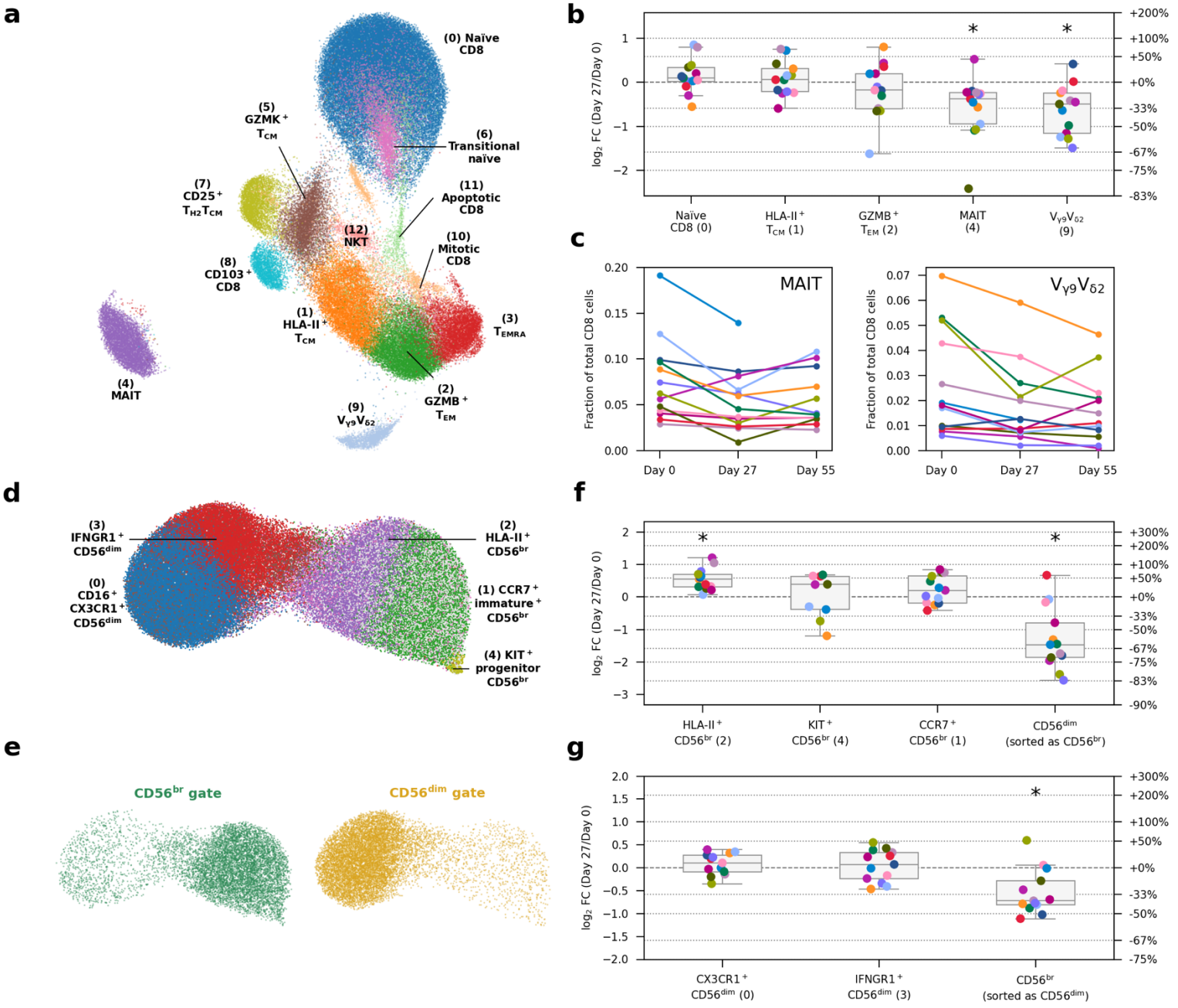

1188

1189 **Figure 4. IL-2 treatment reduces the frequency of innate-like CD8$^+$ MAIT and $V_{\gamma9}V_{\delta2}$ T cells in**
1190 **circulation and selectively expands the IL-2 sensitive CD56^{br} NK cell subset.**

1191 **a**, UMAP plot depicting the clustering of the 93,379 unstimulated CD8$^+$ T cells profiled in this study.
1192 Clusters were manually annotated based on the expression of key differentially expressed mRNA and
1193 protein markers. **b**, Relative frequency changes of five selected CD8$^+$ T cell clusters on Day 27 compared

to the baseline pre-treatment (Day 0) levels, for unstimulated cells. **c**, Relative frequency of the innate-like mucosal-associated invariant T cell (MAIT; left panel) and $V_{\gamma 9}V_{\delta 2}$ T cell (right panel) clusters on Day 0, Day 27, and Day 55. Each line represents cells from a participant. Lines with the same colour represent the same participant. **d**, UMAP plot depicting the clustering of the 118,625 unstimulated NK cells profiled in this study. Clusters were manually annotated based on the expression of key differentially expressed mRNA and protein markers. **e**, UMAP plot as in **d**, split and coloured by FACS sorting gates of origin. **f-g**, Relative frequency changes of five selected $CD56^{br}$ (**f**) or $CD56^{dim}$ (**g**) NK cell clusters on Day 27 compared to the baseline pre-treatment (Day 0) levels, for unstimulated cells. "$CD56^{dim}$ cells sorted as $CD56^{br}$" represents the fraction of cells sorted from the $CD56^{br}$ NK cell gate that are found in clusters that predominantly consists of $CD56^{dim}$ NK cells (ie. Clusters 0 and 3). Conversely, "$CD56^{br}$ cells sorted as $CD56^{dim}$" represents the fraction of cells sorted from the $CD56^{dim}$ NK cell gate that are found in clusters that predominantly consists of $CD56^{br}$ NK cells (ie. Clusters 1, 2 and 4). In **b**, **f**, and **g**, the relative frequency of a certain cluster is calculated as the number of cells in that cluster divided by the total number of cells sorted from the CD8 (**b**), $CD56^{br}$ (**f**) or $CD56^{dim}$ (**g**) NK cell gate. Each dot represents cells from a single participant. Dots with the same colour represent the same participant. Asterisks denote statistically significant differences (FDR-adjusted $P < 0.05$; two-sided Wilcoxon signed-rank test) in cell population frequencies between Day 27 and Day 0.

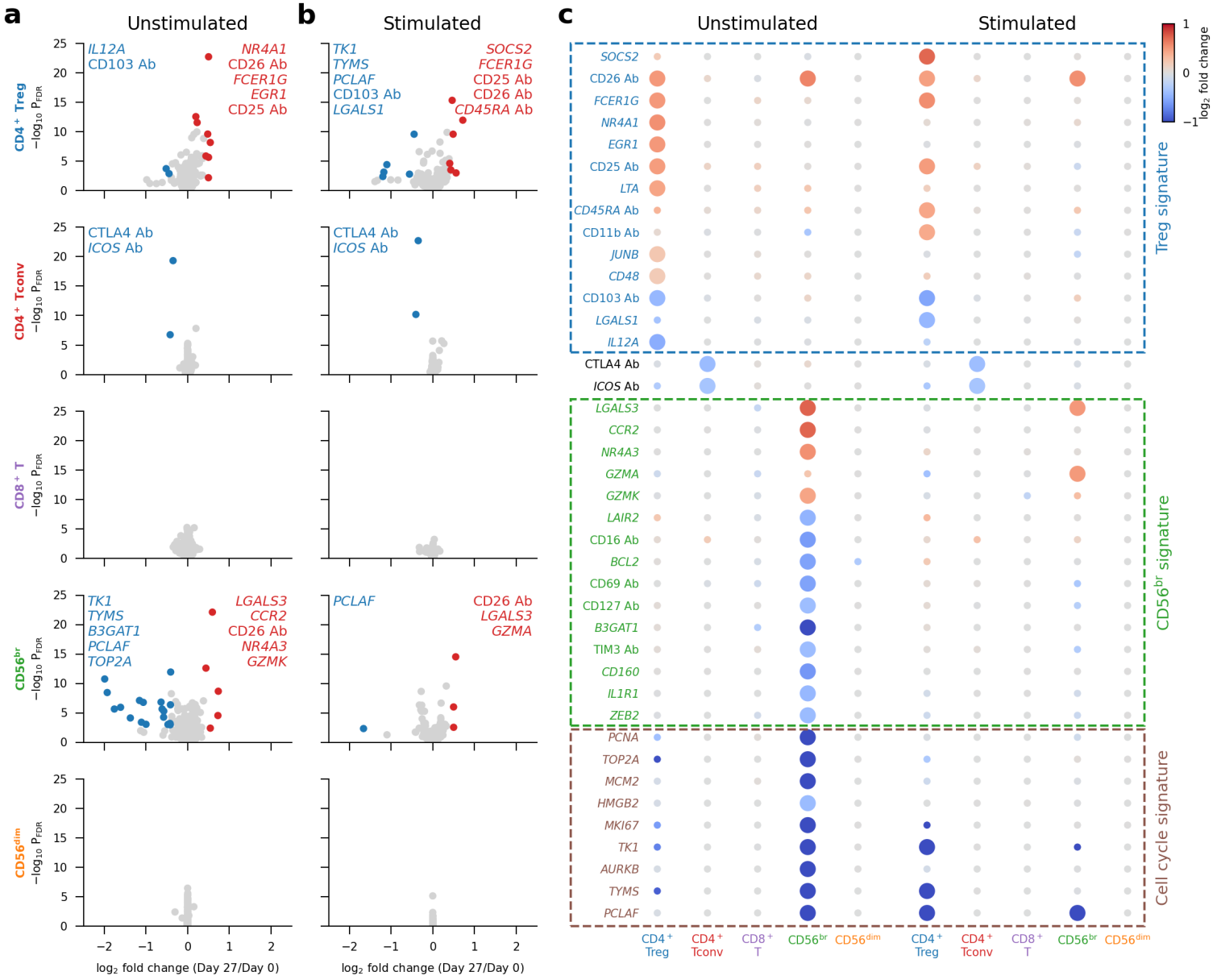

1213

1214 **Figure 5. IL-2 treatment selectively modulates gene expression of CD25^{hi} Tregs and CD56^{br} NK cells**
1215 **at Day 27.**

1216 **a-b**, Volcano plots depicting gene expression changes between Day 0 and Day 27 for the five assessed
1217 immune populations, for unstimulated (**a**) and stimulated (**b**) cells. Significantly differentially expressed
1218 genes are coloured in red (upregulated genes) or blue (downregulated genes). Names of the top five up- and
1219 downregulated genes as defined by fold change are labelled on each panel. **c**, Differential expression of
1220 Day 27 signature genes. Day 27 signature genes are defined as the 40 genes that are significantly

differentially expressed in at least one cell population comparing Day 27 with Day 0. Dot colours represent $\log_2$ fold change between Day 0 and Day 27. Larger dots represent genes that are significantly differentially expressed in a certain cell population. Manually annotated signature gene subsets are labelled with dashed boxes.

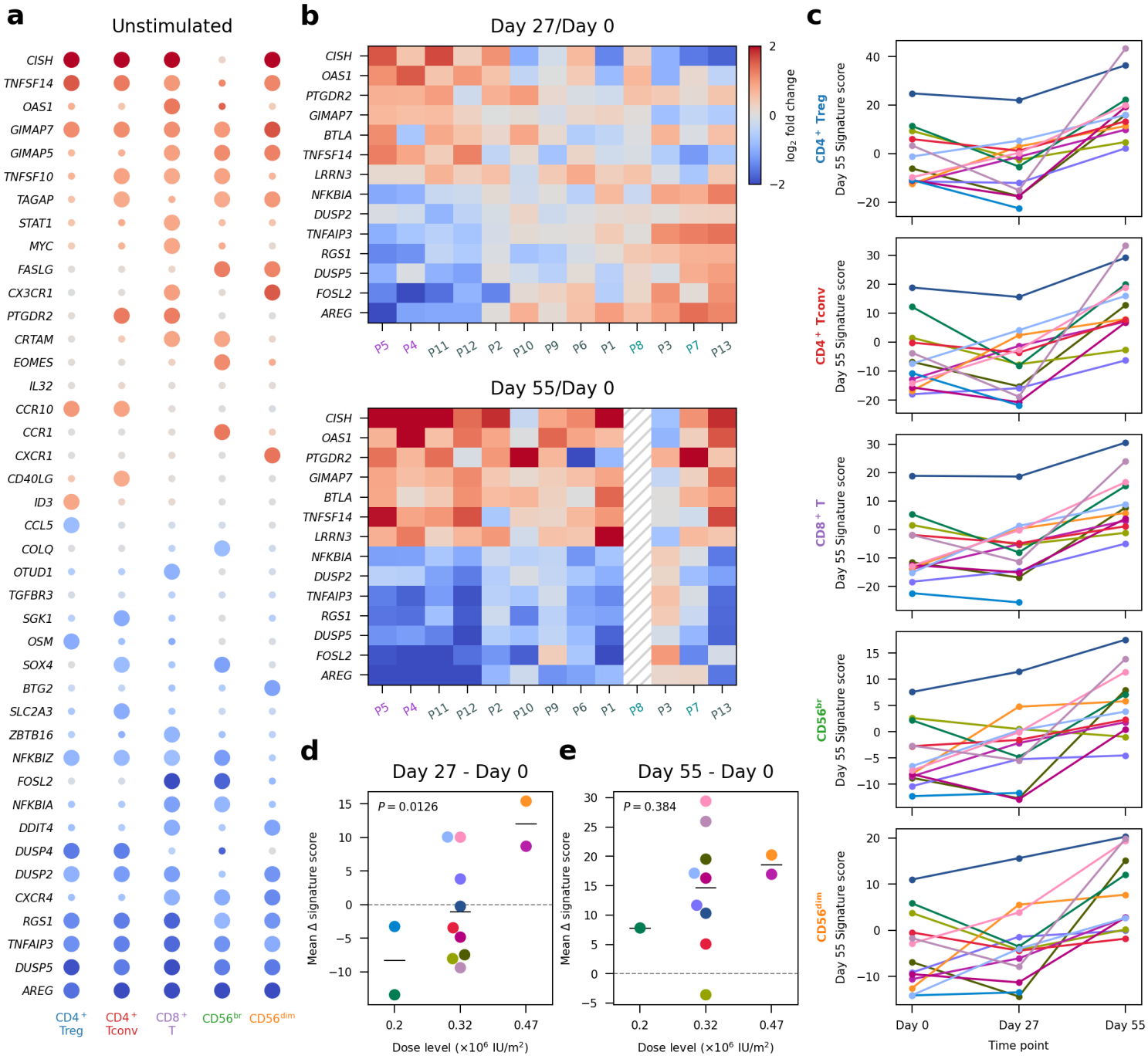

1226

1227 **Figure 6. Interval low-dose IL-2 immunotherapy induces a long-lasting anti-inflammatory gene**
1228 **expression signature**

1229 **a**, Differential expression of Day 55 signature genes. Day 55 signature genes were defined as the 41
1230 genes significantly differentially expressed in at least one cell population comparing Day 55 with Day

0. Dot colours represent $\log_2$ fold-change between Day 0 and Day 55. Larger dots represent significantly differentially expressed genes. **b**, Participant-specific differential expression in $CD8^+$ T cells comparing Day 27 (top panel) or Day 55 (bottom panel) with Day 0. Top 5 up- and downregulated genes as defined by Day 55/Day 0 fold-change in $CD8^+$ T cells. Participant labels are coloured by their respective IL-2 dose ($\times 10^6$ IU/m^2): 0.2 (cyan), 0.32 (gray), 0.47 (purple). **c**, Day 55 signature scores by participant for each time point and cell type. Each participant is represented by a different colour. *P* values were calculated using a two-tailed paired t test comparing Day 27 or Day 55 with Day 0, respectively. **d-e**, Variation in the mean expression scores of Day 55 signature genes across the five major cell types (mean Δ signature score) between Day 27 and Day 0 (**d**) and between Day 55 and Day 0 (**e**) for each participant. Participants were stratified by IL-2 dose. *P* values were calculated using linear regression. In d**-e**, average values of the Day 55 signature in all five cell types are shown for each participant.

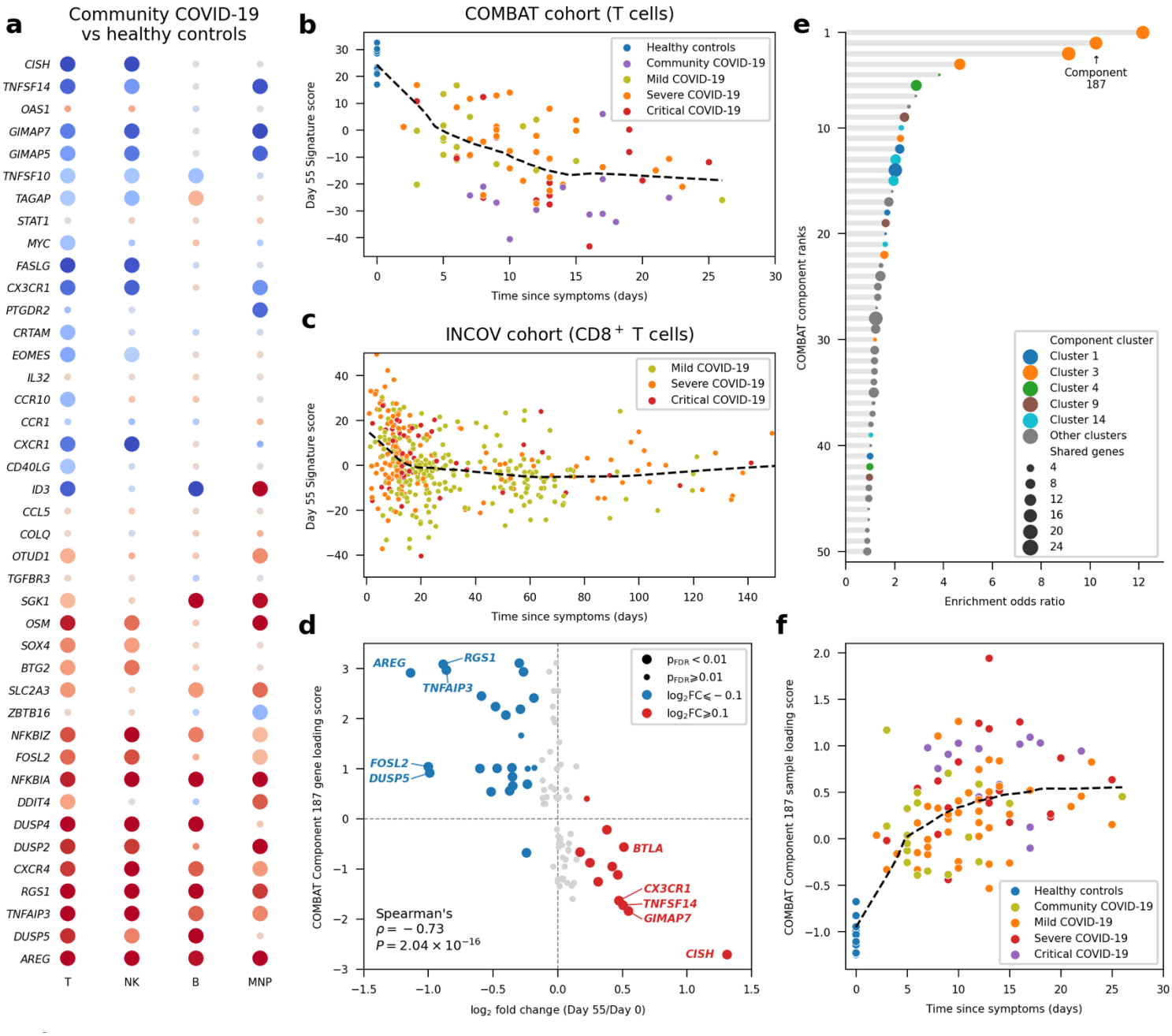

1244

1245 **Figure 7. The IL-2-induced Day 55 anti-inflammatory gene expression signature is reversed in**
1246 **COVID-19 patients**

1247 **a,** Differential expression of the 41 identified Day 55 signature genes in COVID-19 patients. Dot
1248 colours represent $\log_2$ fold-change between healthy controls and community COVID-19 patients
1249 from the COMBAT study[42]. Larger dots represent significantly differentially expressed genes in a

certain cell population. **b-c** Day 55 gene signature scores plotted against the time since COVID-19 symptoms in the COMBAT (**b**) and INCOV[43] (**c**) cohorts. The Day 55 gene signature score was based on expression levels of the 41 identified Day 55 signature genes. Each dot represents a pseudo-bulk sample from a certain participant and time point. Up to three longitudinal samples may originate from the same participant. COVID-19 patients were stratified according to their maximum disease severity. Dashed black lines represent smooth curves fitted by locally weighted scatterplot smoothing (LOWESS). **d**, Correlation between the differential expression of the Day 55 signature genes and Component 187 from the COMBAT study. Of the 1,419 genes included in Component 187, a gene expression signature induced by COVID-19, 77 are also present in the target transcriptional panel used in this study. The effects of IL-2 immunotherapy and COVID-19 infection on the induction of these genes are compared by correlating Component loading score (y axis) with log2 fold change (Day 55/Day 0) in the CD8 population after IL-2 treatment (x axis). The positive and negative values in Component 187 loading scores represent the up- and downregulation of the corresponding gene, respectively, after COVID-19 infection. Larger dots represent genes with FDR-adjusted P values < 0.01, comparing Day 55 and Day 0 expression levels. **e**, Enrichment of Day 55 signature genes in each gene expression component reported in the COMBAT study. Each dot represents a disease-associated gene expression component in the COMBAT study. Dot sizes represent the number of shared genes between a certain component and the 41 Day 55 signature genes. Only top 50 components ranked by their odds ratios of enrichment (x axis) are shown. Colours represent cluster membership as reported in the COMBAT study. Components in the same cluster are associated with diseases in a similar way. Cluster 3 is associated with all severity groups of COVID-19. **f**, Component 187 sample loading scores plotted against time since symptoms for COVID-19 patients. Each dot represents a patient. Patients are stratified by their maximum COVID-19 severity.

Supplementary Figures

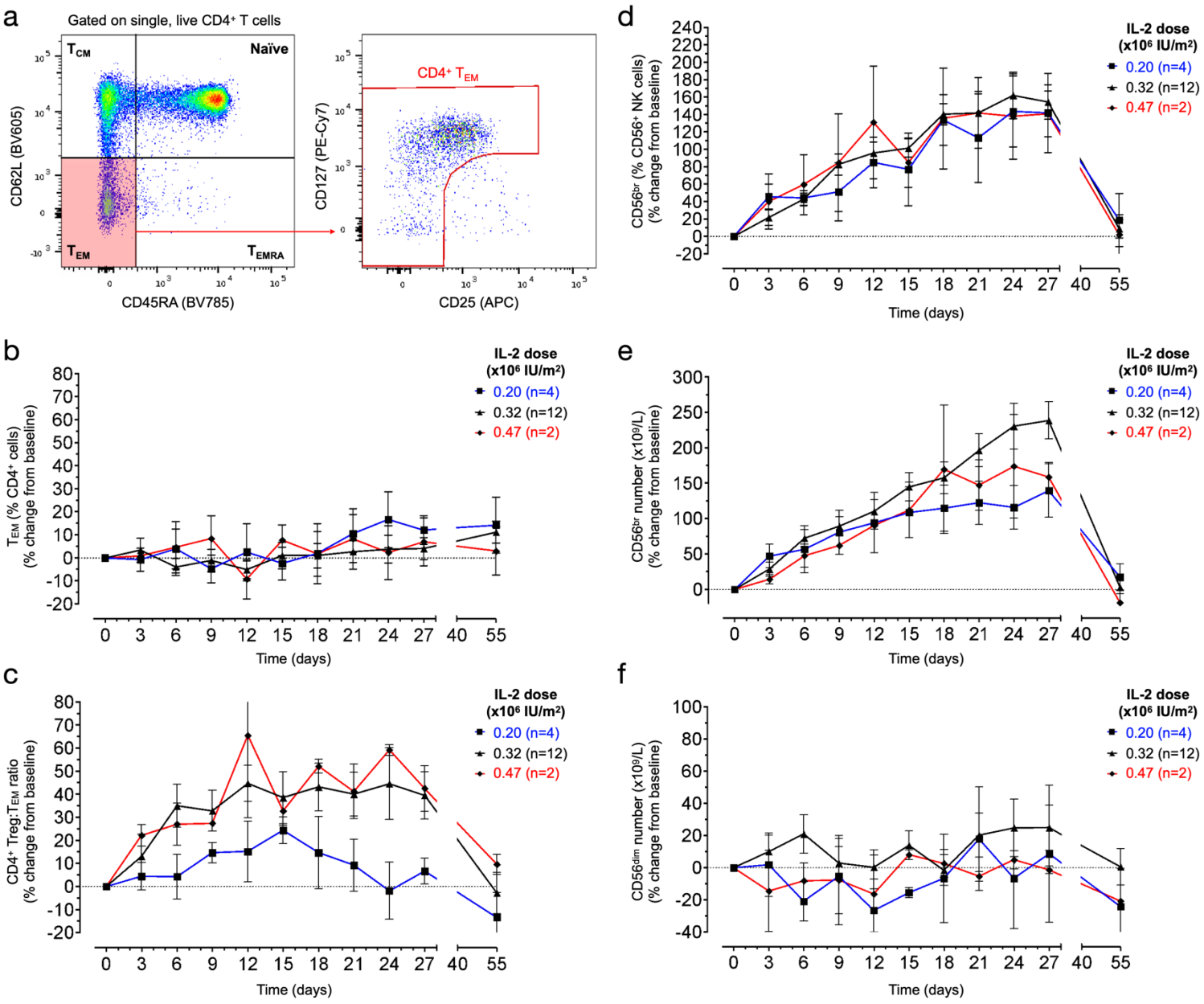

Supplementary Figure 1. Flow cytometric characterisation of the effector memory CD4$^+$ T and CD56$^+$ NK cell populations.

a, Gating strategy for the delineation of CD4$^+$ effector memory T cells (T_{EM}). **b-c**, Variation (depicted as the % change from pre-treatment baseline levels) in the frequency of CD4$^+$ T_{EM} (**b**), or the ratio between CD4$^+$ Tregs and T_{EM} cells (**c**) during the course of the study. Baseline levels (mean +/- SEM): CD4$^+$ T_{EM}

= 10.4% +/- 1.39; $CD4^+$ Treg:T_{EM} ratio = 0.76 +/- 0.07. **d-f,** Variation (depicted as the % change from pre-treatment baseline levels) in the relative frequency of $CD56^{br}$ NK cells within the total $CD3^-CD56^+$ NK cell gate (**d**), and in the absolute number of $CD56^{br}$ (**e**) and $CD56^{dim}$ (**f**) NK cells in blood during the course of the study. Baseline levels (mean +/- SEM): $CD56^{br}$ = 6.2% +/- 0.55; $CD56^{br}$ Number ($x10^9$/L) = 0.011 +/- 0.001; $CD56^{dim}$ Number ($x10^9$/L) = 0.18 +/- 0.02. Frequencies of the assessed immune subsets were determined by flow cytometry in the 18 DILfrequency participants treated with the 3-day interval dosing schedule. Data shown depict the average (± SEM) variation of the assessed immune subsets at each visit and were stratified according to the IL-2 dose.

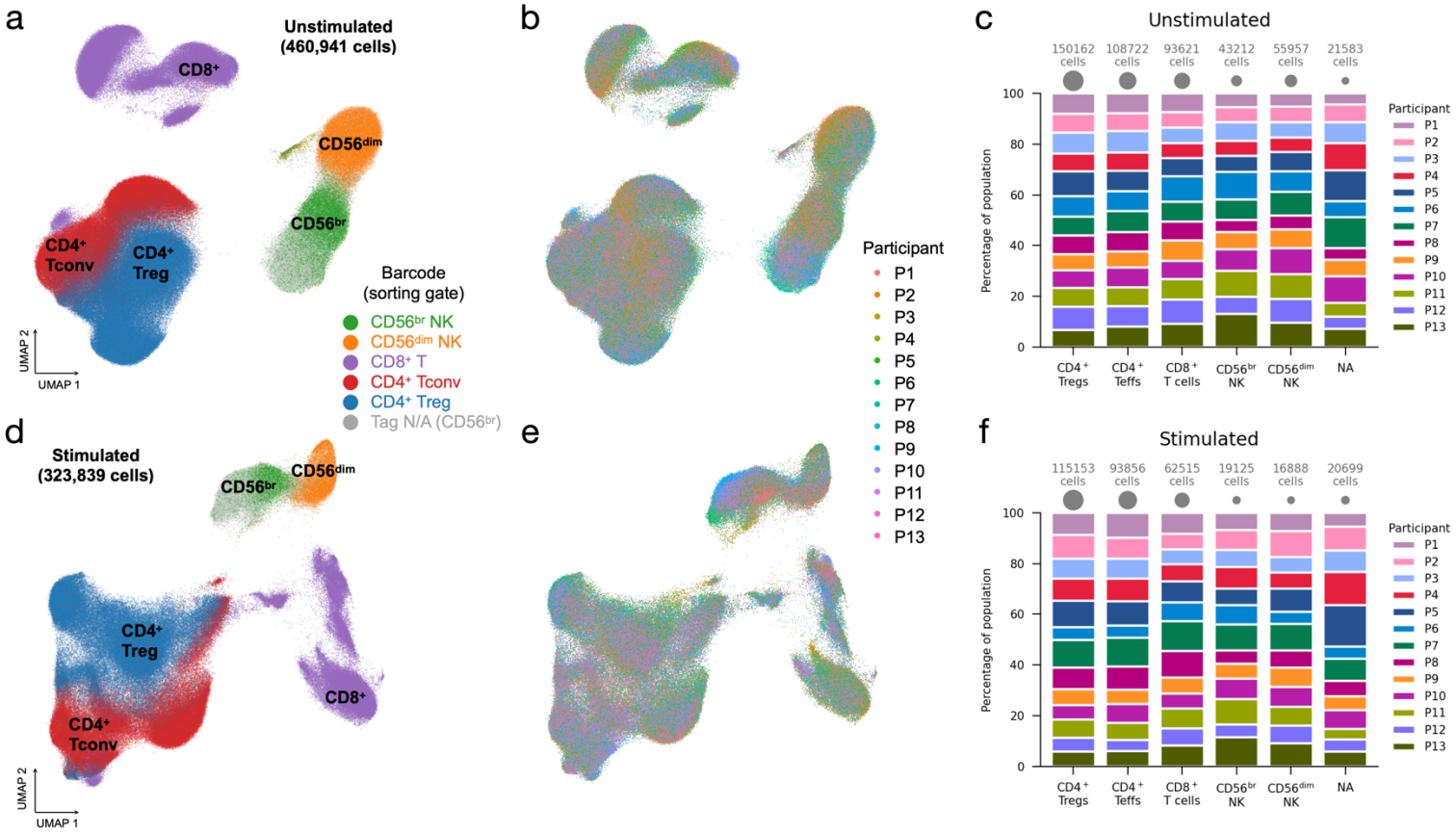

Supplementary Figure 2. Integration of the single-cell multiomics data.

a-b, Uniform Manifold Approximation and Projection (UMAP) plot depicting the clustering of the 460,941 unstimulated cells profiled in this study. Cells were coloured according to the corresponding oligo-conjugated barcode indicative of the respective FACS sorting gate (**a**), or according to the participant of origin (**b**). Untagged cells in **b** (labelled as 'Tag N/A') correspond to CD56^{br} NK cells, where we observed a suboptimal sample tagging efficiency, resulting in a significant fraction (37.2% in unstimulated cells) of CD56^{br} NK cells with missing sample barcode information. **c**, Relative proportion of cells from each individual participant in each of the flow-sorted unstimulated immune cell populations. Areas of grey circles represent total cell numbers in each immune cell population. **d-e**, UMAP plots depicting the clustering of the 323,839 cells profiled in this study following a short (90 min) *in vitro* stimulation with PMA + ionomycin. Cells were coloured according to the corresponding oligo-conjugated barcode indicative of the respective FACS sorting gate (**d**), or to the donor information (**e**). Untagged cells in panel a (labelled as 'Tag N/A') correspond to CD56^{br} NK cells, where we observed a suboptimal sample

tagging efficiency resulting in a significant fraction (44.3% in the *in vitro* stimulated cells) of $CD56^{br}$ NK cells with missing sample barcode information. **f**, Relative proportion of cells from each individual participant in each of the flow-sorted stimulated immune cell populations. Areas of grey circles represent total cell numbers in each immune cell population.

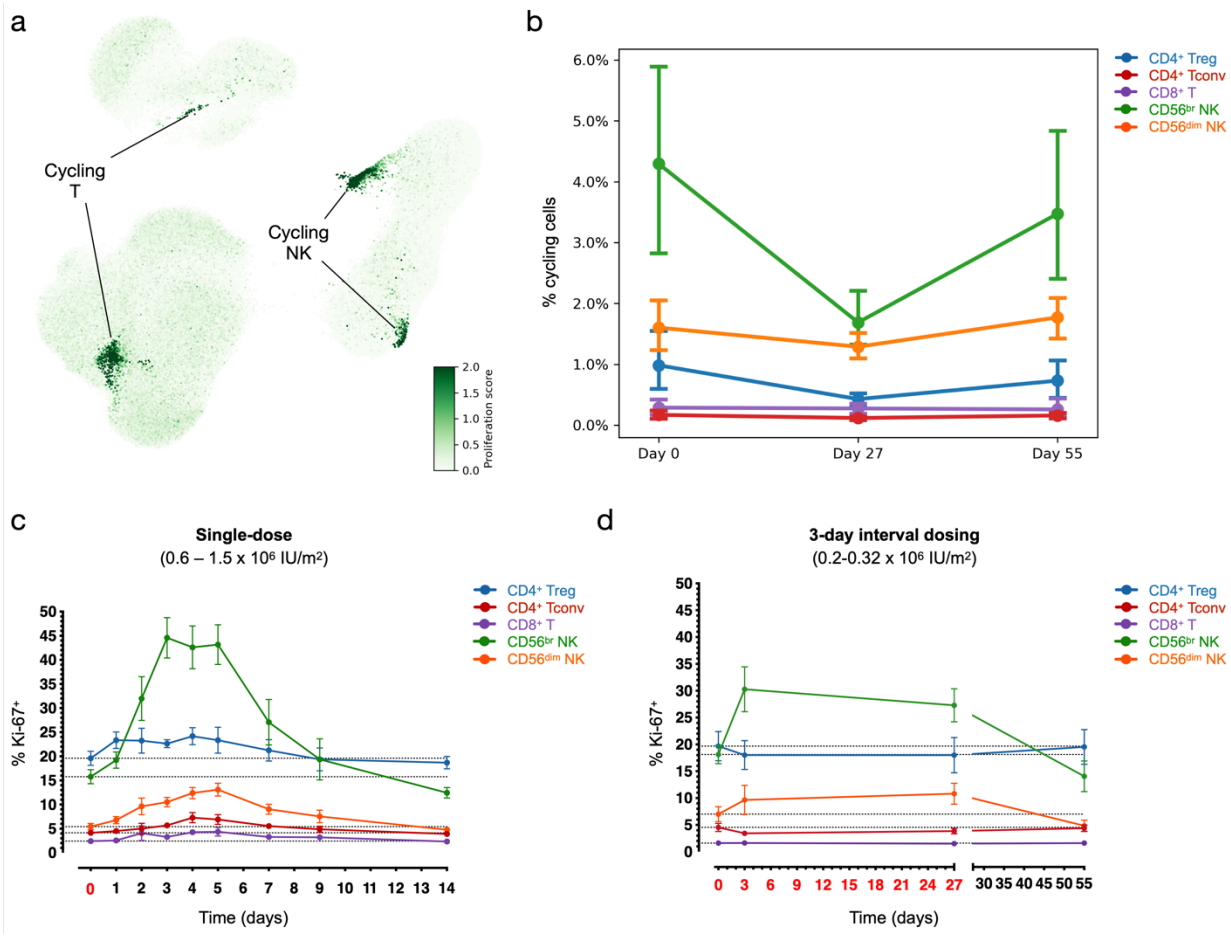

Supplementary Figure 3. Identification of proliferating cells.

a, UMAP plot depicting the expression of the cell-cycle signature score in each unstimulated single-cell, calculated by summarising the expression levels of 11 pre-selected genes related to cell cycle. **b**, Frequency of proliferating cells in each immune subset identified by the single-cell multiomics analysis. Proliferating cells were defined as the proportion of cells in the identified cycling clusters from each of the 5 sorted immune populations at Days 0, 27 and 55. **c-d**, Frequency of Ki-67^{+} cells within each of the 5 assessed immune populations in T1D patients treated with a single (DILT1D; **c**) or with the 3-day interval dosing schedule (DILfrequency; **d**). Ki-67 protein levels were assessed by intracellular flow cytometry in 6 patients from the DILT1D (treated with doses ranging from 0.6-1.5 x 10^6 IU/m^2) and five patients from the DILfrequency (treated with interval doses ranging from 0.2-0.32 x 10^6 IU/m^2). IL-2 dosing days are depicted in red in the x axis.

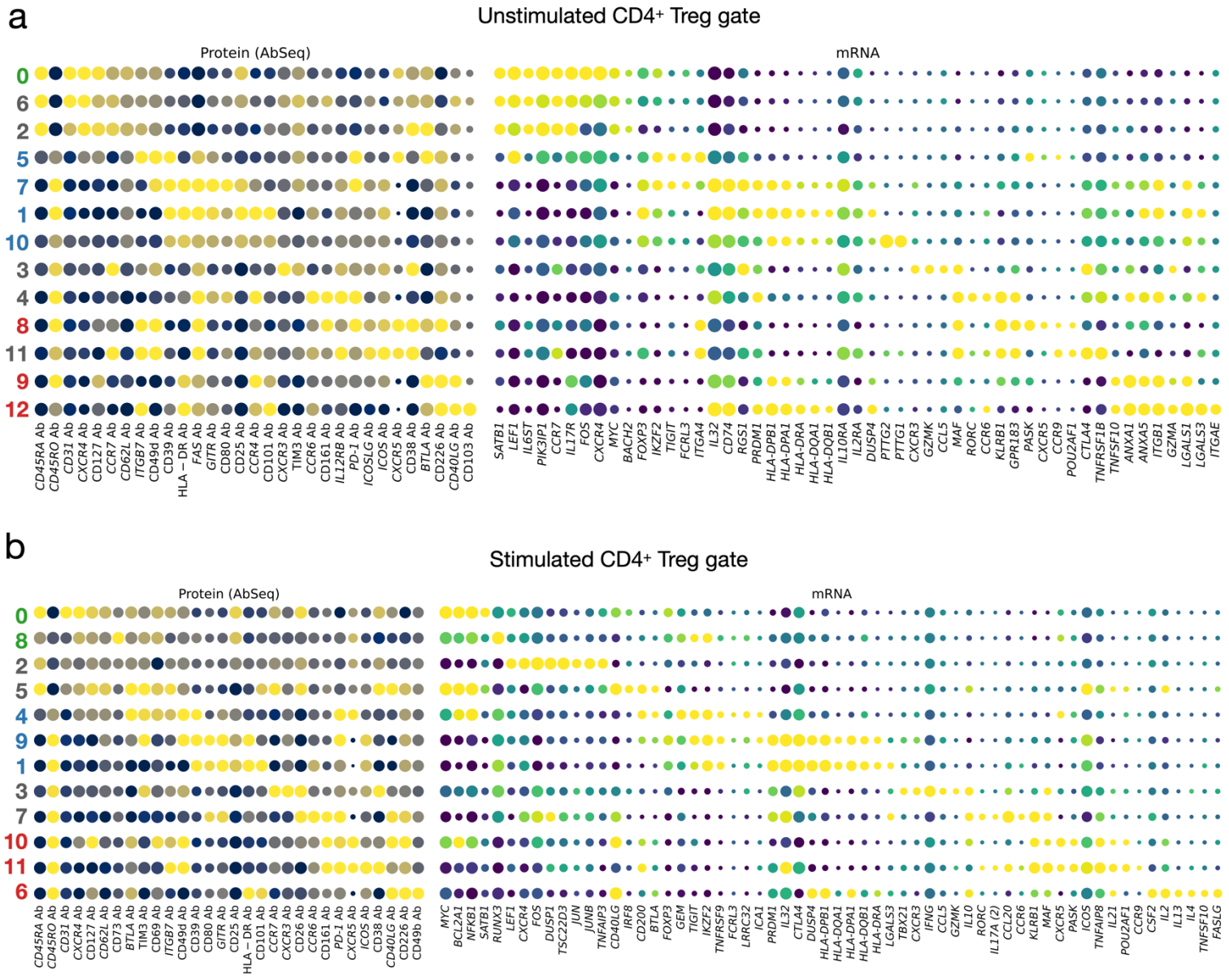

Supplementary Figure 4. Functional annotation of the CD4$^+$ CD127^{low}CD25^{hi} T cell subsets.

a-b, Expression levels of selected differentially expressed markers delineating the functional subsets in the unstimulated (**a**) and *in vitro* stimulated (**b**) CD4$^+$ T cells sorted from the CD127^{low}CD25^{hi} Treg gate. The size of the dots represents the frequency of the marker in the respective cluster and the colour brightness represents the relative expression level. Protein markers (AbSeq) are shown on the left section of the plots and mRNA markers on the right section. Clusters corresponding to: (i) naïve Tregs (defined as CD45RA$^+$ FOXP3$^+$HELIOS$^+$); (ii) memory Tregs (defined as CD45RA$^-$ FOXP3$^+$HELIOS$^+$); or (iii)

1333 $CD25^{+}$ $FOXP3^{-}HELIOS^{-}$Teffs (defined as $CD45RA^{-}$ $FOXP3^{-}HELIOS^{-}$) are annotated in green, blue
1334 and red, respectively. All other miscellaneous clusters not conforming to this definition are annotated in
1335 black.

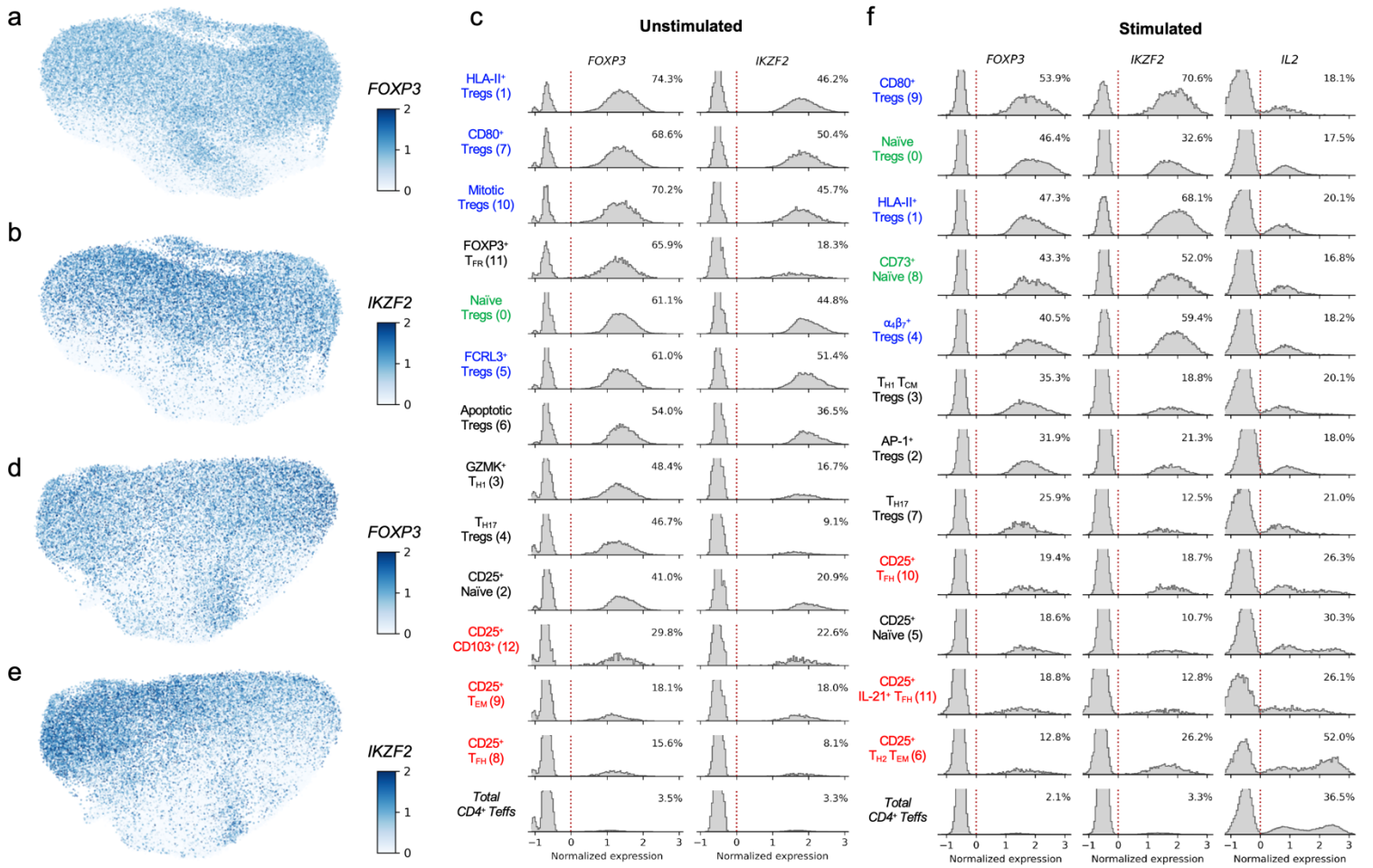

Supplementary Figure 5. Expression of *FOXP3*, *IKZF2* (HELIOS) and *IL2* differentiate functional CD4$^+$ Treg and CD4$^+$ Tconv subsets.

a-b, UMAP plots depicting the expression of the canonical Treg transcription factors *FOXP3* (**a**) and *IKZF2* (encoding HELIOS; **b**) in the unstimulated cells sorted from the CD4$^+$ CD127^{low}CD25^{hi} Treg gate. **c**, Distribution of expression levels of *FOXP3* and *IKZF2* in the identified unstimulated CD127^{low}CD25^{hi} CD4$^+$ T cell clusters. **d-e**, UMAP plots depicting the expression of the canonical Treg transcription factors *FOXP3* (**d**) and *IKZF2* (**e**) in the *in vitro* stimulated cells. **f**, Histograms depicting the expression of *FOXP3*, *IKZF2* and *IL2* in the identified *in vitro* stimulated clusters. Clusters corresponding to: (i) naïve Tregs (defined as CD45RA$^+$ FOXP3$^+$HELIOS$^+$); (ii) memory Tregs (defined as CD45RA$^-$ FOXP3$^+$HELIOS$^+$); or (iii) CD25$^+$ FOXP3$^-$HELIOS$^-$Teffs (defined as CD45RA$^-$ FOXP3$^-$ HELIOS$^-$) are annotated in green, blue and red, respectively. All other miscellaneous clusters not conforming to this definition are annotated in black.

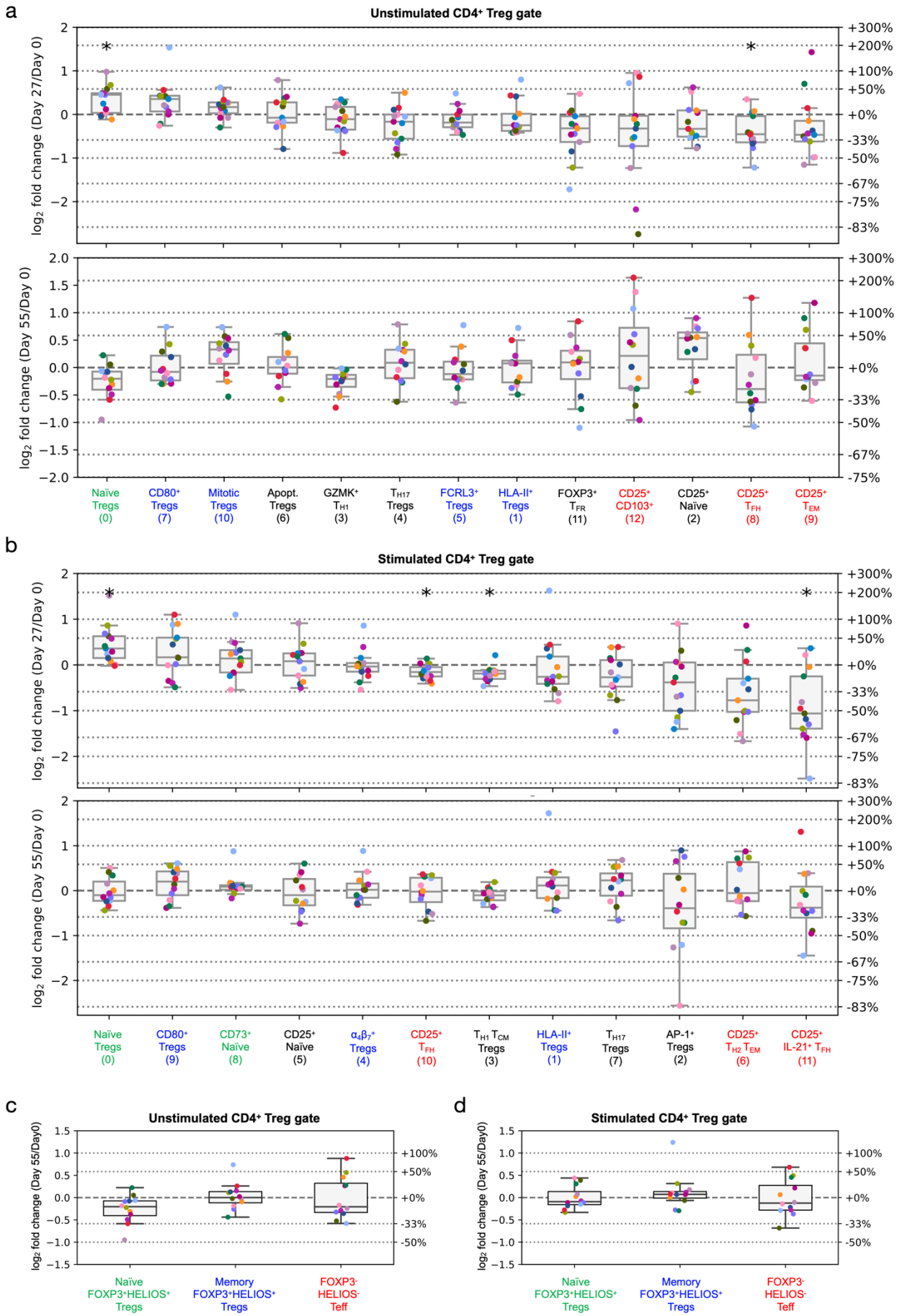

Supplementary Figure 6. Differential abundance analysis reveals a transient increased frequency of FOXP3^{+}HELIOS^{+} Tregs following ld-IL2 treatment.

a-b, Relative frequency changes of all the identified unstimulated (**a**) or *in vitro* stimulated (**b**) CD127^{low}CD25^{hi} T cell clusters between Day 0 and Day 27 (top panels) or Day 55 (bottom panels). Clusters corresponding to: (i) naïve Tregs (defined as CD45RA^{+} FOXP3^{+}HELIOS^{+}), (ii) memory Tregs (defined as CD45RA^{-} FOXP3^{+}HELIOS^{+}), and (iii) CD25^{+} FOXP3^{-}HELIOS^{-}Teffs (defined as CD45RA^{-} FOXP3^{-}HELIOS^{-}) are annotated in green, blue and red, respectively. All other miscellaneous clusters not conforming to this definition are annotated in black. Asterisks denote statistically significant differences (two-sided Wilcoxon signed-rank test) in cell population frequencies between the two time points. **c-d**, Relative frequency changes of unstimulated (**c**) or *in vitro* stimulated (**d**) naïve FOXP3^{+}HELIOS^{+} Treg, memory FOXP3^{+}HELIOS^{+} Treg, and CD25^{+} FOXP3^{-}HELIOS^{-}Teff clusters in blood between Day 0 and Day 55. In **a-d**, each dot represents cells from a single participant. Dots with the same colour represent the same participant.

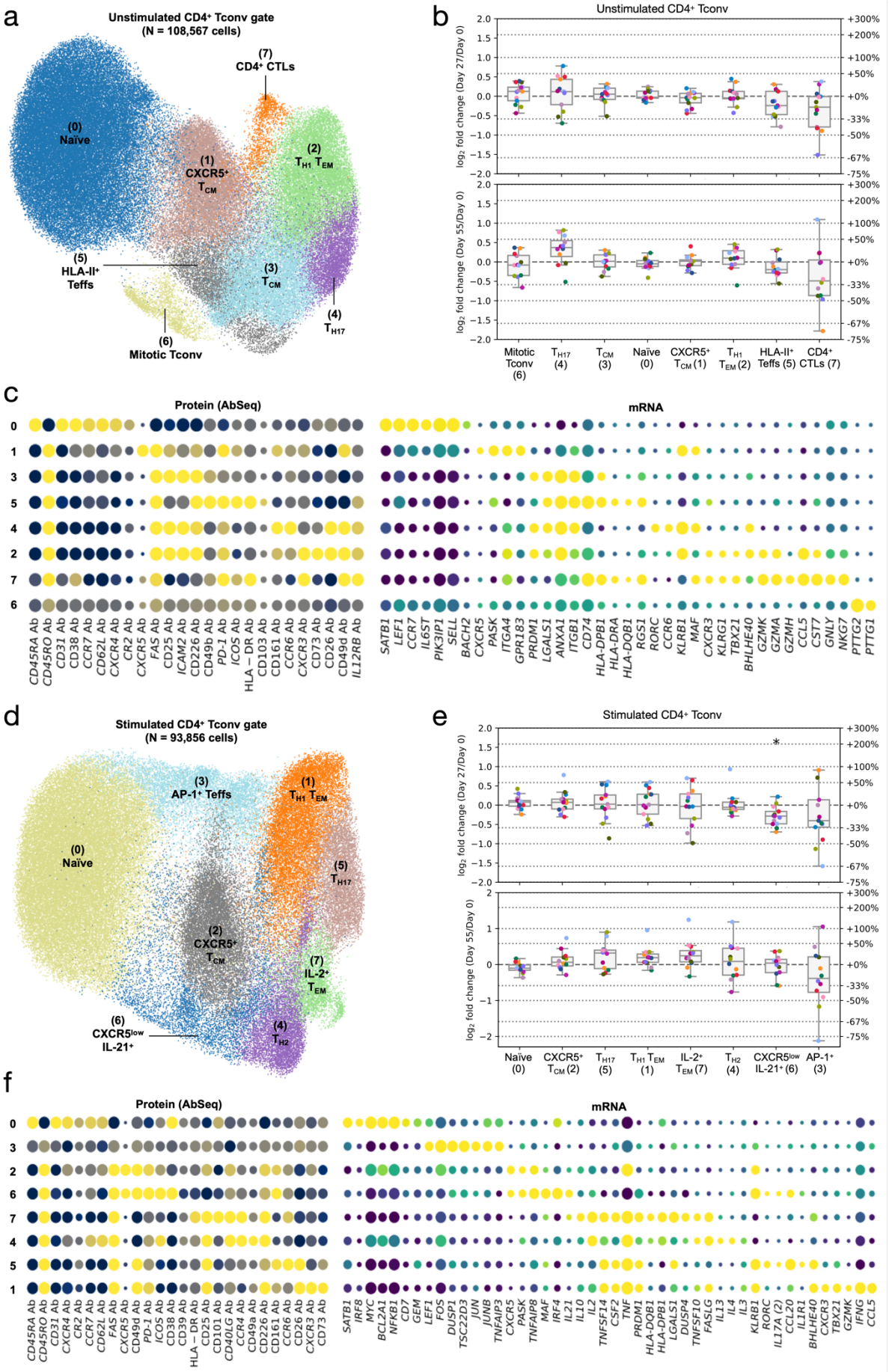

Supplementary Figure 7. Analysis of circulating CD4$^+$ CD25$^{-/low}$ conventional T cells

a, UMAP plot depicting the clustering of the 108,722 unstimulated CD4$^+$ T cells sorted from the CD25$^{-/low}$ Tconv gate profiled in this study. Clusters were manually annotated based on the expression of key differentially expressed mRNA and protein markers. **b**, Expression levels of selected differentially expressed markers delineating the functional subsets in the unstimulated CD4$^+$ T cells sorted from the CD25$^{-/low}$ Tconv gate. The size of the dots represents the frequency of the marker in the respective cluster and the colour brightness represents the relative expression level. Protein markers (AbSeq) are shown on the left section of the plots and mRNA markers on the right section. **c,** Relative frequency changes of all identified unstimulated CD4$^+$ CD25$^{-/low}$ Tconv clusters in blood at Day 27 (top panel) or Day 55 (bottom panel) compared to the baseline pre-treatment (Day 0) levels. **d-f**, Plots corresponding to **a-c**, for the 93,856 *in vitro* stimulated CD4$^+$ T cells sorted from the CD25$^{-/low}$ Tconv gate.

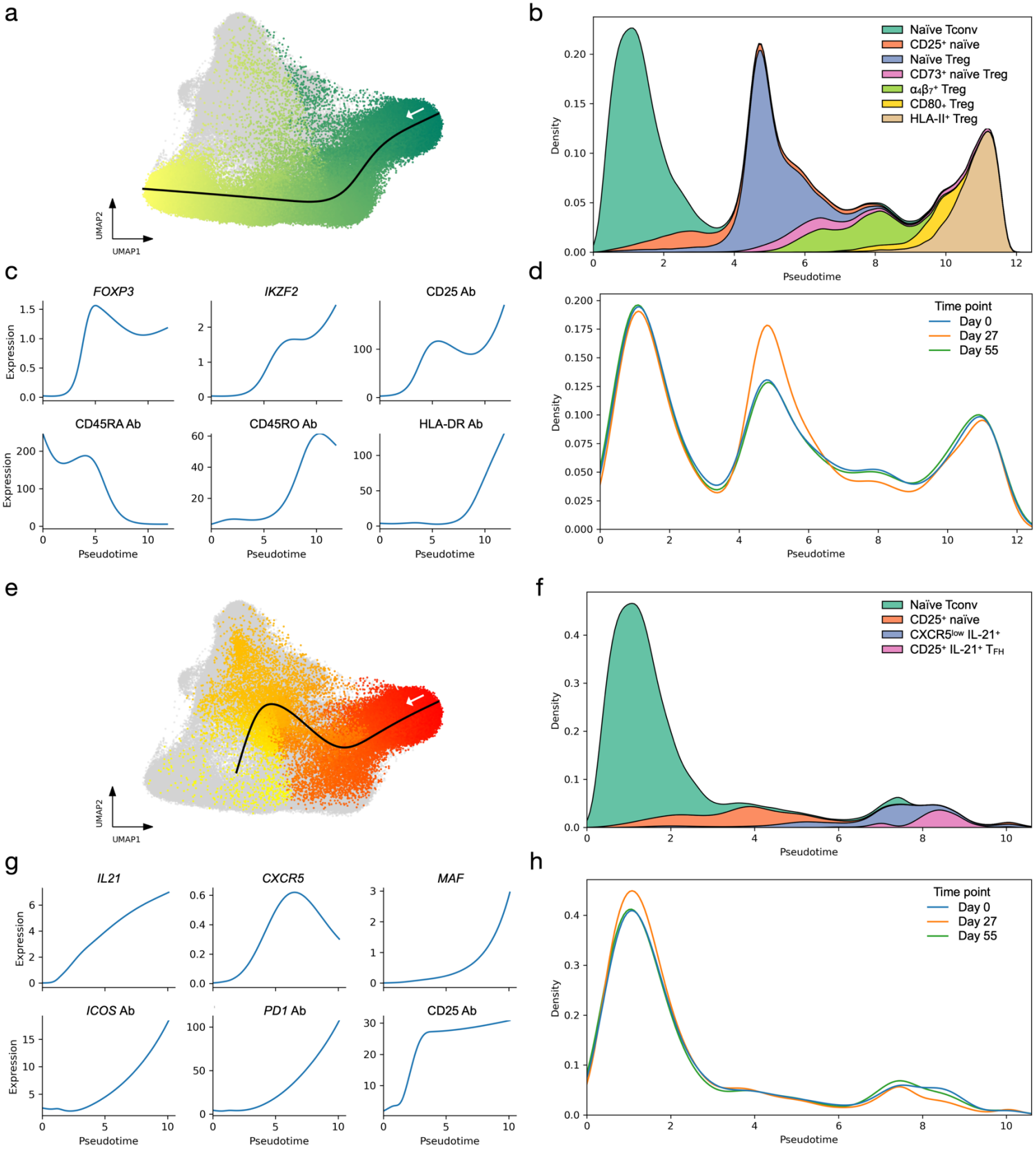

1379

Supplementary Figure 8. Pseudo-time analysis reveals trajectories of Treg and T_{FH} differentiation in *in vitro* stimulated $CD4^+$ T cells.

a, UMAP plot depicting the Treg differentiation trajectory identified by Slingshot pseudo-time analysis. **b**, Pseudo-time distribution of cells associated with the Treg trajectory, stratified by cluster labels. **c**, Fitted expression curves of selected canonical Treg genes by pseudo-time. **d**, Pseudo-time distribution of cells associated with the Treg trajectory, stratified by time points. **e**, UMAP plot depicting the T_{FH} differentiation trajectory identified by Slingshot pseudo-time analysis. **f**, Pseudo-time distribution of cells associated with the T_{FH} trajectory, stratified by cluster labels. **g**, Fitted expression curves of selected canonical T_{FH} genes by pseudo-time. **h**, Pseudo-time distribution of cells associated with the T_{FH} trajectory, stratified by time points. Data from **a-h** were generated from in vitro stimulated $CD4^+$ T cells.

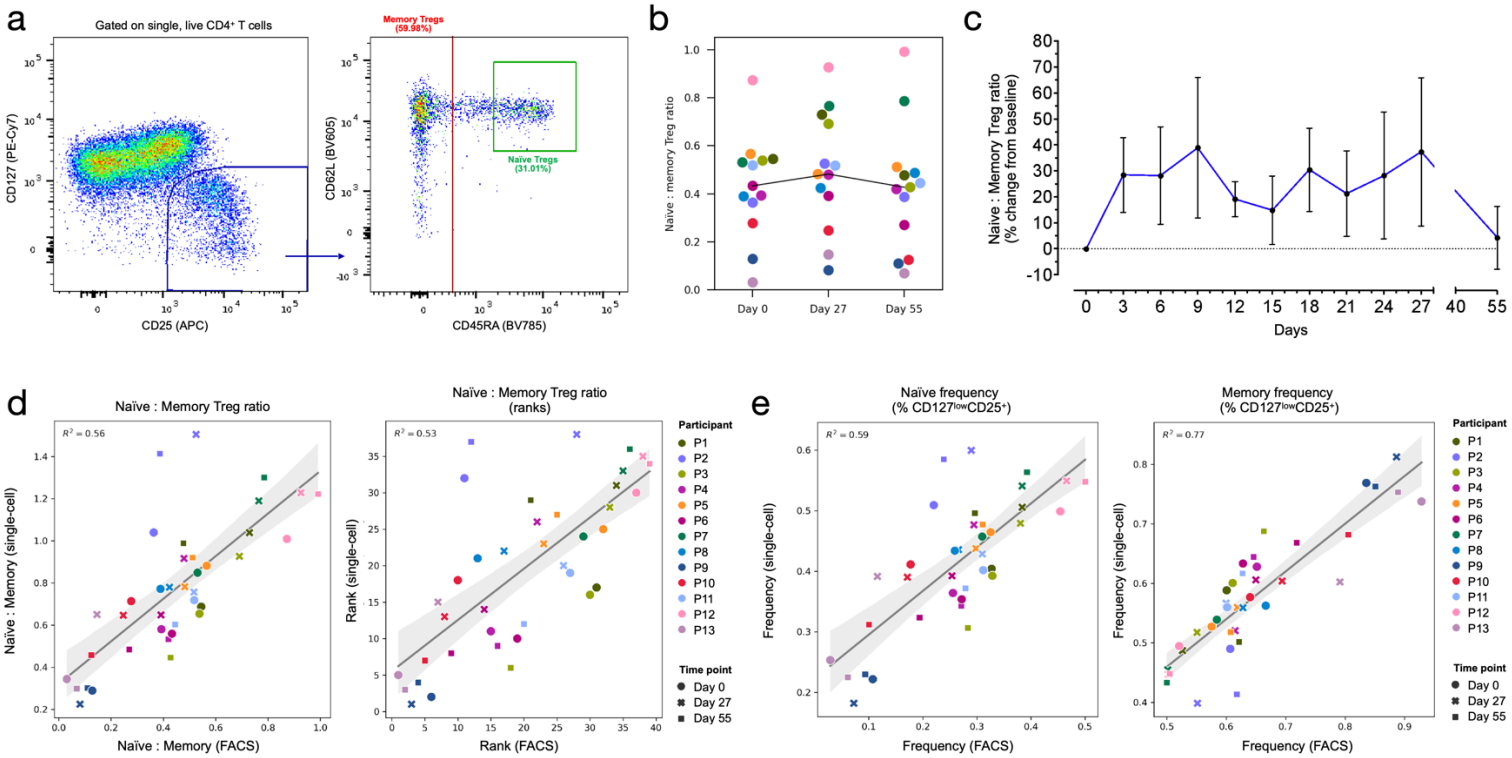

1393

1394 **Supplementary Figure 9. Replication of the ratio of naïve:memory Tregs by FACS**

1395 **a**, Gating strategy for the delineation of the naïve (CD45RA^{+}) and memory (CD45RA^{-}) compartment
1396 by flow cytometry within cells sorted from the CD4^{+} CD127^{low}CD25^{hi} Treg gate. **b**, Ratio between naïve
1397 and memory cells within the CD4^{+} CD127^{low}CD25^{hi} Treg gate at the three assessed timepoints (Day 0,
1398 Day 27 and Day 55). The connecting line represents the median naïve:memory ratio in the 13 participants
1399 selected for single-cell analysis at each time point. **c**, Variation (depicted as the % change from baseline
1400 pre-treatment levels) in the naïve:memory ratio within the CD4^{+} CD127^{low}CD25^{hi} Treg gate assessed by
1401 flow cytometry. Data shown depict the average (±SEM) variation at each visit for the 13 participants
1402 selected for single-cell analysis. **d**, Correlation between the naïve:memory ratio within CD4^{+}
1403 CD127^{low}CD25^{hi} T cells (left panel), or the corresponding ranks (right panel), obtained from FACS data
1404 (x axis) and that estimated from single-cell sequencing data (y axis). **e**, Correlation between the
1405 frequency of naïve (CD45RA^{+}; left panel) and memory (CD45RA^{-}; right panel) cells within
1406 CD127^{low}CD25^{hi} T cells obtained from FACS data (x axis) and that obtained from single-cell sequencing
1407 data (y axis). In **b**, **d** and **e**, each dot represents a sample, with colours and shapes representing
1408 participants and time points of origin, respectively. In **d-e**, linear regression lines are shown in black,
1409 and 95% confidence intervals of the regression estimate are shown in grey shades.

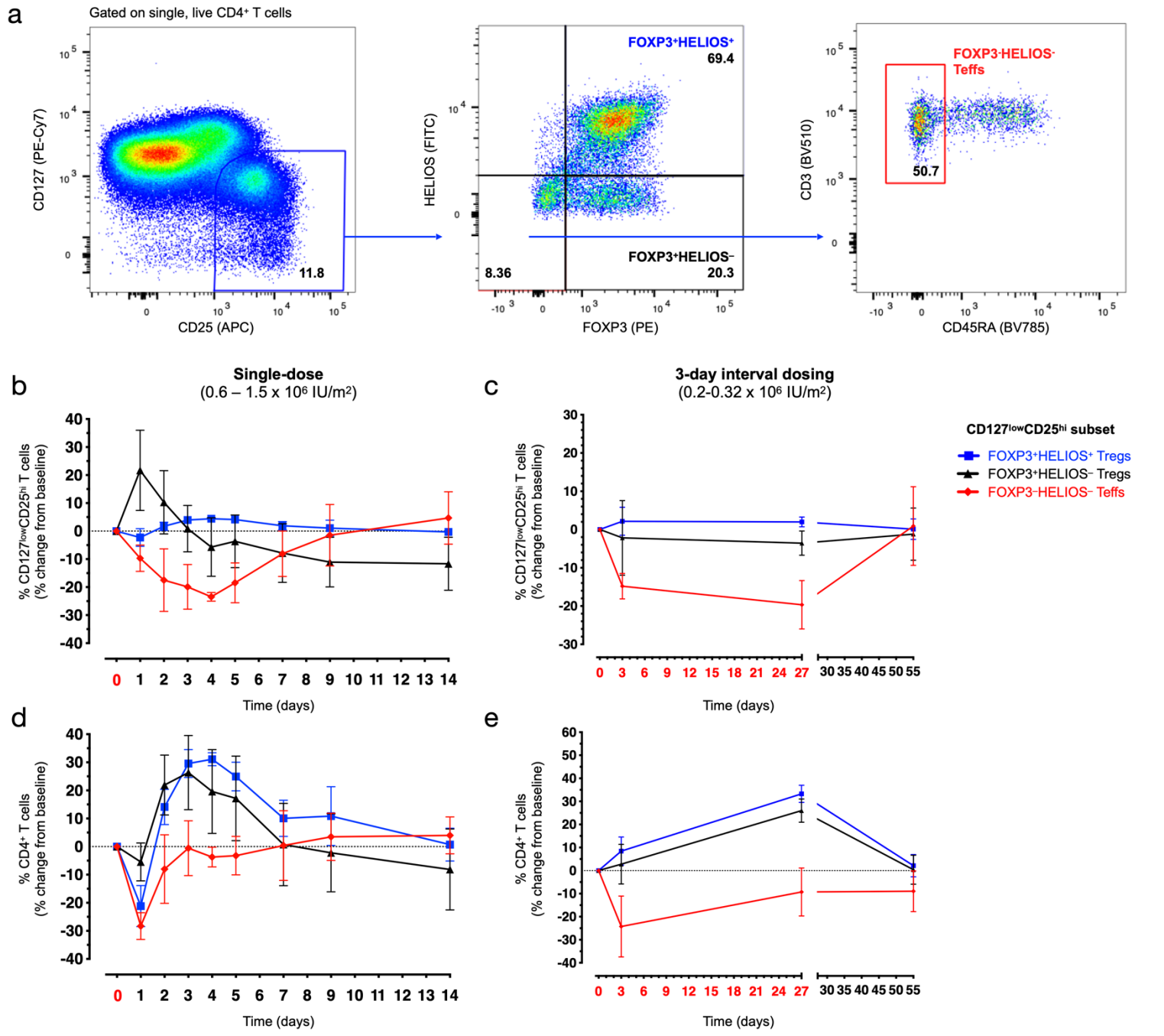

1411

1412 **Supplementary Figure 10. Delineation of Treg subsets by FACS**

1413 **a**, Gating strategy for the delineation of the FOXP3^{+}HELIOS^{+} Treg, FOXP3^{+}HELIOS^{-} Treg and
1414 CD45RA^{-} FOXP3^{-}HELIOS^{-} Teff subsets by flow cytometry. **b-c** Variation (depicted as the % change
1415 from baseline pre-treatment levels) in the frequency of FOXP3^{+}HELIOS^{+} (blue), FOXP3^{+}HELIOS^{-}
1416 (black) and CD45RA^{-} FOXP3^{-}HELIOS^{-} (red) cells within the CD127^{low}CD25^{hi} gate in patients treated

with a single dose (DILT1D; **b**) or with the 3-day interval dosing schedule (DILfrequency; **c**). Baseline levels (mean +/- SEM): (i) DILT1D: $FOXP3^{+}HELIOS^{+}$ = 71.5% +/- 1.47, $FOXP3^{+}HELIOS^{-}$ = 15.6% +/- 1.63 and $CD45RA^{-}$ $FOXP3^{-}HELIOS^{-}$ = 4.7% +/- 0.44; (ii) DILfrequency: $FOXP3^{+}HELIOS^{+}$ = 66.9% +/- 2.0, $FOXP3^{+}HELIOS^{-}$ = 19.8% +/- 1.60 and $CD45RA^{-}$ $FOXP3^{-}HELIOS^{-}$ = 8.0% +/- 1.02. **d-e**, Variation (depicted as the % change from baseline pre-treatment levels) in the frequency of the $FOXP3^{+}HELIOS^{+}$ Treg, $FOXP3^{+}HELIOS^{-}$ Treg and $CD45RA^{-}$ $FOXP3^{-}HELIOS^{-}$ Teff subsets in patients treated with a single dose (**d**) or with the 3-day interval dosing schedule. Baseline levels (mean +/- SEM): (i) DILT1D: $FOXP3^{+}HELIOS^{+}$ = 5.0% +/- 0.54, $FOXP3^{+}HELIOS^{-}$ = 1.2% +/- 0.24 and $CD45RA^{-}$ $FOXP3^{-}HELIOS^{-}$ = 0.34% +/- 0.06; (ii) DILfrequency: $FOXP3^{+}HELIOS^{+}$ = 4.2% +/- 0.44, $FOXP3^{+}HELIOS^{-}$ = 1.3% +/- 0.22 and $CD45RA^{-}$ $FOXP3^{-}HELIOS^{-}$ = 0.49% +/- 0.05. (**e**). Data were generated by intracellular flow cytometry in 6 patients from the DILT1D (treated with doses ranging from 0.6-1.5 x 10^{6} IU/m^{2}) and 5 patients from the DILfrequency (treated with interval doses ranging from 0.2-0.32 x 10^{6} IU/m^{2}). IL-2 dosing days are depicted in red in the x axis.

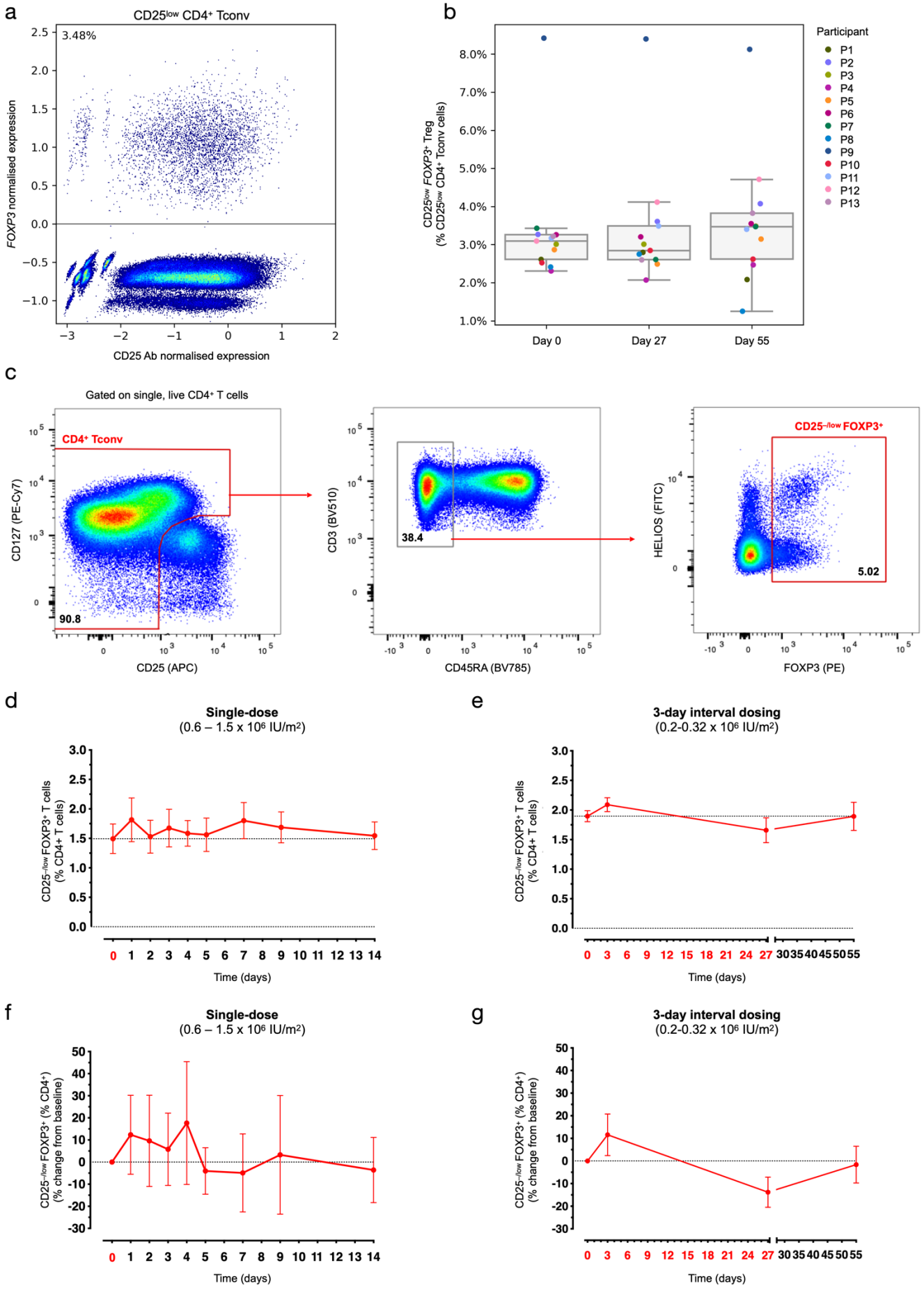

Supplementary Figure 11. Interval low-dose IL-2 treatment does not affect the frequency of CD25$^{-/low}$ FOXP3^{+} T cells

a, Identification of FOXP3^{+} within cells sorted from the CD25$^{-/low}$ Tconv gate. FOXP3^{+} cells were defined as cells with one or more counts of *FOXP3* RNA detected. Data was generated from the analysis of the 13 DILfrequency donors selected for the single-cell multiomics analysis. **b**, Box and whiskers plot depicts the frequency of FOXP3^{+} cells within the CD25$^{-/low}$ Tconv gate at Days 0, 27 and 55. Each dot represents a sample, with colours and shapes representing participants and time points of origin, respectively. **c**, Gating strategy for the delineation of CD25$^{-/low}$ FOXP3^{+} T cells by flow cytometry. **d-e** Frequency of CD25$^{-/low}$ FOXP3^{+} T cells in patients treated with a single dose (DILT1D; **d**) or with the 3-day interval dosing schedule (DILfrequency; **e**). **f-g**, Variation (depicted as the % change from baseline pre-treatment levels) in the frequency of the CD25$^{-/low}$ FOXP3^{+}T cells in patients treated with a single dose (**f**) or with the 3-day interval dosing schedule (**g**). Data were generated by intracellular flow cytometry in six patients from the DILT1D (treated with doses ranging from 0.6-1.5 x 10^6 IU/m^2) and patients from the DILfrequency (treated with interval doses ranging from 0.2-0.32 x 10^6 IU/m^2). IL-2 dosing days are depicted in red in the x axis.

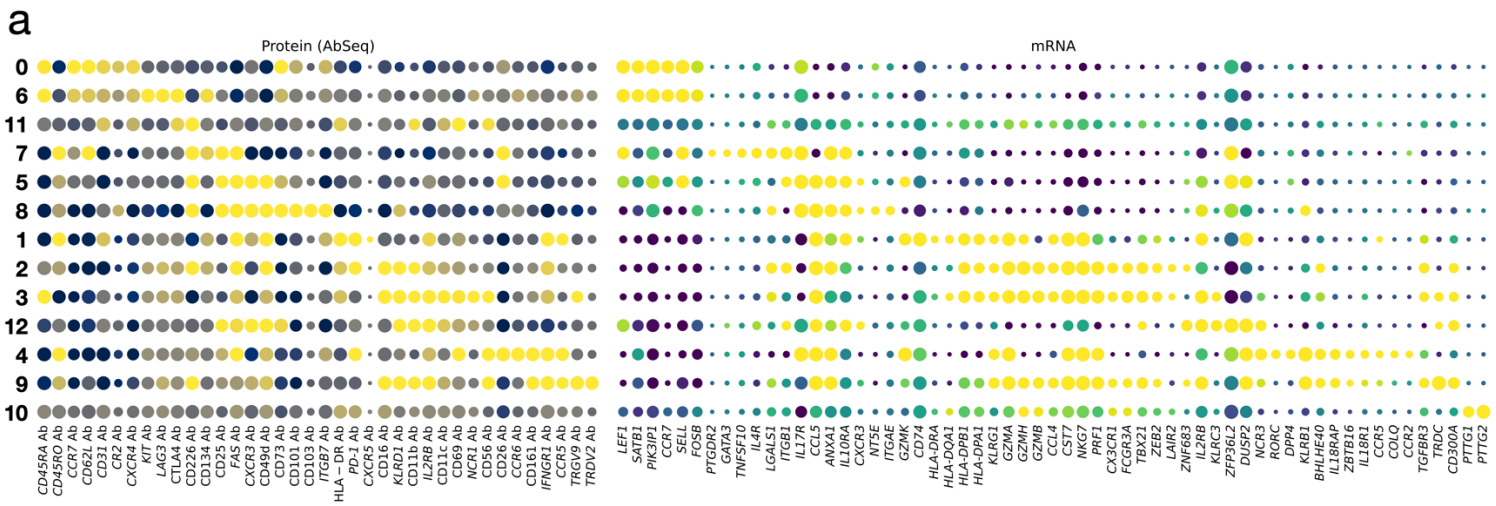

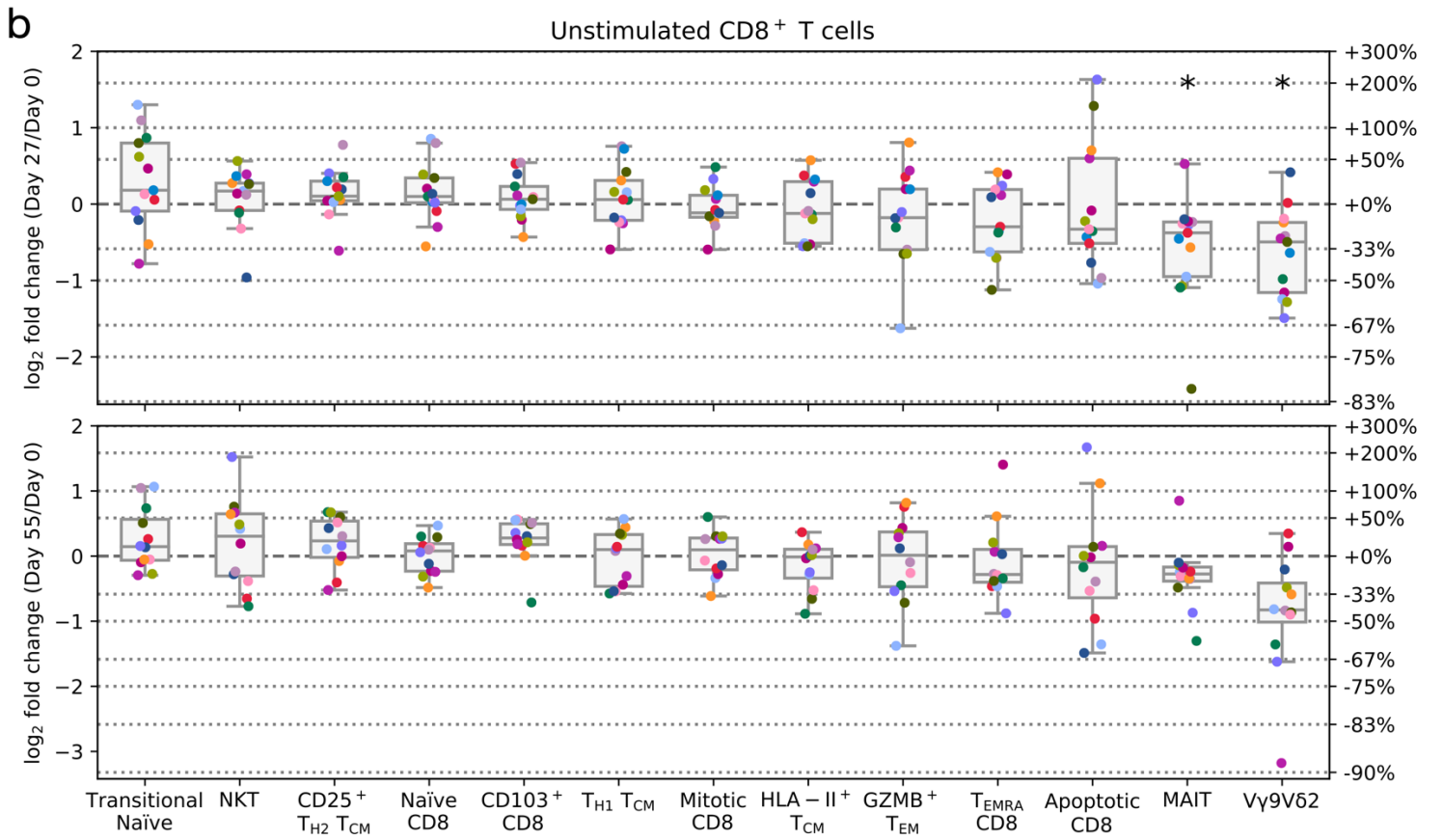

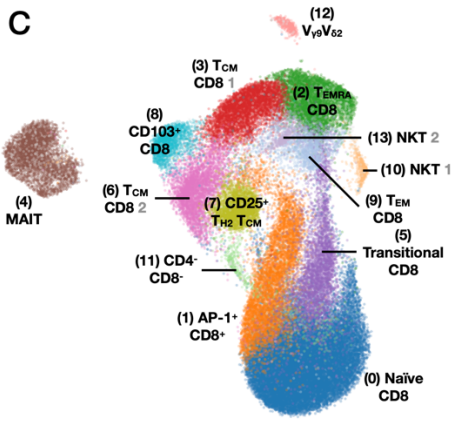

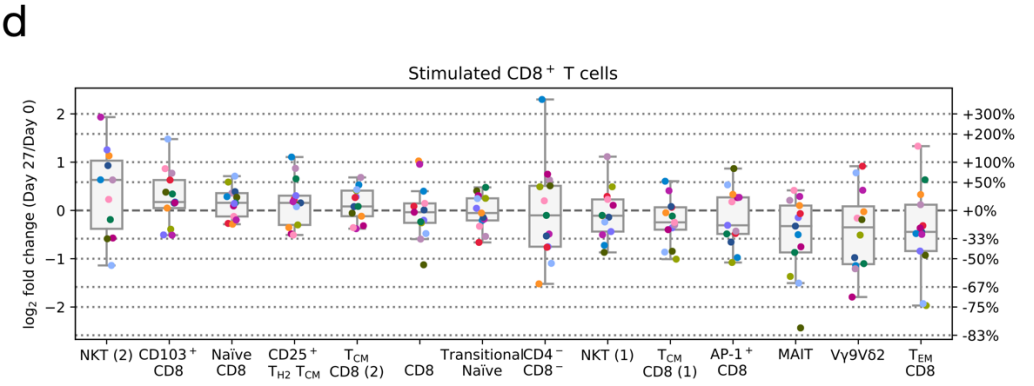

Supplementary Figure 12. Functional annotation of CD8$^+$ T cells.

a, Expression of selected differentially-expressed markers delineating the functional subsets identified from the 13 clustering of the 93,621 unstimulated CD8$^+$ T cells profiled in this study. The size of the dots represents the frequency of the marker in the respective cluster and the colour brightness represents the relative expression level. Protein markers (AbSeq) are shown on the left section of the plots and mRNA markers on the right section. **b,** Relative frequency changes of all identified CD8$^+$ T cell clusters on Day 27 (top panel) or Day 55 (bottom panel) compared to the baseline pre-treatment levels. **c**, UMAP plot depicting the clustering of *in vitro* stimulated CD8$^+$ T cells. Clusters were manually annotated based on the expression of key differentially expressed mRNA and protein markers. **d**, Relative frequency changes of the 14 identified stimulated CD8$^+$ T cell clusters at Day 27 compared to the baseline pre-treatment (Day 0) levels.

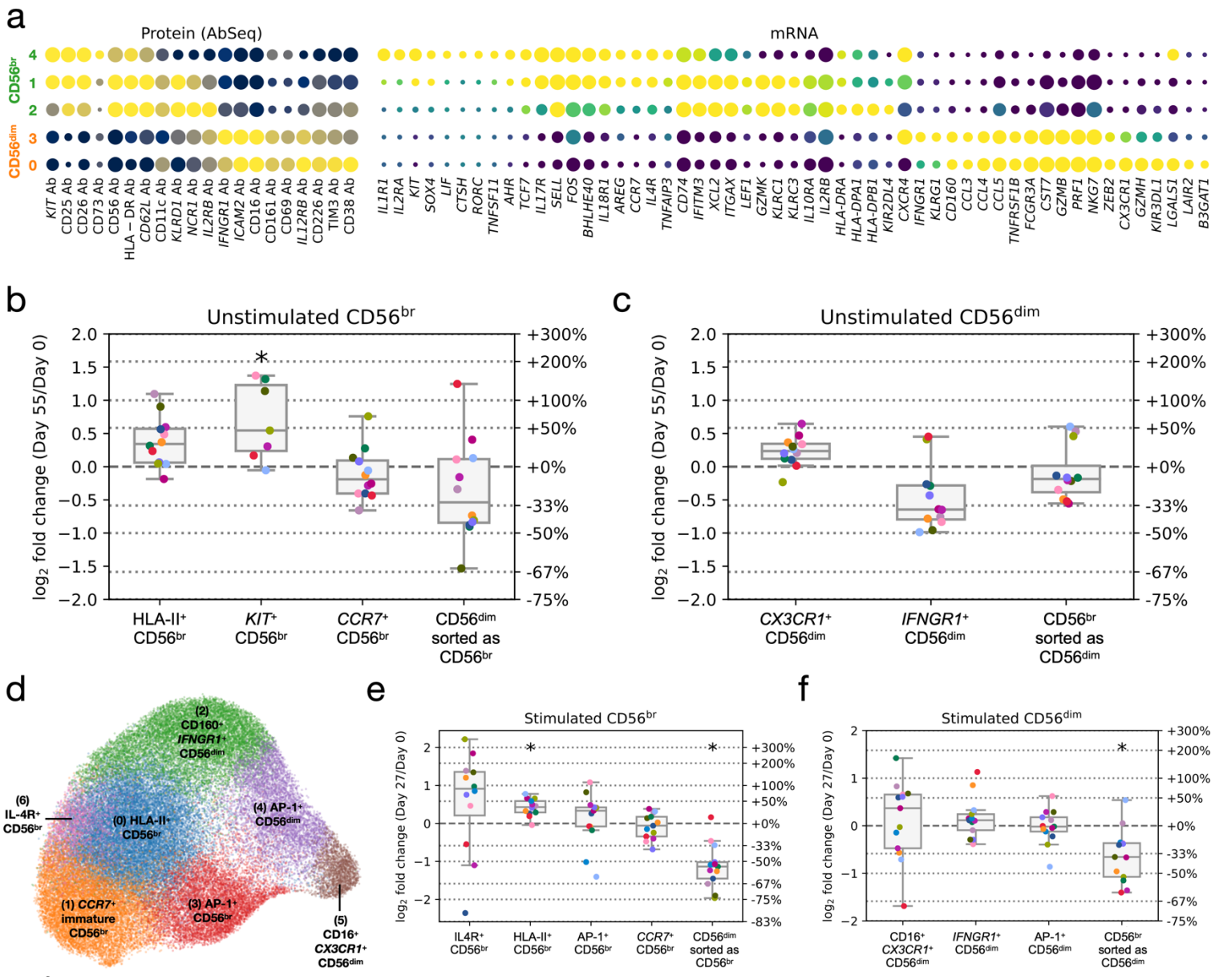

1463 **Supplementary Figure 13. Functional annotation of CD56$^+$ NK cells.**

1464 **a**, Expression of selected differentially-expressed markers delineating the five functional subsets
1465 identified from the clustering of the 99,169 unstimulated CD56$^+$ NK cells profiled in this study. The size
1466 of the dots represents the frequency of the marker in the respective cluster and the colour brightness
1467 represents the relative expression level. Protein markers (AbSeq) are shown on the left section of the
1468 plots and mRNA markers on the right section. The dotted red line separates the clusters corresponding
1469 to either CD56^{br} (top) and CD56^{dim} NK cells (bottom). **b-c**, Relative frequency changes of all identified
1470 unstimulated CD56^{br} (**b**) and CD56^{dim} (**c**) NK cell clusters on Day 55 compared to the baseline pre-
1471 treatment levels. **d**, UMAP plot depicts the clustering of *in vitro* stimulated CD56$^+$ NK cells. **e-f** Relative

1472 frequency changes of all identified clusters of cells sorted from either the $CD56^{br}$ (**e**) or $CD56^{dim}$ (**f**) NK
1473 cell gates following *in vitro* stimulation on Day 27 compared to the baseline pre-treatment (Day 0) levels.

1474

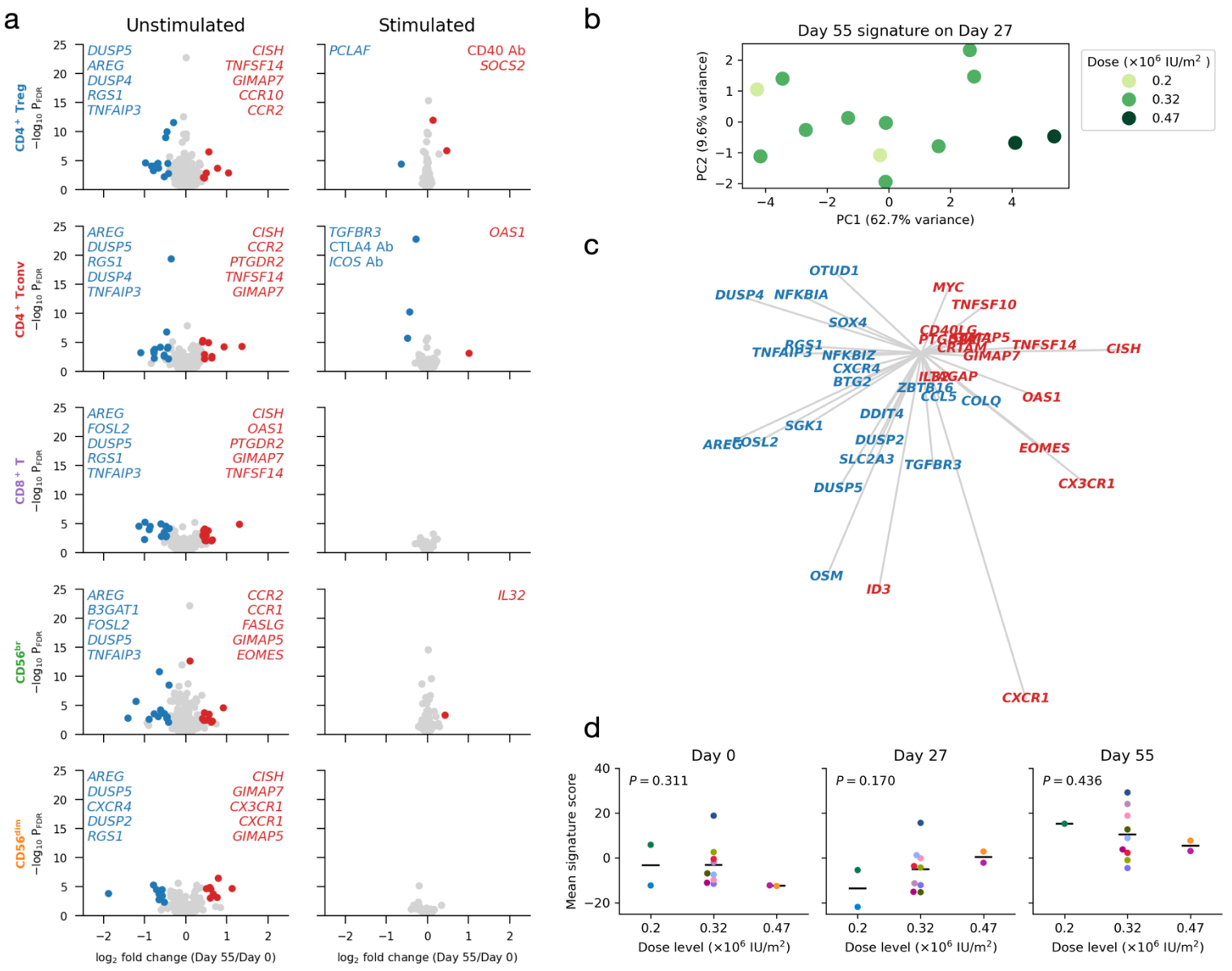

1476 **Supplementary Figure 14. Induction of the anti-inflammatory gene expression signature at Day**
1477 **55 is IL-2 dose-dependent and is detected in all T and NK cell populations**

1478 **a**, Volcano plots depicting gene expression changes between Day 0 and Day 55 for the five assessed
1479 immune populations, for unstimulated (left panels) and stimulated (right panels) cells. Significantly
1480 differentially expressed genes are coloured in red (upregulated genes) or blue (downregulated genes).
1481 The top five up- and downregulated genes (as defined by fold change) are labelled on each panel. **b**,
1482 Principal component analysis (PCA) correlating gene expression changes with dose levels. PCA was
1483 performed on $\log_2$ fold-change values of Day 55 signature genes on Day 27 in $CD8^+$ T cells. Each dot
1484 represents a participant, with colours indicating IL-2 dose levels. Vectors representing the gene loading

scores of PC1 and PC2 are shown on the right panel, with genes up- and downregulated on Day 55 shown in red and blue, respectively. **c**, Day 55 signature scores by participant for each time point. Each participant is represented by a different colour. **d**, Day 55 signature scores plotted against IL-2 dose. The average value of the Day 55 signature score in the five cell types is shown for each participant.

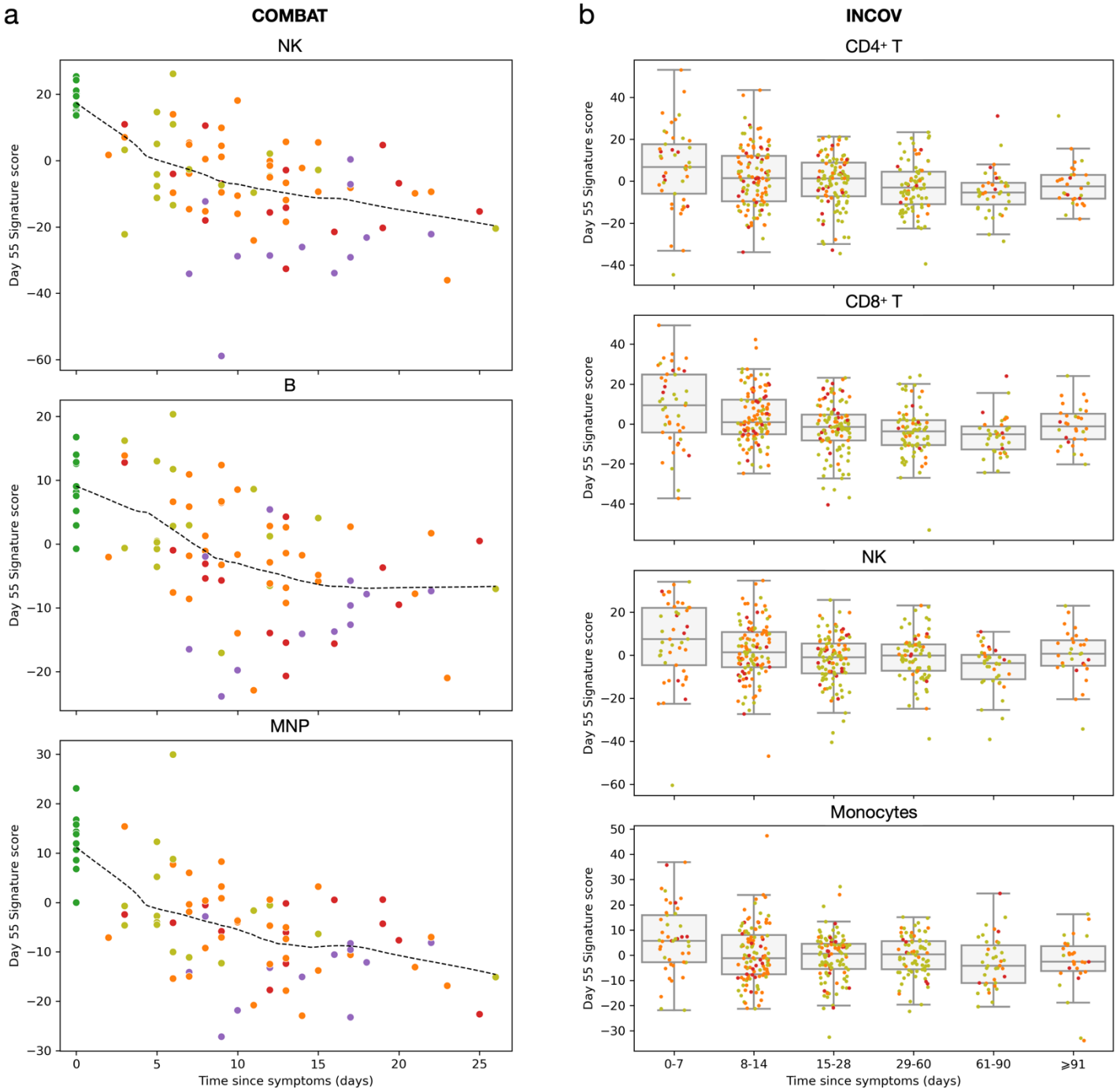

1491

1492 **Supplementary Figure 15. Expression of anti-inflammatory gene expression in COVID-19 patients**

1493 **a**, Day 55 signature scores plotted against the time since COVID-19 symptoms in the COMBAT cohort
1494 in NK cells, B cells and mononuclear phagocytes (MNP). **b**, Day 55 signature scores plotted against the
1495 time since COVID-19 symptoms in the INCOV cohort in $CD4^+$ T cells, $CD8^+$ T cells, NK cells and

monocytes. In **a** and **b**, each dot represents a pseudo-bulk sample from a certain participant and time point. Up to three longitudinal samples may originate from the same participant. COVID-19 patients were stratified according to their maximum disease severity. Dashed black lines represent smooth curves fitted by locally weighted scatterplot smoothing (LOWESS).

Supplementary Information

Supplementary Table 1. Baseline characteristics of study participants

Supplementary Table 2. Targeted mRNA, protein (AbSeq) and immunostaining panels used in this study

Supplementary Table 3. Characteristics of COMBAT study participants with single-cell data available

Supplementary Data 1. Summary of the cluster-specific RNA and AbSeq markers used for cell type annotation

Supplementary Data 2. Differential expression between Day 0 and Day 27 or Day 55 analysed using DESeq2